**Title**
Magnetic-Field-Guided Assembly of Anisotropic Nanostructures for Optical Applications

**Author**
Wang, Mingsheng

**Publication Date**
2016

UNIVERSITY OF CALIFORNIA
RIVERSIDE

# Magnetic-Field-Guided Assembly of Anisotropic Nanostructures for Optical Applications

A Dissertation submitted in partial satisfaction
of the requirements for the degree of

Doctor of Philosophy

in

Chemistry

by

Mingsheng Wang

March 2016

Dissertation Committee:
Dr. Yadong Yin, Chairperson
Dr. Ludwig Bartels
Dr. Jingsong Zhang

The Dissertation of Mingsheng Wang is approved:

Committee Chairperson

University of California, Riverside

# Acknowledgement

Pursuing a Ph.D. is never an easy decision. When I came to the United States six years ago, I could never imagine how this decision was going to change my life. This change is, however, not bad. When I retrospect, I can clearly remeber every piece of anxiety, frustration and happiness. I am proud of all the achievements I made during my Ph.D. study, not only a couple of papers published in pretigious research journals, but also the right way of criticial thinking and of doing scientific research, which will benefit me a lot in my future career.

First, I would like to express my deepest gratitide to my Ph.D. advisor, Dr. Yadong Yin for his guidance, encouragement and support. Yadong has dedicated a high amount of time and efforts to me since I ever started my first project. His punctiliousness and enthusiasm towards scientific research set an excellent role model for all people who are willing to do this in the future. His role is far beyond lenders of intellectual loans to me. The most important thing I have learned from him is the positive attitude in dealing with any problems in life, which helped me overcome many obstables in my life.

I am also very thankful to my other committee members Prof. Bartels and Prof. Zhang for their valuable help and comments on my dissertation. Without the contribution from the committee, this dissertation can be little more than a set of technical exercises. I have received valuable help in both academic research and daily life from Dr. Chuanbo Gao, Dr. Le He, Wenjing Xu. I would acknowledge the substantial influence on this dissertation by many past and current members in Yin group: Dr. Yu Lu, Dr. Yongxing

Hu, Dr. Qiao Zhang, Dr. Zhenda Lu, Lishun Fu, Xin Wang, Yaocai Bai, Xiaojing Wang, Ji Feng, Zhiwei Li; and Chi Tang from department of physics & astronomy, and Prof. Zorba from Whittier College for their great help in the collaboration of my projects. I would also like to take this opportunity to thank U.S. Army Research Laboratory and U.S. National Science Foundation for their financial support on my research projects.

I would like to thank my parents Kexin Wang and Yueying Zhou for their understanding and unconditional support throughout everything; and most of all, my spouse, Jie Sheng for always encouraging me, standing with me, and being the one on my back.

# ABSTRACT OF THE DISSERTATION

## Magnetic-Field-Guided Assembly of Anisotropic Nanostructures for Optical Applications

by

Mingsheng Wang

Doctor of Philosophy, Graduate Program in Chemistry
University of California, Riverside, March 2016
Dr. Yadong Yin, Chairperson

Magnetic-field-guided assembly of colloidal matter has long been regarded as one of the most unique methods for bottom-up fabrication of functional materials, owing to the instantaneous and anisotropic nature of magnetic interactions. The magnetic assembly process is driven by magnetic dipole–dipole interactions which magnitude and direction can be conveniently controlled by the field strength and direction. The collective property of the resultant superstructures can often response to the external magnetic stimuli, allowing the facile design of smart and responsive devices. Tremendous efforts have been made in the development of magnetic-field-guided assembly strategies; however, current magnetic assembly processes were limited to spherical, isotropic building block; while little progress has been achieved to the assembly of anisotropic building blocks, which, however, hold great promise as they often possess shape-dependent physical and chemical properties and add more degrees of freedom to the materials design.

In this dissertation, I summarized my explorations on magnetic anisotropic nanostructures, from their controlled synthesis, guided assembly, to the tuning of the resultant superstructures, with a special emphasis on the tuning of their collective optical. To start with, I developed a sophisticated method for the controlled synthesis of one-dimensional magnetic nanostructures, with tunable size, shape, aspect ratio and magnetic property. These magnetic nanostructures have great uniformity and serve as excellent building blocks for magnetic assembly. I studied the assembly behavior of these building blocks, investigated the effects of their morphology, volumetric fraction, and the direction and strength of external magnetic fields, and optimized the assembly process with respect to these factors.

After successfully assembling the anisotropic magnetic building blocks into organized structures with positional periodicities and/or orientational orders, I investigated the optical tuning of the resultant superstructures. Owing to the anisotropy of building blocks, these superstructures exhibit unique angular-dependent optical property, which can be controlled by changing the direction of external magnetic fields, as anisotropic magnetic particles spontaneously align themselves parallel to the field direction. I demonstrated this concept by using the magnetic field direction to tune the photonic property, polarity and plasmonic property of as-assembled superstructures. Such method is instant, reversible, contact-less, and only requires a weak magnetic field. It is expected to provide a general and very effective mean to assemble a wide range of nanoscale objects, and paves the way towards fabrication of novel superstructures and design of function devices in many fields.

# Table of Contents

## List of Figures

# Chapter 1

# Introduction

## 1.1 Introduction to Colloidal Assembly

The self-assembly of colloidal particles represents for an ideal model system in condensed matter physics, which allows exploration of the phase complexity in a single sample as the inter-particle interactions can be conveniently tuned.[1-6] Compared with other atomic systems, it is more convenient to conduct the study of colloidal particles in more experimentally accessible length and time scales. During the last several decades, progress in the fundamental study of colloidal assembly has enabled deep understanding of atomic world. For example, the study of colloidal assembly in aqueous dispersion helped to clarify the early stage of crystallization in dilute solutions; and the assembly of binary nanoparticles provided valuable insight for the construction of ionic crystals.

On the other hand, self-assembly of colloidal particles is also of practical interest as it is a powerful bottom-up method for the fabrication of functional nanostructured materials, which include but not limit to nanoscale electronic, magnetic, optical, catalytic, and many energy-related devices.[7-14] More importantly, by designing and modifying the physical and/or chemical property of colloidal building blocks and/or their surroundings, the self-assembly process can often be triggered and controlled by certain physical stimuli (temperature,[15, 16] light,[17, 18] humidity,[19, 20] mechanical stress,[21] electric and magnetic fields[22-27]) or chemical stimuli (chemical interactions,[28, 29] ionic strength and environmental pH[30-34]), resulting in an acceleration and improved precision of the whole process.

Among variety of strategies for the guided assembly of colloidal matter, magnetic-field-guided routes have been regarded as the most unique due to the instantaneous and anisotropic nature of magnetic interactions, and have been widely introduced to the materials fabrication and design of function devices in many fields, such as photonics[35-39], drug delivery[40, 41], object patterning[42-46], magnetic levitation[47-50] and so on. Magnetic-field-guided colloidal assembly routes have several common characteristics. First, the assembly process is driven by magnetic dipole–dipole interactions which are directional in nature, and can be either attractive or repulsive, depending on the angle between the magnetic field and the line connecting the dipoles, thus permitting significant experimental design freedom.[51] Second, strong magnetic interactions can be effectively and reversibly initiated by the application of an external magnetic field, providing enough driving force for the rapid assembly of colloidal matter even within one second.[52, 53] Third, magnetic interactions act at a distance, enabling contactless manipulation of objects, and are independent of changes in experimental conditions, including temperature, pH and solvent composition.[54] Fourth, magnetic fields can easily be created, either by permanent magnets or electromagnets. More importantly, their strengths and spatial distributions can be programmed macroscopically and microscopically, allowing the realization of fine control over the assembly of colloidal matter, from the movement of one single object in a locally magnetized area to the globally synchronized motion of large numbers of objects.[55]

## 1.2 General Principle of Magnetic Interactions

Generally, colloidal magnetic particles experience various type of magnetic interactions in external magnetic fields.[27, 56] Upon the application of external magnetic fields, they are magnetized with an induced magnetic dipole moment $m = \chi HV$, where $\chi$ is the volume susceptibility of the particle, $H$ is the local magnetic field, and $V$ is the volume of the particle. For a particle with a magnetic moment of $m$, its induced magnetic field $H_1$ felt by another particle can be described as:

$$H_1 = [3(m \cdot r)r - m]/d^3$$

where $r$ is the unit vector parallel to the line pointed from the center of the first particle to that of the second particle, and $d$ is the center-center distance. The dipole-dipole interaction energy of second particle with the same magnetic moment $m$ can be thus written as:

$$U_2 = m \cdot H_1 = (3\cos^2\theta - 1)m^2/d^3$$

where $\theta$ ranging from 0° to 90°, is the angle between the direction of external magnetic field and the line connecting the center of the two particles. The dipole force exerted on the second particle induced by the first particle can be expressed as:

$$F_{21} = \nabla(m \cdot H_1) = 3r(1 - 3\cos^2\theta)m^2/d^4$$

which clearly shows the dependence of the dipole-dipole force on the configuration of the two dipoles. At the critical angle of 54.09°, the interaction approaches zero. The dipole-dipole interaction is attractive when $0° \leq \alpha < 54.09°$ and repulsive in cases where $54.09° < \alpha \leq 90°$. When the interaction energy is large enough to overcome thermal fluctuations, the magnetic dipole-dipole force drives the self-assembly of particles into one-dimensional (1D) chain-like structures along the dipole moment.

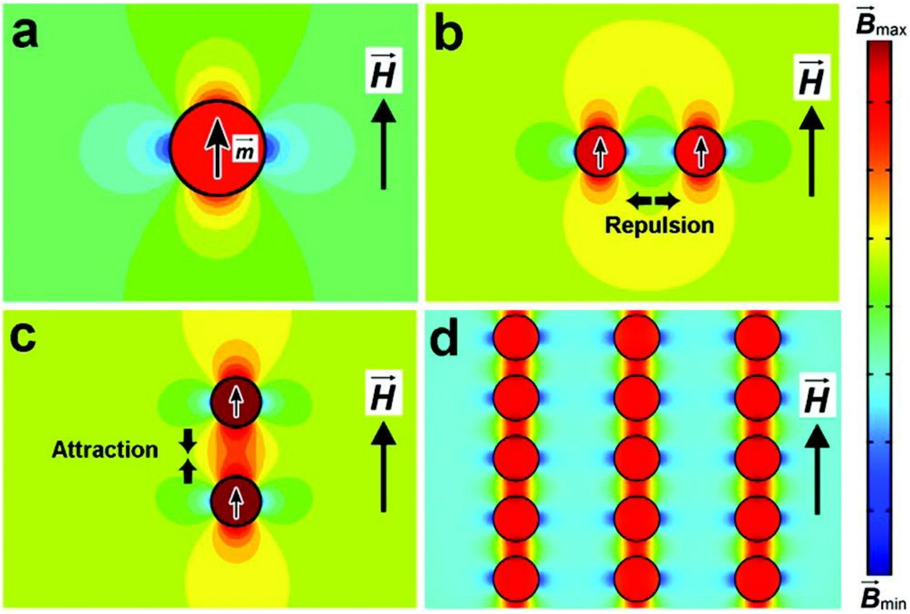

**Figure 1.1** (a) Magnetic field distribution around a superparamagnetic particle with a dipole moment in the same direction as the external magnetic field. The repulsive (b) and attractive (c) dipole–dipole forces in different particle configurations drive the formation of particle chains along the magnetic field (d). The color bar on the right shows the relative strength of the local magnetic field.

Practically, the magnetic fields for experimental use are generated by a permanent magnet or an electromagnet, and are therefore not always homogeneous. Magnetic particles in a non-homogeneous magnetic field will experience a force along the direction of increasing field strength. The magnitude of this magnetophoretic force is monotonically related to the difference between the magnetic susceptibility of the particles and the magnetic susceptibility of their surroundings. If the difference is larger enough, the magnetophoretic force can be approximated as:

$$F_{phr} = \nabla B^2 \cdot V\chi / 2\mu_0$$

It drives the movement of particles towards regions with the maximum magnetic field strength and subsequently induces a particle concentration gradient or crystallization.

Magnetic shape anisotropy can also play a very important role in the magnetization of particles of anisotropic shapes.[57-59] A magnetized particle will have induced magnetic poles at its surface, which will produce a demagnetizing field in the opposing direction to the magnetization, $B_{demag} = -\mu_0 N \cdot m$, where $N$ is the demagnetizing tensor, and $m$ is the induced magnetic moments. Then the energy of the particle in its own demagnetizing field is given by the integral:

$$E_{demag} = -\frac{1}{2}\int B_{demag} \cdot mdV = \frac{1}{2}\int \mu_0 (N \cdot m) \cdot mdV$$

For an infinitely long cylinder, the expression can be simplified as:

$$E_{demag} = \frac{1}{4}\mu_0 m^2 \sin^2 \theta$$

where $\theta$ is the angle between the major axis of the cylinder and the field direction. As a result, anisotropic particles spontaneously align their major axis parallel to the direction of external magnetic fields, in order to reduce the demagnetizing field as well as the energy associated with it.[60, 61] For an infinitely expanded and/or very thin ellipsoid, the expression can be simplified as:

$$E_{demag} = \frac{1}{2}\mu_0 m^2 \cos^2 \theta$$

where $\theta$ is the angle between the major axis of the thin ellipsoid and the field direction. As a result, an in-plane orientation of magnetic moment of thin ellipsoid is energetically favorable, and it spontaneously align their plane parallel to the direction of external magnetic fields, in order to reduce the demagnetizing field as well as the energy associated with it.[62-64]

## 1.3 Magnetic Assembly of Spherical Nanoparticles

Magnetic nanoparticles assemble into various kinds of structures under external magnetic fields, with key factors which determine the final equilibrium state of the assembly process being the magnitude of magnetic interactions between particles as well as the local concentrations of particles. The strength of external magnetic fields directly determine both factors, which enable people to fully control the assembly process of nanoparticles into desired structures. On one hand, it determines the magnitude of induced dipole moments in particles and therefore controls the magnitude of dipole-dipole interactions between particles; on the other hand, magnetophoretic forces induced by the inhomogeneity of magnetic fields drive the movements of particles towards increasing magnetic field strength and therefore creates differences in the local concentrations of particles.

### 1.3.1 1D Assembly of Spherical Nanoparticles

One of the most remarkable features of the assembly of magnetic nanoparticles is the formation of ordered structures. The transition from randomly distributed nanoparticles to 1D particle chains may represent the simplest switch between random and ordered states.[53, 65, 66] As a direct result of the directional magnetic dipole-dipole force, the chaining of nanoparticles happens when the force is strong enough to overcome the thermal fluctuations. Structures of 1D particle chains formed by nanoparticles with various kinds of sizes and chemical compositions have been intensively investigated, with spherical superparamagnetic magnetite nanoclusters chosen here as a model system.[67]

These superparamagnetic nanoclusters are composed of tiny (~ 10 nm) magnetite crystals. They show acute magnetic response and can be easily manipulated by external magnetic fields. Their zero net magnetic moments prevent them from permanent magnetically induced aggregation, and make the assembly process reversible. In the meanwhile, their highly charged surfaces provide a sufficient long-range inter-particle electrostatic repulsive forces, which balance with the magnetic dipole-dipole attractive forces and aid in an establishment of force equilibrium with in the chain-like structures. This equilibrium, however, is dynamic and sensitive. Slight changes in the field strengths can lead to destruction of the original equilibrium and reconstruction of a new equilibrium, and the inter-particle separations as well as the periodicities of chain-like structures change as a result.

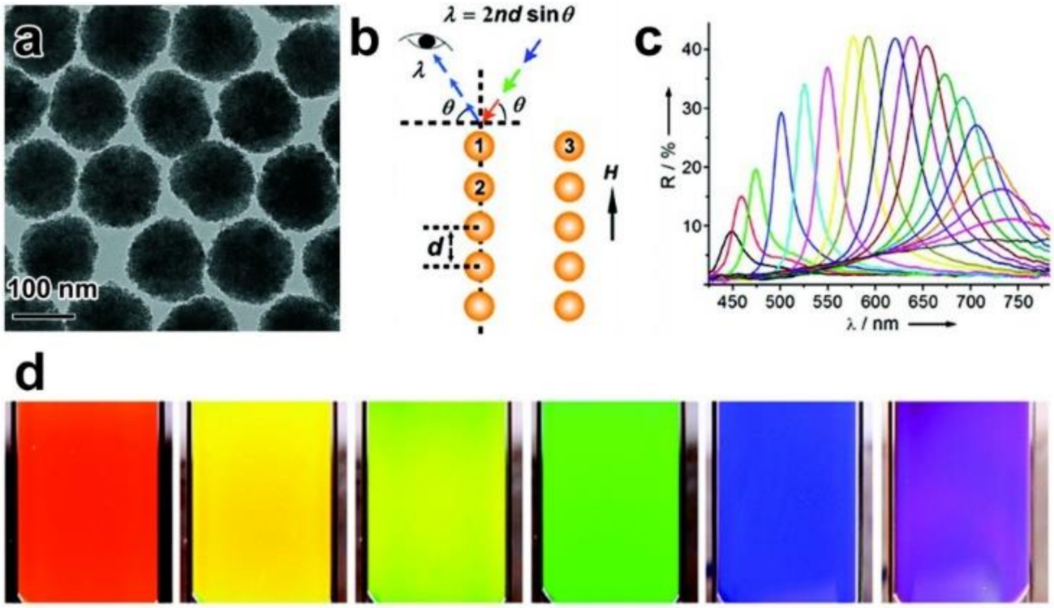

**Figure 1.2** (a) A representative TEM image of the superparamagnetic nanoclusters building blocks; (b) Scheme of Bragg diffraction from the 1D chain-like structures assembled from the building blocks; (c) Reflectance spectra of an aqueous dispersion of chain-like structures under magnetic fields with different strengths; (d) Digital photos showing the diffraction color change in a typical sample encapsulated in a capillary tube with a width of 1 cm in response to a magnetic field with increasing strengths from left to right.

These chain-like structures with ordered arrangements of nanoclusters serve as one of the smallest photonic structures, with their diffraction wavelengths determined by Bragg's law, $m\lambda = 2nd\sin\theta$, where $n$ and $d$ are their effective refractive index and periodicity, $m$ is the diffraction order, and $\theta$ is the glancing angle of the incident light.[36, 37] In response to the change of the external field strength, the periodicities of the chain-like structures alter. Their diffraction wavelengths are therefore responsive to external magnetic fields. After carefully designing the sizes of nanoclusters, their photonic colors can be effectively tuned within the visible light spectrum, from blue to red. The color change happens instantly upon the change in field strength.

In 1D chain-like structures, the magnetic dipole-dipole attractive forces are perfectly balanced by the electrostatic repulsive forces between particles. The inter-chain forces, mainly magnetic dipole-dipole repulsive forces, separate the chain away from each other. However, chain-like structures are not the end of the self-assembly phases of spherical nanoclusters. When stronger magnetic fields were applied, the magnetophoretic force induced the movement of particles towards higher gradient areas. In addition, the inter-particle dipole-dipole interactions became stronger. 1D chain-like structures become less thermodynamically favorable under this condition. As a result, they further coalesce through a side-by-side assembly manner into zigzag multiple chains, 2D planar structures, or even 3D structures.

### 1.3.2 2D Assembly of Spherical Nanoparticles

The presence of 2D planar structures have been proposed and indirectly observed by a number of theoretical and experimental works, although a solid evidence for the existence of 2D planar structures has yet been achieved until a recent study.[68] By taking advantage of a sol-gel process, the dynamic 2D structures formed by the magnetite nanoclusters can be in-situ stabilized for further characterization. It is clearly revealed by the characterization results that these 2D structures were evolved from the side-by-side coalescence of 1D chain-like structures. They have well-defined sheet-like morphology, with lengths and widths over 20 μm, and an average thickness of less than 200 nm, which is equivalent to the diameter of a single magnetite nanocluster and is two orders of magnitude smaller.

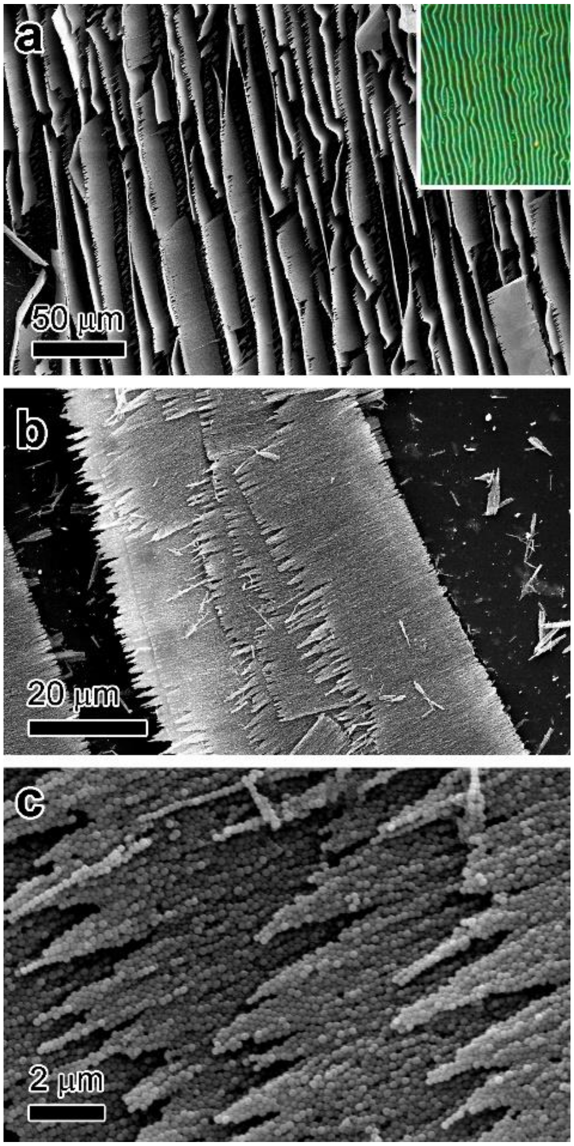

**Figure 1.3** (a-c) SEM images of 2D planar structures formed by the nanoclusters from different angles and under different magnifications. Inset: A digital image of 2D planar structures taken under an optical microscope in dark mode clearly reveal their green structural color.

### 1.3.3 3D Assembly of Spherical Nanoparticles

Further increasing the local particle concentrations and the field strength resulted in the formation of highly crystalline 3D structures. Small-angle X-ray scattering technique (SAXS) was used to investigate the 3D assembly process of magnetite nanoclusters.[69] In the absence of magnetic fields, the nanoclusters suspension exhibited three major diffraction rings with q ratios of $\sqrt{8}$: $\sqrt{24}$: $\sqrt{32}$, which corresponded to (220), (422) and (440) planes respectively and indicated the nanoclusters formed a polycrystalline fcc structure. The change in the structures was negligible when a 100 G magnetic field was applied; however, a reorganization of polycrystalline structure into well-oriented single-crystalline-like structure was found when the field strength further increased to 900 G, as evidenced by the evolution of diffraction patterns from rings to three sets of six diffraction spots. These diffraction spots have q ratios of $\sqrt{3}$: $\sqrt{4}$: $\sqrt{7}$, which corresponds to (110), (200) and (210) planes and suggests that magnetite nanoclusters formed a single-crystalline hexagonal-packed structures. The diffraction spots in the scattering pattern got further separated at a higher magnetic field strength of 1600 G, indicating the formation of the structure with improved crystallinity. The diffraction wavelengths of 3D photonic structures also changed during this process, with a blue shift from ~ 620 nm to ~ 500 nm.

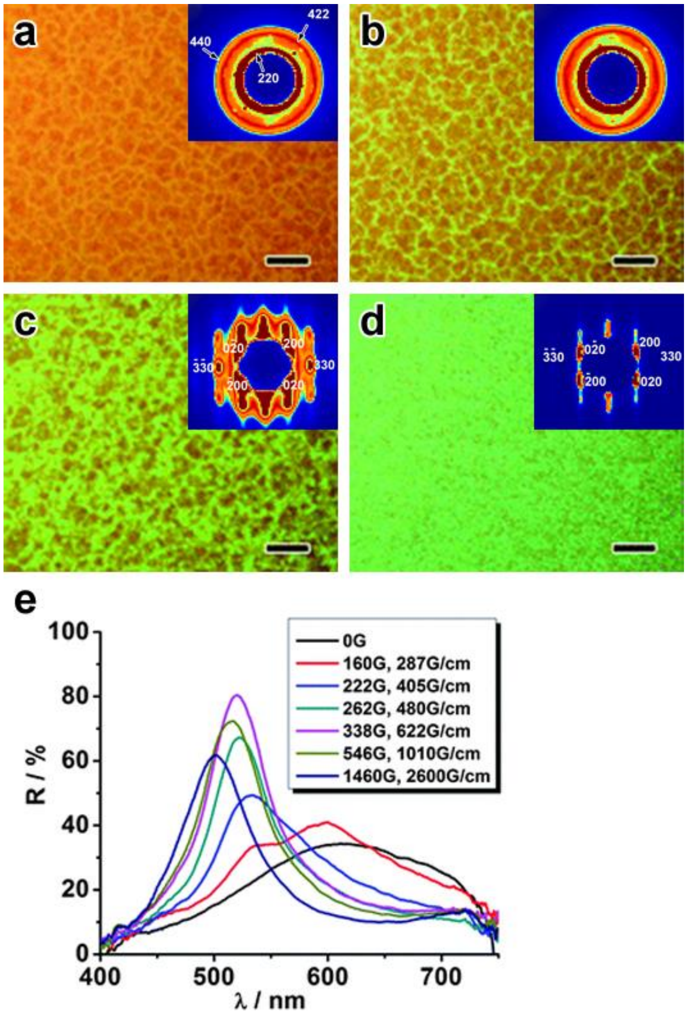

**Figure 1.4** (a-d) Digital images of highly crystalline 3D structures of nanoclusters taken under an optical microscope in dark mode. Inset: The corresponding SAXS pattern of 3D structures. Scale bar: 20 μm; (e) Reflectance spectra of 3D structures under magnetic fields with different strengths.

### 1.4 Magnetic Assembly of Anisotropic Particles

Living systems, for example, Morpho butterfly, peacock and Chrysochroa fulgidissima, often utilize ordered assemblies of anisotropic motifs such as plates and rods to produce their striking color effects.[70, 71] Compared with spherical building blocks, a unique feature of the anisotropic building blocks is that the collective property of their assemblies often show strong angular dependence. In addition to the positional order that is usually considered for describing assemblies from spherical building blocks, one should take orientational order into account when anisotropic building blocks are assembled. Lots of efforts have been made to organizing anisotropic colloidal particles such as polystyrene and ZnS,[72-78] albeit the assembly methods are conventional and time-consuming, and the resulting structures do not exhibit unique collective property than those from spherical particles.

The key to the exploration in the assembly of anisotropic building blocks is the effective tuning in their orientations, in which magnetic assembly strategy has unique advantages. Owing to their anisotropic morphology, the orientation of anisotropic magnetic particles can be easily controlled by external magnetic fields. Upon the application of magnetic fields, they instantly rotate and align their long axis parallel to the field direction to minimize their magnetostatic energy, making them ideal building blocks for constructing ordered structures with novel collective property.

### 1.4.1 Anisotropic Structures for Light Scattering Modulation

Anisotropic magnetic nanostructures suspended in a carrier fluid have been intensively studied for their potential use in light transmission modulation.[79-81] The common idea in these applications is to use external stimulus, such as a magnetic field, to coax and assemble magnetic nanostructures into ordered or aligned systems in a reversible way, which results in the change of their scattering cross section. A simple demonstration for this idea is the use of $Fe_3O_4/SiO_2/TiO_2$ peapod-like nanostructures for magnetically controlled light intensity modulation and chopping.[82, 83] In a typical light modulation experiment, an aqueous solution containing the peapod-like nanostructures is placed in a cylindrical glass cell. The glass cell is positioned inside a solenoid which is driven by an audio amplifier which in turn is driven by a function generator. Alternating linearly polarized magnetic fields of a few mT magnitude were facilely obtained at the center of the solenoid with tunable frequency capability. A constant intensity polarized laser beam is directed at the sample, goes through the sample, and is then detected by a photodetector which in turn is monitored by an oscilloscope. A typical result of the optical intensity modulation under an alternating magnetic field with a strength of 4.5 mT and a frequency of 905 Hz is shown in Figure 1. The top signal drives the solenoid magnetic field, while the bottom signal is what is observed at a photodetector due to the modulated light. The light intensity modulation is achieved by a change of the scattering cross sections of the peapod-like nanostructures, due to their alignments with the alternating magnetic field, as schematized in Figure 1d. For a full period of the periodic signal driving the magnetic field, the peapod-like nanostructures align themselves twice, once for the +B direction and the other for the −B direction, allowing maximum light passage each time. As a result, the laser beam comes out of the sample with its intensity modulated at twice the frequency of the driving magnetic field signal. The high fidelity in the waveform of the modulated signal and the constant-phase relation between the driving signal and the modulated signal benefit from the small inertia of the particles. It is worth noting that the modulation frequency is comparable with the frequency of commercial mechanical spoked-wheel-based optical choppers. Since no mechanical moving parts are involved, this magnetically controlled light intensity modulation system may find applications in optical circuits with advantages including high reliability, long lifetime, and great flexibility and convenience for a high degree of device integration.

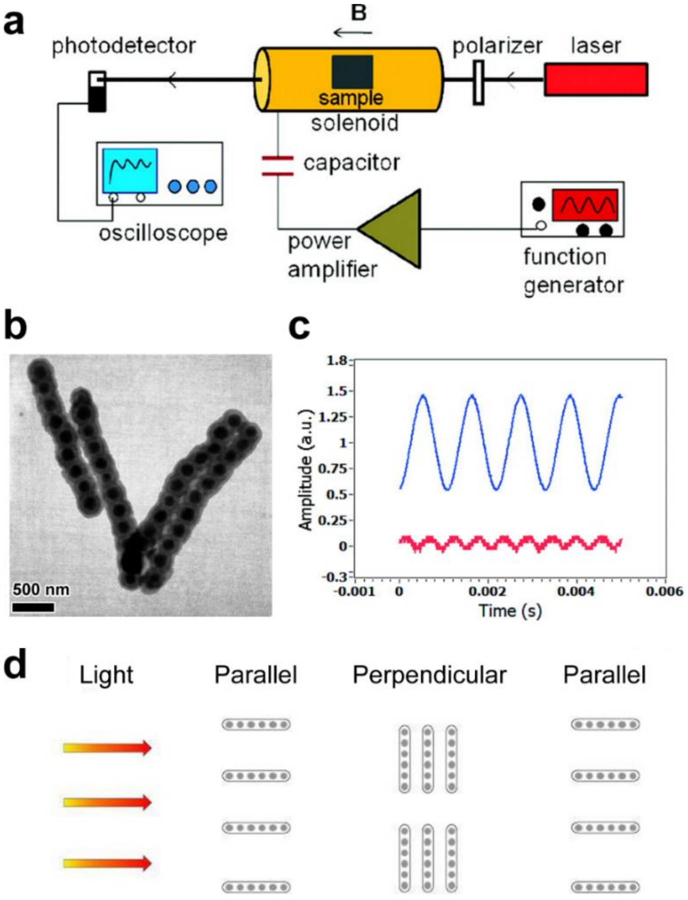

**Figure 1.5** (a) Schematic diagram of the experimental setup used for modulation of laser intensity; (b) TEM image of $Fe_3O_4/SiO_2/TiO_2$ peapod-like superstructure; (c) Oscilloscope screenshot of light modulation with peapod superstructures with lengths of 1 ~ 3 µm at 905 Hz; (d) Depiction of how light modulation is caused during a full cycle of the magnetic field oscillation.

### 1.4.2 Anisotropic Structures for Light Reflection Modulation

The similar concept was also extended to materials with planar morphology. When light encounters a metallic surface, the penetrating light causes the cloud of negative charge – consisting of weakly bound electrons of the metal atoms – to vibrate in phase with the light frequency, and this vibrating and charged cloud produces light of the same frequency, specifically reflected light. Therefore, the use of planar metallic materials as scatters not only enables the light transmission modulation, but also bring the opportunities for effectively modulating the intensity of reflected light and thus benefits the development of reflective displays.[84-86]

Gold microplates were chosen as an example for the demonstration of this idea.[87] After being synthesized, they were rendered magnetically functional via conjugation to amine terminated superparamagnetic $\gamma$-$Fe_2O_3$@$SiO_2$ nanoparticles. Since only a thin layer of magnetic material is necessary to render the plates magnetic, they retain their high reflectivity and their surrounding solution remains transparent, while their orientation can be readily, rapidly and reversibly tuned by applying a magnetic field oriented in varying directions. If the direction of incident light is fixed, the reorientation of microplates with external magnetic fields will results in the changes of its projected area as well as its scattering cross section, and thus the changes in the light transmittance and reflectance.

The reflectance of a dispersion of gold microplates can be conveniently modulated by external magnetic fields. As shown in Figure 2c, the reflectance was strongly dependent on the angle of the applied magnetic field. Almost no change in reflectance occurred when $\theta$ was increased from 0° ~ 60°, while a dramatic increase from 1% to 6% was observed as

$\theta$ was increased from 60° to 90°, suggesting a six fold difference between the maximum and minimum reflectance states. The transmittance changes of gold microplates dispersion exposed to a direction-varying magnetic field was also monitored by the transmittance spectra. As shown in Figure 2d, it could be varied from 42 % to 72 % as $\theta$ was decreased from 90° to 0°. This observed increase was largely due to a gradual change in the projected cross section of the plates, which was minimized when the major axis was aligned with the beam path and maximized when the plates were oriented perpendicular to the beam path.

In the absence of a magnetic stimulus, the gold plates dispersion exhibited a shiny, golden color reminiscent of bulk gold. Upon the application of a magnetic field oriented parallel to the viewing direction, the plates rapidly aligned with the applied field and the solution became transparent due to the minimized cross section of the microplates. As the applied magnetic field was rotated such that the angle between the magnetic field and the viewing direction ($\theta$) increased, the plate solution transitioned from being clear and transparent to opaque and reflective. This optical change was due to the plates in the solution becoming aligned perpendicular to the viewing angle ($\theta$ = 90°), which maximized the projected cross section of the plates to reduce transmitted light , as well as direct more reflected light back to the observer, as suggested by Figure 2e.

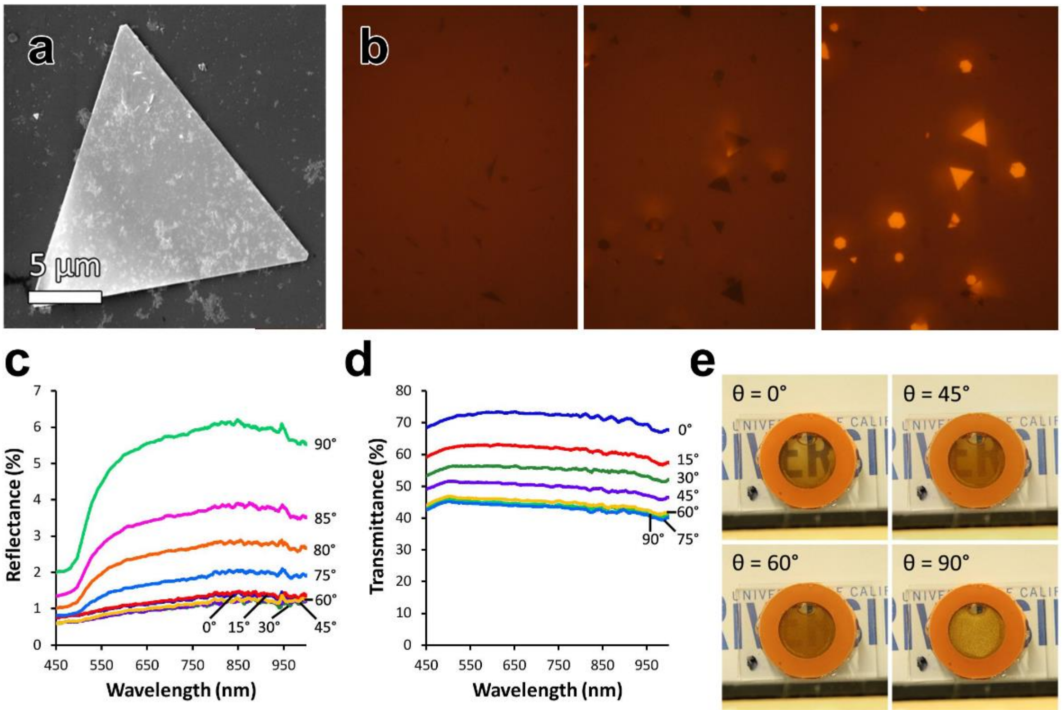

**Figure 1.6** (a) SEM images of gold microplates with magnetic nanoparticle deposition; (b) Optical microscopy images of gold microplates under an applied magnetic field with varying orientations relative to the viewing directions: 0°, 45°, and 90°, from left to right; (c) Reflectance spectrum of a dispersion of gold microplates exposed to a magnetic field oriented at various angles (from 0° to 90°) relative to the path of the incident light; (d) Transmittance spectrum of a dispersion of gold microplates exposed to a magnetic field oriented at various angles (from 0° to 90°) relative to the path of the incident light; (e) Digital photographs of a bulk gold microplate solution under an applied magnetic field with various orientations ($\theta$) relative to the viewing direction.

### 1.4.3 Anisotropic Structures for Light Interference Modulation

If the thickness of the planar structures is comparable to the wavelength of visible light, structural colors will be observed as a result of the interference between incident light reflected by the upper and lower interfaces of planar structures. Thin-film interference is common in the natural world as exemplified by soap bubbles and oil films. Unlike the colors from organic dyes or pigments, interference colors are free from bleaching, and allow for considerably longer lifetime in real applications associated with colorful displays.[88-90] The active tuning of interference colors represents for one important mechanism for the modulation of light in its wavelengths.[91]

The magnetic modulation of light interference has been successfully demonstrated using magnetically responsive polystyrene microplates.[92] These microplates were fabricated from tiny $Fe_3O_4$ nanocrystals (less than 10 nm) through a template-directed assembly method. The interference colors of microplates are highly dependent on their thicknesses, and can be tuned from red to blue by modifying the experimental parameters, for instance, the original amount of $Fe_3O_4$ nanocrystals, as shown in Figure 3c – 3e. These microplates exhibit satisfactory response to external magnetic fields after being dispersed into a liquid medium. They spontaneously align their plane parallel to the field directions. The reflectance spectrum of one typical microplate at an incident angle of 0° showed a series of diffraction maxima and minima in the visible and near-IR range, a phenomenon that is typical for thin-film interference (Figure 3f). All the peaks and valleys were assigned to different orders of constructive and destructive interferences, respectively. With an increase of the incident angle to 3°, the peak and valley positions of the same interference orders shifted to shorter wavelengths, as indicated in Figure 3g. The angular-dependent optical properties were further demonstrated by the continued blueshift of the peaks and valleys at even higher incident angles of 9° and 15°.

The rotation of one single plate upon the application of an external magnetic field was monitored under a dark-field optical microscope. In the absence of a magnetic field, the plates lie flat with their main axis parallel to the substrate due to gravity. Therefore, the reflected light does not travel along the observation direction and no interference color can be observed. Instead, only random scattered light is visible from the plate (Figure 3h). When a magnetic field is applied at an angle 15° offset from the horizontal, the plate aligns its main axis parallel to the field to minimize its magnetostatic potential, so that the reflected light goes into the objective lens and its vivid structural color can be observed (Figure 3h). Such “ON / OFF” color switching of microplates is very convenient to be achieved by magnetically controlling their orientations. Further optimization of this light interference modulation system and its integration with existing optical devices will enable a wide range of chromatic display applications in various fields.

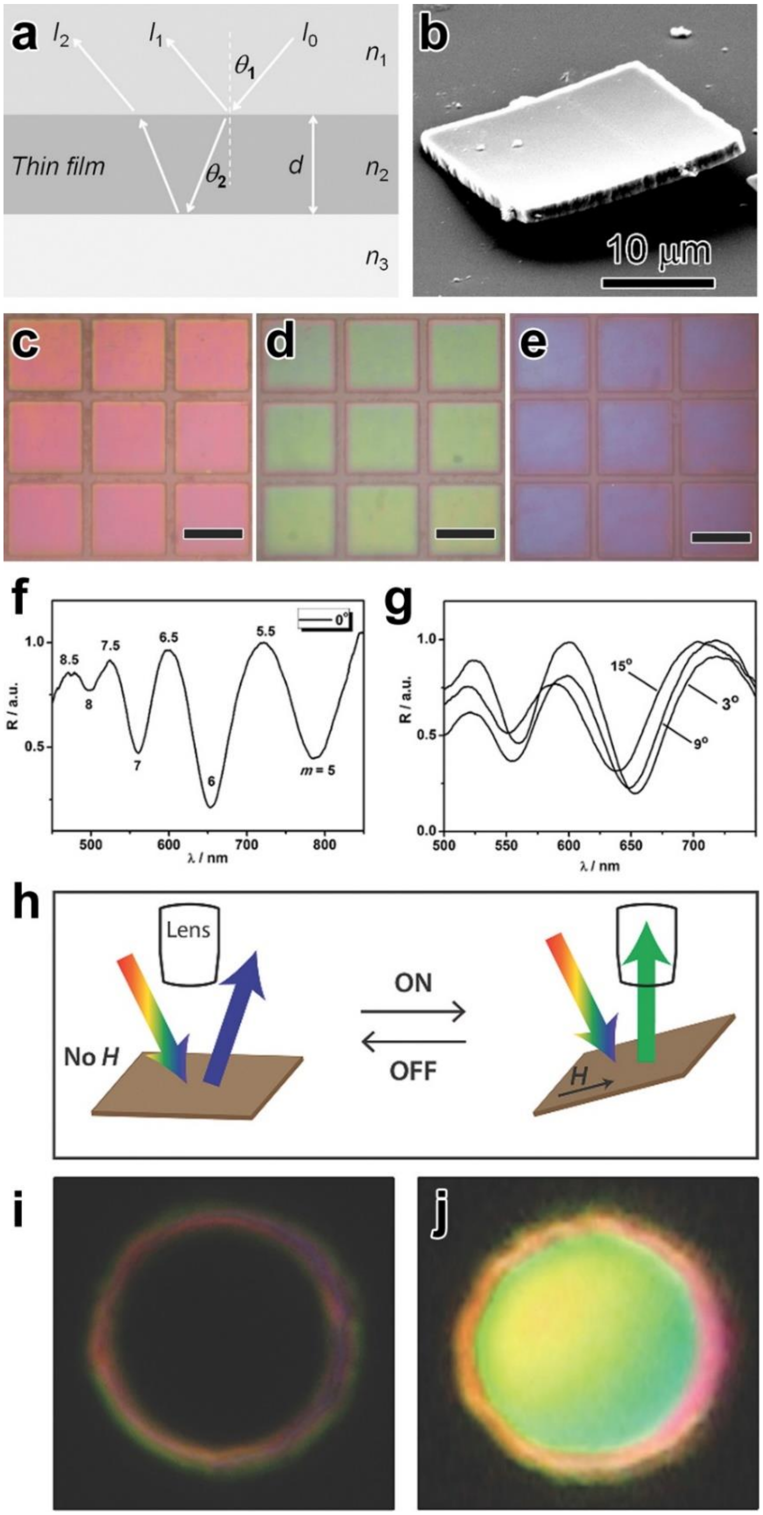
a
$I_2$
$I_1$
$I_0$
$\theta_1$
$n_1$
Thin film
$\theta_2$
d
$n_2$
$n_3$
b
10 μm
c
d
e
f
R / a.u.
1.0
0.5
8.5
8
7.5
7
6.5
6
5.5
m = 5
0°
500
600
700
800
λ / nm
g
R / a.u.
0.0
0.5
1.0
15°
3°
9°
500
550
600
650
700
λ / nm
h
Lens
No H
ON
OFF
H
i
j

**Figure 1.7** (a) Schematic illustration of thin film interference. The light reflected from the upper and lower interfaces ($I_1$ and $I_2$) interfere with one another to form a new wave. $\theta_1$ is the incident angle, while $\theta_2$ responds to the diffractive angle; (b) A representative TEM image of a single microplate; (c-e) Bright-field optical images of dried nanocrystal thin plates with different thicknesses formed against the same square-shape template. Scale bar: 20 µm; (f) Reflectance spectrum of a typical nanocrystal thin-film microplate at an incident angle of 0°; (g) Reflectance spectrum of a typical nanocrystal thin-film microplate at an incident angle of 3°, 9° and 15°; (h) Schematic illustration of the ON/OFF switch of the diffractions of a thin microplate observed under a dark-field optical microscope; (i) The reflected light does not travel along the observation direction, corresponding to an "OFF" state; (j) The observed structural color of the microplate when a magnetic field of 15° offset from the horizontal direction is applied, corresponding to an "ON" state.

## 1.5 Scope of This Dissertation

Despite the tremendous progress made in the development of magnetic-field-guided assembly strategies, the potential of the magnetic assembly has not been fully exploited, and a number of challenges still present. For example, current magnetic assembly processes were more or less limited to spherical, isotropic building blocks; while very limited effort has been made to the assembly of anisotropic building blocks, which, however, hold great promise as they often possess shape-dependent physical and chemical properties and add more degrees of freedom for manipulating the collective properties of the resultant superstructures.

This dissertation summarized my explorations in the magnetic assembly of anisotropic nanostructures, from their controlled synthesis to guided assembly, with special emphasis on the collective optical property of the as-assembled structures and their potential applications in optical devices. In **Chapter 2**, I discussed about a new type of magnetically responsive photonic ink with fast response, good reversibility and bi-stability based on 1D photonic nanochains. Each chain can be treated as an anisotropic magnetic particle, and it spontaneously align along the field direction upon the application of an external magnetic field. Owing to the periodical arrangement of magnetite and silica along their long axis, these nanochains exhibited angular-dependent photonic property and were exploited as basic color units for the photonic ink. The photonic response of the ink could be rapidly and repetitively switched “on” and “off” by tuning the direction of external magnetic fields. More importantly, when highly viscous solvents were introduced as dispersants, temporary bi-stability was achieved in the photonic ink, as the rotations of nanochains were suppressed, and they were allowed to stay temporary aligned after the removal of external magnetic field and to retain their photonic response for a considerably long period. The effects of the lengths of nanochains was also investigated. It was found that the bi-stability of photonic inks enhanced as the nanochains became longer. By designatedly choosing nanochains with different lengths, the fabrication of inks with more sophisticated color expression was also demonstrated.

In **Chapter 3**, I demonstrated the synthesis of anisotropic Fe@$SiO_2$ nanoellipsoids and their self-assembly into a new class of magnetically responsive photonic structures. In contrast to the conventional colloidal crystals made from spherical particles where dynamic tuning of photonic property is mainly achieved by controlling the field strength, the photonic property of novel colloidal crystals assembled from these highly uniform shape- and magnetically anisotropic nanoellipsoids can be dynamically tuned by controlling the direction of magnetic fields. These novel photonic structures diffracted incident light at a minimum wavelength when the field direction was perpendicular to the incident angle, as the periodicity of photonic structure was determined by the shorter axis of nanoellipsoids under this situation. When the field direction was parallel to the incident angle, the orientation of nanoelliposoids changed, and the periodicity of photonic structure was then determined by the longer axis of nanoellipsoids. As a result, they diffracted incident light at a maximum wavelength. I also investigated the effect of field strength. I found that it only affected the intensity of diffracted light, as the orientation of nanoellipsoids became more uniform and the positional order of photonic structures was improved.

In **Chapter 4**, I continued my investigation on the self-assembly of anisotropic magnetic nanoparticles, but with more elongated building blocks. I started with the synthesis of anisotropic $Fe_3O_4$@$SiO_2$ nanorods with larger aspect ratios, and studied their self-organization into liquid crystal phases under high volume fractions. The optical property of the resultant liquid crystals were demonstrated to be instantaneously and reversibly tuned with external magnetic fields. Depending on the direction of the applied external field, the resultant liquid crystal alters the polarization of light and is thus able to control the intensity of the light transmitted through it. Optical switching tests indicated that this liquid crystal is extremely sensitive to the directional change of external magnetic fields, and exhibits an instant response within 0.01 s. Combining with a UV curable resin, the magnetically responsive liquid crystals can be made into thin films, which orientations can be fixed completely or in selected areas by combining magnetic alignment and lithography processes, allowing the creation of patterns of different polarizations and control over the transmittance of light in particular areas.

In **Chapter 5**, I further extended the magnetic tuning mechanism into the tuning of non-magnetic nanomaterials, with gold nanorods being chosen for demonstration. Magnetic orientational control of the gold nanorods was achieved by attaching them to superparamagnetic iron oxide nanorods in a parallel manner, so that the resultant hybrid nanostructure aligned themselves parallel to the direction of external magnetic field upon its application. I then demonstrated the magnetic control of the excitation of plasmonic modes of gold nanorods. Depending on the angles between them and the field directions, the excitation magnitude of gold nanorods' transverse plasmon and longitudinal plasmon could be gradually tuned. As a result, the colloidal dispersion of AuNRs showed color switching in response to the changes in the orientation or strength of external magnetic fields. Such tuning is instant and reversible, and can be operated under considerably weak magnetic fields or alternating magnetic fields with high frequency, as suggested by optical switching tests. This strategy is expected to be extended to magnetic tuning of other anisotropic plasmonic nanostructures.

### 1.6 Reference

1. Bishop, K.J.M., et al., *Nanoscale Forces and Their Uses in Self-Assembly*. Small, 2009. **5**(14): p. 1600-1630.

2. Glotzer, S.C. and M.J. Solomon, *Anisotropy of building blocks and their assembly into complex structures*. Nature Materials, 2007. **6**(8): p. 557-562.

3. Li, M., H. Schnablegger, and S. Mann, *Coupled synthesis and self-assembly of nanoparticles to give structures with controlled organization*. Nature, 1999. **402**(6760): p. 393-395.

4. Mirkin, C.A., et al., *A DNA-based method for rationally assembling nanoparticles into macroscopic materials*. Nature, 1996. **382**(6592): p. 607-609.

5. Velev, O.D., A.M. Lenhoff, and E.W. Kaler, *A class of microstructured particles through colloidal crystallization*. Science, 2000. **287**(5461): p. 2240-2243.

6. Whitesides, G.M. and B. Grzybowski, *Self-assembly at all scales*. Science, 2002. **295**(5564): p. 2418-2421.

7. Dinsmore, A.D., et al., *Colloidosomes: Selectively permeable capsules composed of colloidal particles*. Science, 2002. **298**(5595): p. 1006-1009.

8. Freeman, R.G., et al., *Self-Assembled Metal Colloid Monolayers - an Approach to Sers Substrates*. Science, 1995. **267**(5204): p. 1629-1632.

9. Redl, F.X., et al., *Three-dimensional binary superlattices of magnetic nanocrystals and semiconductor quantum dots*. Nature, 2003. **423**(6943): p. 968-971.

10. Shevchenko, E.V., et al., *Structural diversity in binary nanoparticle superlattices*. Nature, 2006. **439**(7072): p. 55-59.

11. Vlasov, Y.A., et al., *On-chip natural assembly of silicon photonic bandgap crystals*. Nature, 2001. **414**(6861): p. 289-293.

12. Xia, Y.N., B. Gates, and Z.Y. Li, *Self-assembly approaches to three-dimensional photonic crystals*. Advanced Materials, 2001. **13**(6): p. 409-413.

13. Sun, S.H. and C.B. Murray, *Synthesis of monodisperse cobalt nanocrystals and their assembly into magnetic superlattices (invited)*. Journal of Applied Physics, 1999. **85**(8): p. 4325-4330.

14. Zerrouki, D., et al., *Chiral colloidal clusters*. Nature, 2008. **455**(7211): p. 380-382.

15. Moon, H.J., et al., *Temperature-responsive compounds as in situ gelling biomedical materials*. Chemical Society Reviews, 2012. **41**(14): p. 4860-4883.

16. Liu, W.G., et al., *A rapid temperature-responsive sol-gel reversible poly(N-isopropylacrylamide)-g-methylcellulose copolymer hydrogel*. Biomaterials, 2004. **25**(15): p. 3005-3012.

17. Schumers, J.M., C.A. Fustin, and J.F. Gohy, *Light-Responsive Block Copolymers*. Macromolecular Rapid Communications, 2010. **31**(18): p. 1588-1607.

18. Alvarez-Lorenzo, C., L. Bromberg, and A. Concheiro, *Light-sensitive Intelligent Drug Delivery Systems*. Photochemistry and Photobiology, 2009. **85**(4): p. 848-860.

19. Sidorenko, A., et al., *Reversible switching of hydrogel-actuated nanostructures into complex micropatterns*. Science, 2007. **315**(5811): p. 487-490.

20. Ge, J.P., et al., *Rewritable Photonic Paper with Hygroscopic Salt Solution as Ink*. Advanced Materials, 2009. **21**(42): p. 4259-+.

21. Arsenault, A.C., et al., *From colour fingerprinting to the control of photoluminescence in elastic photonic crystals*. Nature Materials, 2006. **5**(3): p. 179-184.

22. Kim, S.Y. and Y.M. Lee, *Drug release behavior of electrical responsive poly(vinyl alcohol)/poly(acrylic acid) IPN hydrogels under an electric stimulus*. Journal of Applied Polymer Science, 1999. **74**(7): p. 1752-1761.

23. Ge, J., et al., *Drug Release from Electric-Field-Responsive Nanoparticles*. Acs Nano, 2012. **6**(1): p. 227-233.

24. Li, H., et al., *Model development and numerical simulation of electric-stimulus-responsive hydrogels subject to an externally applied electric field*. Biosensors & Bioelectronics, 2004. **19**(9): p. 1097-1107.

25. Medeiros, S.F., et al., *Stimuli-responsive magnetic particles for biomedical applications*. International Journal of Pharmaceutics, 2011. **403**(1-2): p. 139-161.

26. Filipcsei, G., et al., *Magnetic field-responsive smart polymer composites*. Oligomers Polymer Composties Molecular Imprinting, 2007. **206**: p. 137-189.

27. He, L., et al., *Magnetic Assembly Route to Colloidal Responsive Photonic Nanostructures*. Accounts of Chemical Research, 2012. **45**(9): p. 1431-1440.

28. Yan, X.Z., et al., *Stimuli-responsive supramolecular polymeric materials*. Chemical Society Reviews, 2012. **41**(18): p. 6042-6065.

29. Popat, A., et al., *Enzyme-Responsive Controlled Release of Covalently Bound Prodrug from Functional Mesoporous Silica Nanospheres*. Angewandte Chemie-International Edition, 2012. **51**(50): p. 12486-12489.

30. Zhao, B. and J.S. Moore, *Fast pH- and ionic strength-responsive hydrogels in microchannels*. Langmuir, 2001. **17**(16): p. 4758-4763.

31. Markland, P., et al., *A pH- and ionic strength-responsive polypeptide hydrogel: Synthesis, characterization, and preliminary protein release studies*. Journal of Biomedical Materials Research, 1999. **47**(4): p. 595-602.

32. Solomatin, S.V., et al., *Environmentally responsive nanoparticles from block ionomer complexes: Effects of pH and ionic strength*. Langmuir, 2003. **19**(19): p. 8069-8076.

33. Carrick, L.M., et al., *Effect of ionic strength on the self-assembly, morphology and gelation of pH responsive beta-sheet tape-forming peptides*. Tetrahedron, 2007. **63**(31): p. 7457-7467.

34. Zhang, K.P., Y.L. Luo, and Z.Q. Li, *Synthesis and characterization of a pH- and ionic strength-responsive hydrogel*. Soft Materials, 2007. **5**(4): p. 183-195.

35. Ge, J.P., et al., *Assembly of Magnetically Tunable Photonic Crystals in Nonpolar Solvents*. Journal of the American Chemical Society, 2009. **131**(10): p. 3484-+.

36. Ge, J.P., Y.X. Hu, and Y.D. Yin, *Highly tunable superparamagnetic colloidal photonic crystals*. Angewandte Chemie-International Edition, 2007. **46**(39): p. 7428-7431.

37. Ge, J.P. and Y.D. Yin, *Magnetically tunable colloidal photonic structures in alkanol solutions*. Advanced Materials, 2008. **20**(18): p. 3485-+.

38. Xu, X.L., et al., *Superparamagnetic photonic crystals*. Advanced Materials, 2001. **13**(22): p. 1681-1684.

39. Xu, X.L., S.A. Majetich, and S.A. Asher, *Mesoscopic monodisperse ferromagnetic colloids enable magnetically controlled photonic crystals*. Journal of the American Chemical Society, 2002. **124**(46): p. 13864-13868.

40. Chorny, M., et al., *Targeting stents with local delivery of paclitaxel-loaded magnetic nanoparticles using uniform fields*. Proceedings of the National Academy of Sciences of the United States of America, 2010. **107**(18): p. 8346-8351.

41. Forbes, Z.G., et al., *An approach to targeted drug delivery based on uniform magnetic fields*. Ieee Transactions on Magnetics, 2003. **39**(5): p. 3372-3377.

42. Li, K.H. and B.B. Yellen, *Magnetically tunable self-assembly of colloidal rings*. Applied Physics Letters, 2010. **97**(8).

43. Ooi, C., R.M. Erb, and B.B. Yellen, *On the controllability of nanorod alignment in magnetic fluids*. Journal of Applied Physics, 2008. **103**(7).

44. Yellen, B.B. and G. Friedman, *Analysis of repulsive interactions in chains of superparamagnetic colloidal particles for magnetic template-based self-assembly*. Journal of Applied Physics, 2003. **93**(10): p. 8447-8449.

45. Yellen, B.B. and G. Friedman, *Programmable assembly of colloidal particles using magnetic microwell templates*. Langmuir, 2004. **20**(7): p. 2553-2559.

46. Yellen, B.B., O. Hovorka, and G. Friedman, *Arranging matter by magnetic nanoparticle assemblers*. Proceedings of the National Academy of Sciences of the United States of America, 2005. **102**(25): p. 8860-8864.

47. Mirica, K.A., et al., *Magnetic Levitation in the Analysis of Foods and Water*. Journal of Agricultural and Food Chemistry, 2010. **58**(11): p. 6565-6569.

48. Mirica, K.A., et al., *Using Magnetic Levitation To Distinguish Atomic-Level Differences in Chemical Composition of Polymers, and To Monitor Chemical Reactions on Solid Supports*. Journal of the American Chemical Society, 2008. **130**(52): p. 17678-+.

49. Mirica, K.A., et al., *Measuring Densities of Solids and Liquids Using Magnetic Levitation: Fundamentals*. Journal of the American Chemical Society, 2009. **131**(29): p. 10049-10058.

50. Shapiro, N.D., et al., *Measuring Binding of Protein to Gel-Bound Ligands Using Magnetic Levitation*. Journal of the American Chemical Society, 2012. **134**(12): p. 5637-5646.

51. Kraftmakher, Y., *Magnetic field of a dipole and the dipole-dipole interaction*. European Journal of Physics, 2007. **28**(3): p. 409-414.

52. Ge, J.P. and Y.D. Yin, *Responsive Photonic Crystals*. Angewandte Chemie-International Edition, 2011. **50**(7): p. 1492-1522.

53. Hu, Y.X., L. He, and Y.D. Yin, *Magnetically Responsive Photonic Nanochains*. Angewandte Chemie-International Edition, 2011. **50**(16): p. 3747-3750.

54. Erb, R.M., et al., *Magnetic assembly of colloidal superstructures with multipole symmetry*. Nature, 2009. **457**(7232): p. 999-1002.

55. He, L., et al., *Magnetic Assembly and Patterning of General Nanoscale Materials through Nonmagnetic Templates*. Nano Letters, 2012. **13**(1): p. 264-271.

56. Wang, M.S., L. He, and Y.D. Yin, *Magnetic field guided colloidal assembly*. Materials Today, 2013. **16**(4): p. 110-116.

57. Damon, R.W. and J.R. Eshbach, *Magnetostatic Modes of a Ferromagnet Slab*. Journal of Physics and Chemistry of Solids, 1961. **19**(3-4): p. 308-320.

58. Beleggia, M., et al., *On the magnetostatic interactions between nanoparticles of arbitrary shape*. Journal of Magnetism and Magnetic Materials, 2004. **278**(1-2): p. 270-284.

59. Ignatchenko, V.A., I.S. Edelman, and D.A. Petrov, *Magnetostatic fields in planar assemblies of magnetic nanoparticles*. Physical Review B, 2010. **81**(5): p. 054419.

60. Kasperski, M., *Magnetostatic modes in a uniform magnetic nanorod*. Journal of Applied Physics, 2014. **116**(14): p. 143904.

61. Joseph, R.I. and E. Schlomann, *Theory of Magnetostatic Modes in Long, Axially Magnetized Cylinders*. Journal of Applied Physics, 1961. **32**(6): p. 1001-1005.

62. Vi, K. and M.A. Sigal, *Magnetostatic Waves in a Thin Uniaxial Platelet with Stripe Domains Magnetized Along the Easy Axis*. Physica Status Solidi b-Basic Solid State Physics, 1992. **170**(2): p. 569-584.

63. Sigal, M.A. and V.I. Kostenko, *Magnetostatic Modes in a Thin Uniaxial Platelet with Bubble Lattice at Normal Magnetization*. Physica Status Solidi a-Applied Research, 1991. **128**(1): p. 219-234.

64. Craik, D.J. and P.V. Cooper, *Criteria for Uniaxial Magnetostatic Behavior in Thin Platelets*. Physics Letters A, 1972. **A 41**(3): p. 255-256.

65. Guo, L., et al., *Uniform magnetic chains of hollow cobalt mesospheres from one-pot synthesis and their assembly in solution*. Advanced Functional Materials, 2007. **17**(3): p. 425-430.

66. Zhang, Y., et al., *The Shape Anisotropy in the Magnetic Field-Assisted Self-Assembly Chain-like Structure of Magnetite*. Journal of Physical Chemistry C, 2009. **113**(19): p. 8152-8157.

67. Ge, J.P., et al., *Superparamagnetic magnetite colloidal nanocrystal clusters*. Angewandte Chemie-International Edition, 2007. **46**(23): p. 4342-4345.

68. Zhang, Q., et al., *Photonic Labyrinths: Two-Dimensional Dynamic Magnetic Assembly and in Situ Solidification*. Nano Letters, 2013. **13**(4): p. 1770-1775.

69. He, L., et al., *Self-assembly and magnetically induced phase transition of three-dimensional colloidal photonic crystals*. Nanoscale, 2012. **4**(15): p. 4438-4442.

70. Ingram, A.L. and A.R. Parker, *A review of the diversity and evolution of photonic structures in butterflies, incorporating the work of John Huxley (The Natural History Museum, London from 1961 to 1990)*. Philosophical Transactions of the Royal Society B-Biological Sciences, 2008. **363**(1502): p. 2465-2480.

71. Galusha, J.W., et al., *Study of natural photonic crystals in beetle scales and their conversion into inorganic structures via a sol-gel bio-templating route*. Journal of Materials Chemistry, 2010. **20**(7): p. 1277-1284.

72. Forster, J.D., et al., *Assembly of Optical-Scale Dumbbells into Dense Photonic Crystals*. Acs Nano, 2011. **5**(8): p. 6695-6700.

73. Lee, S.H. and C.M. Liddell, *Anisotropic Magnetic Colloids: A Strategy to Form Complex Structures Using Nonspherical Building Blocks*. Small, 2009. **5**(17): p. 1957-1962.

74. Liddell, C.M. and C.J. Summers, *Nonspherical ZnS colloidal building blocks for three-dimensional photonic crystals*. Journal of Colloid and Interface Science, 2004. **274**(1): p. 103-106.

75. Hosein, I.D., S.H. Lee, and C.M. Liddell, *Dimer-Based Three-Dimensional Photonic Crystals*. Advanced Functional Materials, 2010. **20**(18): p. 3085-3091.

76. Ding, T., et al., *Fabrication of 3D Photonic Crystals of Ellipsoids: Convective Self-Assembly in Magnetic Field*. Advanced Materials, 2009. **21**(19): p. 1936-1940.

77. Hu, Y.D., et al., *Janus Photonic Crystal Microspheres: Centrifugation-Assisted Generation and Reversible Optical Property*. Langmuir, 2013. **29**(50): p. 15529-15534.

78. Hu, Y.D., et al., *Microfluidic Fabrication and Thermoreversible Response of Core/Shell Photonic Crystalline Microspheres Based on Deformable Nanogels*. Langmuir, 2012. **28**(49): p. 17186-17192.

79. Li, J., et al., *Field modulation of light transmission through ferrofluid film*. Applied Physics Letters, 2007. **91**(25): p. 253108.

80. Fan, F., et al., *Magnetically tunable terahertz magnetoplasmons in ferrofluid-filled photonic crystals*. Applied Physics Letters, 2013. **103**(16): p. 161115.

81. Chen, S., et al., *Tunable optical and magneto-optical properties of ferrofluid in the terahertz regime*. Optics Express, 2014. **22**(6): p. 6313-6321.

82. Ye, M.M., et al., *Self-assembly of superparamagnetic magnetite particles into peapod-like structures and their application in optical modulation*. Journal of Materials Chemistry, 2010. **20**(37): p. 7965-7969.

83. Zorba, S., et al., *Superparamagnetic Magnetite Nanoparticle Superstructures for Optical Modulation/Chopping*. Journal of Physical Chemistry C, 2010. **114**(41): p. 17868-17873.

84. Erb, R.M., et al., *Locally Reinforced Polymer-Based Composites for Elastic Electronics*. Acs Applied Materials & Interfaces, 2012. **4**(6): p. 2860-2864.

85. Mao, Y.W., J. Liu, and J.P. Ge, *Tuning the Transmittance of Colloidal Solution by Changing the Orientation of Ag Nanoplates in Ferrofluid*. Langmuir, 2012. **28**(36): p. 13112-13117.

86. Bubenhofer, S.B., et al., *Magnetic switching of optical reflectivity in nanomagnet/micromirror suspensions: colloid displays as a potential alternative to liquid crystal displays*. Nanotechnology, 2009. **20**(48): p. 485302.

87. Goebl, J., et al., *Magnetically tunable colloidal micromirrors*. Nanoscale Horizons, 2016. **1**(1): p. 64-68.

88. Gu, Z.Z., et al., *Structural color and the lotus effect*. Angewandte Chemie-International Edition, 2003. **42**(8): p. 894-897.

89. Kinoshita, S. and S. Yoshioka, *Structural colors in nature: The role of regularity and irregularity in the structure*. Chemphyschem, 2005. **6**(8): p. 1442-1459.

90. Parker, A.R., *515 million years of structural colour*. Journal of Optics A-Pure and Applied Optics, 2000. **2**(6): p. R15-R28.

91. Lezec, H.J., et al., *Submicrometer dimple array based interference color field displays and sensors*. Nano Letters, 2007. **7**(2): p. 329-333.

92. He, L., et al., *Magnetochromatic Thin-Film Microplates*. Advanced Materials, 2015. **27**(1): p. 86-92.

# Chapter 2

## Magnetically Rewritable Photonic Ink Based on 1D Nanochains

### 2.1 Introduction

Photonic materials are very common in nature. For example, the iridescent colors displayed in the wings of Morpho butterflies and peacocks were found to result from a different mechanism from that of dyes or pigments, which produce colors by the absorption of light to excite an electron between the ground and excited state of the chromophore. In contrast, the color in photonic structures has a more physical origin that stems from the modulation of photon motions when light travels through their periodic nanostructures. Such unique colors originating from the interaction of light with periodically arranged structures of dielectric materials are often named as structural colors, which are iridescent and metallic, cannot be mimicked by chemical dyes or pigments, and free from photo-bleaching.

Structural-colored photonic materials with band gaps located in the visible regime have been considered as important chromatic materials. Among different version of photonic materials, photonic papers and inks are of particular interest in marketplace. Unlike the backlit LCD type displays which emit light, electronic paper based displays reflect light and do not need to undergo frequent refreshing during use so they are significantly more energy efficient. Because they do not emit light, they are also free of glare under strong illumination such as sunlight, making them superior to other emissive display technologies, especially for outdoor applications, such as e-book readers and billboards.[1-4]

A commonly desired feature for electronic paper is self- maintenance of property - bi-stability - for the purposes of recording visual information for a considerably long period and avoiding the energy cost for constant refreshing. In a bi-stable system, energy is only consumed during occasional refreshing; afterwards the information displayed by the electronic paper will be kept for minutes or even longer without the need of any energy input. The first generation of electronic papers are composed of microcapsules containing positively charged black and negatively charged white particles which, upon the application of an electric field, migrate to the oppositely charged electrodes and therefore display black and white patterns.[5, 6] These particles will not immediately migrate back to their original positions after the removal of electric field so that the black-white information recorded in the microcapsules kept recognizable over an extended period. The remaining challenges of this type of electronic papers include relatively slow response and lack of the ability to display color contents.

Lots of efforts have been devoted into the development of photonic inks and papers which display structural colors, although many such systems still have difficulties to create bi-stability.[7-13] In the cases that bi-stability can be established, the stimuli usually involve slow processes such as solvent swelling or heat transport so that instant writing of arbitrary patterns remains a challenge.[14-18] In this chapter, I demonstrated the feasibility of using superparamagnetic 1D nanochains for fabricating rewritable photonic inks that can record visual information under magnetic fields. 1D photonic nanochains containing periodically arranged magnetic spheres along their long axis are used as the basic color units, which can be magnetically switched on and off very rapidly.[19] Only if they are aligned parallel to the viewing angle by the magnetic field, incident light can be diffracted and strong photonic response can be observed, corresponding to an "On" state, otherwise no diffraction occurs and nanochains only show the native brown color of magnetite, corresponding to an "Off" state. The "On" state can be maintained for different lengths of period by controlling the length of the nanochains or the viscosity of the solvents. In solvents with high viscosities, the rotational movements of nanochains are limited so that they can stay temporary aligned after the removal of external magnetic field and retain their photonic response for a considerably long period.

## 2.2 Synthesis and Characterization

***Chemicals.*** Ethanol (denatured), anhydrous iron(III) chloride, ammonium hydroxide (28-30 % solution in water), tetraethyl orthosilicate (TEOS), sodium hydroxide, ethylene glycol (EG), tetraethylene glycol (TEG), polyethylene glycol 400 (PEG 400) and glycerol were purchased from Fisher Scientific. Polyacrylic acid (PAA, MW = 1800) and diethylene glycol (DEG) were obtained from Sigma-Aldrich. All chemicals were directly used as received without further treatment. Deionized water was used for all the solution preparations and reactions.

***Synthesis of magnetite colloidal nanoclusters (CNCs).*** A $FeCl_3$ in DEG stock solution was prepared by dissolving $FeCl_3$ (2 mmol) in DEG (50 mL); this solution was heated at 80 °C for 1 hr under nitrogen, cooled, and stored under room temperature. A NaOH in DEG stock solution was prepared by dissolving NaOH (50 mmol) in DEG (20 mL); this solution was heated at 120 °C for 1 hr under nitrogen, cooled, and stored in an oven at 70 °C. For the synthesis of 130 nm CNCs, a mixture of 0.288 g of PAA, 1 mL of $FeCl_3$ stock solution and 17 mL of DEG was heated to 220 °C in a nitrogen atmosphere with vigorous stirring to form a transparent, light yellow solution. After 1.5 hrs, 1.75 mL of NaOH stock solution was injected rapidly into the above hot mixture, and the temperature dropped to about 210 °C instantly. The reaction solution slowly turned black after about 2 min and became slightly turbid. The reaction mixture was heated for an additional 1 hr and then cooled down to room temperature. The final products were centrifuged and washed with a mixture of water and ethanol for at least three times, and then dispersed in 3 mL of water. For the synthesis of 110 nm CNCs, all the experimental condition were kept the same, except that the volume of NaOH stock solution was adjusted to 1.70 mL. For the synthesis of 150 nm CNCs, all the experimental condition were kept the same, except that the volume of NaOH stock solution was adjusted to 1.80 mL.

***Synthesis of 1D photonic nanochains.*** The optical property of photonic nanochains are determined by the size of initial CNCs. Generally, when 110 nm CNCs were used, the resultant photonic nanochains reflected blue light; when 130 nm CNCs were used, the resultant photonic nanochains reflected green light; when 150 nm CNCs were used, the resultant photonic nanochains reflected red light. For the synthesis of long green photonic nanochains, 3 mL of aqueous dispersion of 130 nm CNCs was dispersed in a mixture of 1 mL of ammonium hydroxide and 20 mL of ethanol under sonication. The mixture was then transferred into a three-neck flask under mechanical stirring at 600 rpm, and 120 μL of

TEOS was quickly injected. After 12 min, the mixture was transferred to a plastic cup (45 × 65 mm) and placed above a 75 × 6 mm neodymium disc magnet at a distance of 1 cm for 2 s. After removal of the magnetic field, the mixture was allowed to sit undisturbed for another 15 min, after which it was centrifuged, washed with ethanol for three times, and dispersed in water. For the synthesis of short blue photonic nanochains, 3 mL of aqueous dispersion of 110 nm CNCs was dispersed in a mixture of 1 mL of ammonium hydroxide and 20 mL of ethanol under sonication. The mixture was then transferred into a three-neck flask under mechanical stirring at 600 rpm, and 100 μL of TEOS was quickly injected. After 18 min, the mixture was transferred to the same plastic cup and placed above the same neodymium disc magnet at a distance of 1 cm for 1 s. After removal of the magnetic field, the mixture was allowed to sit undisturbed for another 15 min, after which it was centrifuged, washed with ethanol for three times, and dispersed in water.

***Fabrication of bi-stable photonic inks and displays.*** The photonic nanochains were magnetically separated from the above aqueous dispersion. 3 mL of viscous polar solvents such as EG, DEG, PEG 400 and glycerol were added into the photonic nanochains, respectively. The mixture was then vigorously vortexed and sonicated for 30 min. The mixture was injected into a home-made 75 × 50 × 1 mm glass vessel for bi-stable display demonstration.

***Characterization.*** The morphology of the CNCs and 1D nanochains were characterized by a Tecnai T12 transmission electron microscope (TEM) and a Philips FEI XL30 scanning electron microscope (SEM). The diffraction spectra were measured by an Ocean Optics HR 2000CG-UV-NIR spectrometer coupled with a six-around-one reflectionbackscattering probe. The spectra integration time of collecting the signals was set to be 300 ms. A Zeiss AXIO Imager optical microscope connected with a camera was used to take the digital microscope images for 1D nanochains. A permanent magnet was placed underneath the sample stage and could be manually moved vertically to change the distance between it and the sample.

## 2.3 Results and Discussions

The fabrication of 1D photonic chains is based on a previous work from our group. The superparamagnetic $Fe_3O_4$ CNCs are initially coated with a thin layer of silica, assembled into temporary chain-like structures by applying a magnetic field, and these temporary chain-like structures are then further stabilized to permanent nanochains with an additional coating of silica layer. The key to the successful synthesis of nanochains is to induce the 1D assembly of CNCs by brief exposure to external fields during the silica coating process, so that the CNCs stay temporarily connected, allowing additional silica deposition to fix them into mechanically robust rods or wires. The process is highly controllable: the periodicity can be varied by using CNCs of different sizes, the inter-particle spacing can be fine-tuned by adjusting the timing of magnetic field exposure, and the length of the chains can be controlled by changing the duration of the magnetic field exposure. TEM and SEM characterizations of the resultant product in Figure 2.1a and 2.1b clearly revealed its 1D chain-like morphology, which appear in the form of many linearly connected spheres. The core-shell structure can be better observed in the inset of Figure 2.1b. The periodically arranged $Fe_3O_4$ cores and the smooth silica coating can be identified by the contrast between the core and the shell. Note that the magnetic cores are not in direct contact with each other, confirming the initial silica deposition before the chain formation. By tuning the sizes of initial CNCs, the structural colors of the chains can be tuned from blue to red, as demonstrated in Figure 2.1c, 2.1d and 2.1e.

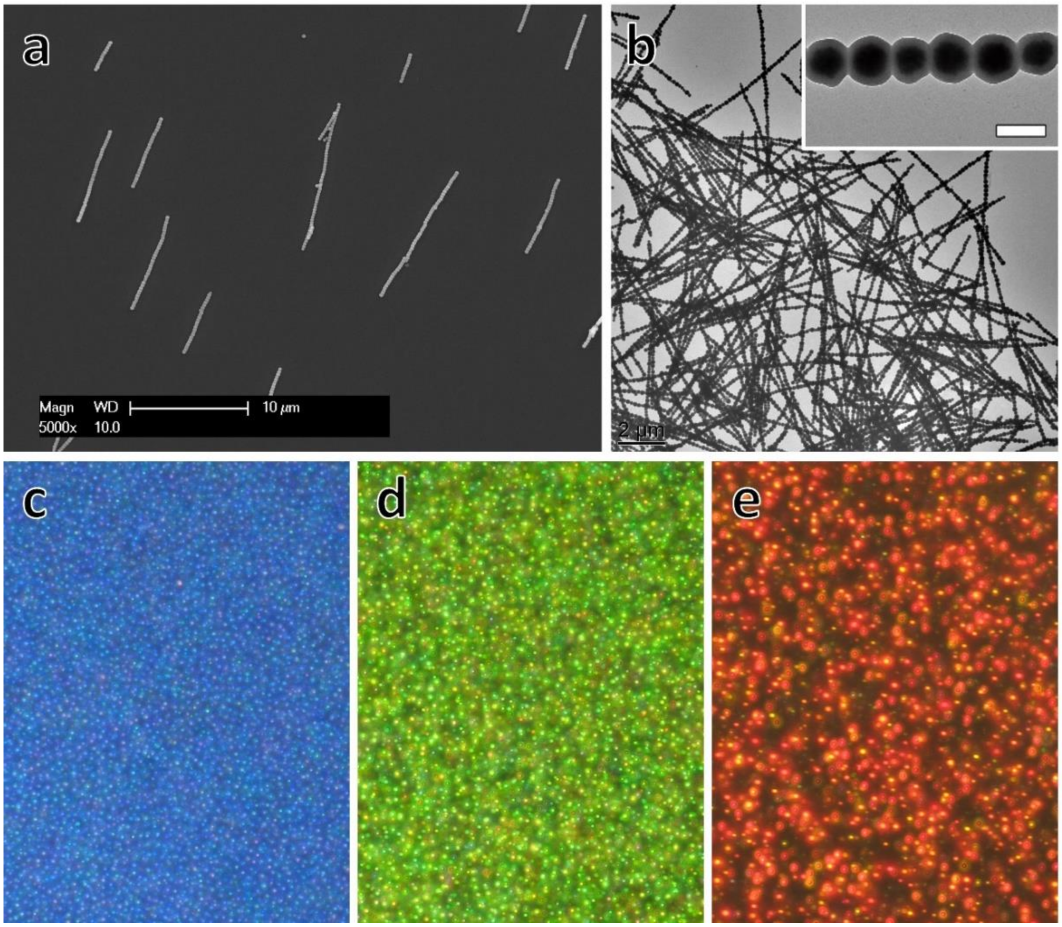

**Figure 2.1** (a) A representative SEM image of nanochains; (b) A representative TEM image of nanochains. Inset: an enlarged TEM image of a single nanochain, scale bar: 200 nm; (c,d,e) Optical images of red, green and blue nanochains in the presence of a magnetic field parallel to the viewing angle.

The periodic arrangement of the $Fe_3O_4$ and silica along their along axis makes these nanochains one of the smallest photonic structures. Their photonic property is, however, highly sensitive to their orientations. Only if they are aligned parallel to the viewing angle, incident light can be diffracted and strong photonic response can be observed; otherwise no diffraction occurs, and nanochains only exhibit the native brownish color of magnetite. Owing to the magnetic substance embedded inside nanochains, their orientations can be conveniently controlled by external magnetic fields. They spontaneously align themselves parallel to the field directions to minimize their magnetostatic energy. As a result, if the field direction is parallel to the viewing angle, the structural colors of photonic nanochains can be observed, corresponding to an "ON" state; otherwise, we can only see their intrinsic brownish color, corresponding to an "OFF" state.

In addition to the magnetic forces, the thermal fluctuation of nanochains and the resistance force from the friction between nanochains and solvent molecules also play an important role in determining the orientation of nanorods, when nanorods are dispersed in a solvent. The magnitude of the following two forces are not comparable to the magnetic forces in the presence of an external magnetic field (the strength of magnetic fields used throughout this chapter is 200 G, unless specified otherwise). As a result, all the nanochains are aligned instantly (less than a second) along the field direction. When the magnetic field is removed, the nanochains naturally rotate away from their original orientations, and their rotational diffusivity is then determined by the competition between the resistance force and their thermal fluctuation. Theoretically, the rotational diffusivity $D_r$ of a Brownian hard rod is given by:[20]

$$D_r = \frac{3k_B T(\ln(L/b) + \gamma)}{\pi \eta L^3}$$

where $k_B$ is Boltzmann's constant, $T$ is temperature in Kelvin, $\eta$ is the solvent viscosity, $L$ and $b$ are the length and diameter of the rod, and $\gamma$ is a correction term.

According to the above equation, the viscosity of the solvent is reversely proportional to the rotational diffusivity of nanorods. It therefore determines the behavior of nanorods, in the absence of external magnetic fields. As the solvent becomes more viscous, the rotational diffusivity of nanorods decreases, and it takes longer time for them to rotate away from their previous orientation. Considering the case that all the nanorods were aligned by an external magnetic field parallel to the viewing angle and the field was then removed, the nanorods dispersed in more viscous solvents were expected to take more time to rotate away from their previous orientation (which is parallel to the viewing angle), and their photonic signals (structural colors) were expected to last for longer consequently (Figure 2.2). For nanorods dispersed in low viscous solvents, they would quickly rotate away from their previous orientation and lose their photonic signal. As a result, only their intrinsic brownish color would be observed.

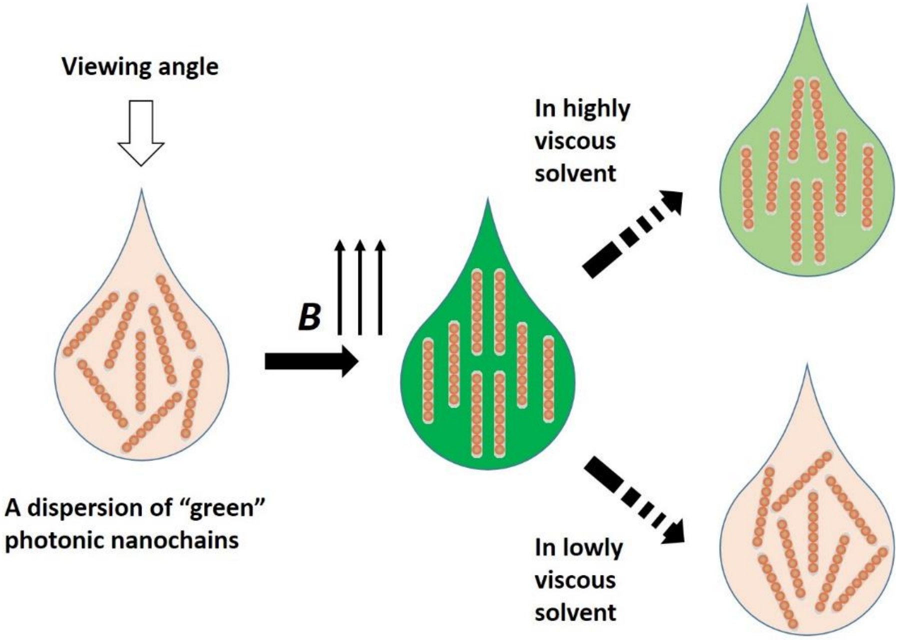

**Figure 2.2** Scheme showing how the viscosities of solvents affect the optical property of a dispersion of "green" photonic nanorods after the removal of magnetic fields.

Owing to the silica shell on their surface, these photonic nanochains can be well dispersed in many polar solvents with different viscosities. The photonic property of nanochains in these solvents were then investigated, with special emphasis on the situations right after the removal of external magnetic fields. Herein I will only discuss the "green" photonic nanochains for simplicity; other photonic nanochains are expected to follow the exactly same principle. The following solvents were chosen: EG, DEG, TEG, PEG 400, and glycerol-water mixtures. In the first step, the nanochains from one batch of synthesis were divided into several portions, and were then dispersed in these solvents, respectively. A magnetic field parallel to the detection angle of the spectrometer was applied to the nanochains dispersions, and their reflection spectra were measured and standardized, as presented in Figure 2.3a. It can be clearly seen that the reflection spectrum of photonic nanochains in water is very different from other solvents. The much broader reflection peak can be attributed to the vigorous thermal fluctuations of nanochains in water, as the viscosity of water is the smallest among these solvents. The peak wavelength of nanochains in water is also the shortest, which can be explained by the Bragg's law that the diffraction wavelength is proportional to the overall refraction index of the system. The reflection spectra of nanochains in other solvents exhibited only small differences in their peak wavelengths. Figure 2.3b clearly reveals this trend, in which the reflection peak wavelengths were plotted against the refractive indexes of solvents.

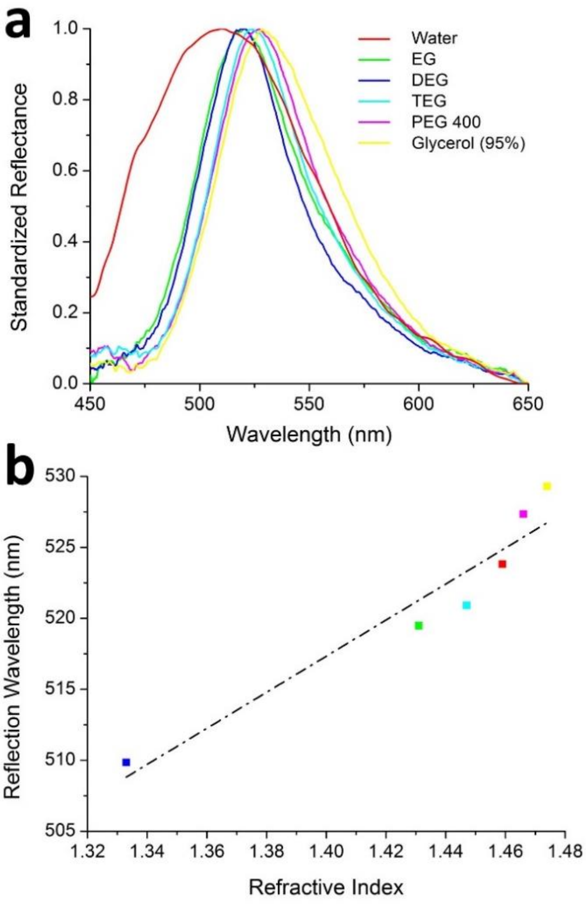

**Figure 2.3** (a) Standardized reflection spectra of the same photonic nanochains in different solvents; (b) A plot of the reflection peak wavelengths against the refractive index of solvents.

In the next step, the magnetic field was removed, and the reflection spectra of photonic nanochains in different solvents were measured against time. Nanochains dispersed in water lost their photonic property almost immediately upon removal of the external magnetic field, therefore their reflection spectrum was not monitored. The reflection spectra of photonic nanochains dispersed in other solvents were presented in Figure 2.4. In addition, glycerol-water mixture with volume fractions of 89%, 91%, 93% and 95% were investigated respectively. For EG which has the smallest viscosity among these solvents, the initial reflectance of the photonic nanochains is ~20% in the presence of a magnetic field, and this value drops to ~10% (about half of the intensity of the initial reflectance) within 6 s after the removal of magnetic field, as shown in Figure 2.4a. For PEG 400 which has a medium viscosity, the time for the reflectance to drop to half of its initial value increases to 60 s, as shown in Figure 2d. In the case of 95% glycerol with the highest viscosity, the elongation in the half-decay time becomes more obvious. The reflectance of the dispersion is still above 10% in 150 s after the removal of magnetic field, as suggested by in Figure 2.4h.

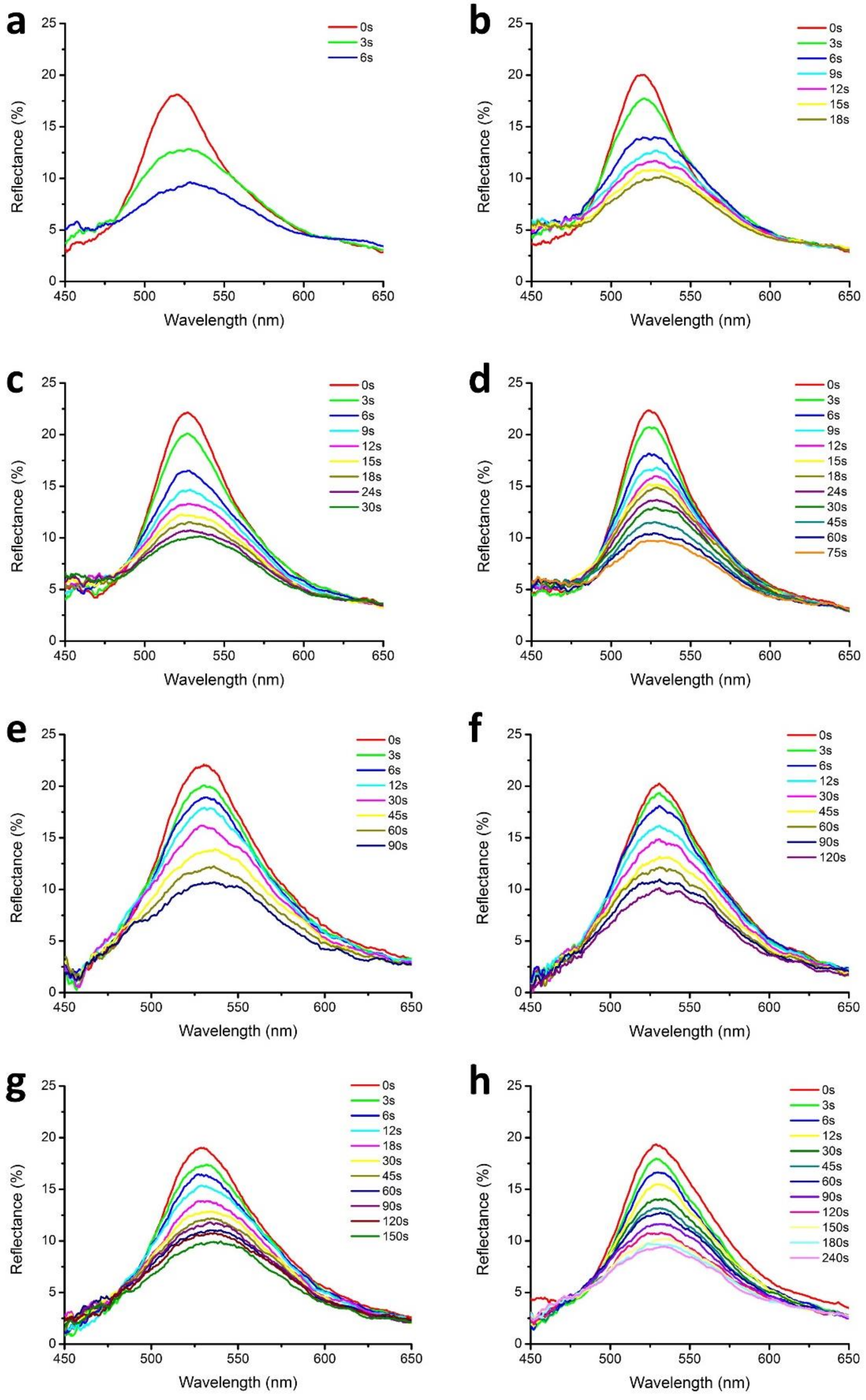

a
b
c
d
e
f
g
h
Reflectance (%)
Wavelength (nm)
0
5
10
15
20
25
450
500
550
600
650
0s
3s
6s
9s
12s
15s
18s
24s
30s
45s
60s
75s
90s
120s
150s
180s
240s

**Figure 2.4** Reflection Spectra of photonic nanochains in (a) EG; (b) DEG; (c) TEG; (d) PEG 400; (e) 89% glycerol solution; (f) 91% glycerol solution; (g) 93% glycerol solution; (h) 95% glycerol solution in certain time periods after the removal of external magnetic fields.

The viscosities of the above solvents were listed in Figure 2.5a. From the plot in Figure 2.5b, the decay half-life of the reflectance were found to monotonously increase with the solvent viscosities, in accordance with the theory. Given that the rotational diffusivities of nanochains are inversely proportional to the solvent viscosities, the Brownian rotation of photonic nanochains is more restricted as the solvent viscosities increase. As a result, their orientation changes slower and their photonic response can be maintained for a longer period.

**a**

| Solvent | Viscosity (mPa·s) |
|---|---|
| Ethylene glycol | 21.18 |
| Diethylene glycol | 38.82 |
| Tetraethylene glycol | 53.24 |
| Polyethylene glycol 400 | 120.75 |
| 90% glycerol in water | 219 |
| 91% glycerol in water | 259 |
| 93% glycerol in water | 367 |
| 95% glycerol in water | 523 |

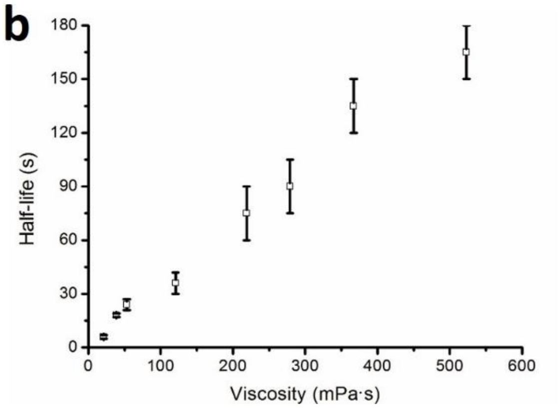

**Figure 2.5** (a) Viscosities of various polar solvents used in this experiment; (b) A plot of the half-life of reflectance decay versus the solvent viscosities.

The above nanorods dispersions can serve as promising bi-stable photonic inks, benefitting from the instant alignment of the nanochains in response to the application of external fields and their delayed rotational movements after field removal. In one demonstration, a unique bi-stable photonic writing tablet were fabricated by dispersing nanochains in 95% glycerol solution and sealing the solution inside a 75 mm × 50 mm × 1 mm glass vessel. A refrigerator magnet with stripe-patterned field distribution with a strength of 130 G (as illustrated in Figure 2.6a) was used to investigate the performance of the tablet.[21] Upon the application of a magnetic field, alternating green or brown stripes appeared within 1 s, owing to the strong magnetic interactions between nanochains and the magnet, as shown in Figure 2.6b. In the areas where the magnetic field was parallel to the viewing angle, green strips could be observed, while brown stripes appeared in areas where the direction of magnetic field was perpendicular. As shown in Figure 2.6c, the alternating strips remained visually almost unchanged 3 mins after the removal of the magnet, suggesting a good bi-stability of the photonic dispersion. Although gradual intensity decay occurred over time, the strips remained distinguishable after more than 10 mins. Patterns or letters can also be manually written on this writing tablet by using a small piece of magnet as a “pen”, as shown in Figure 2.6d.

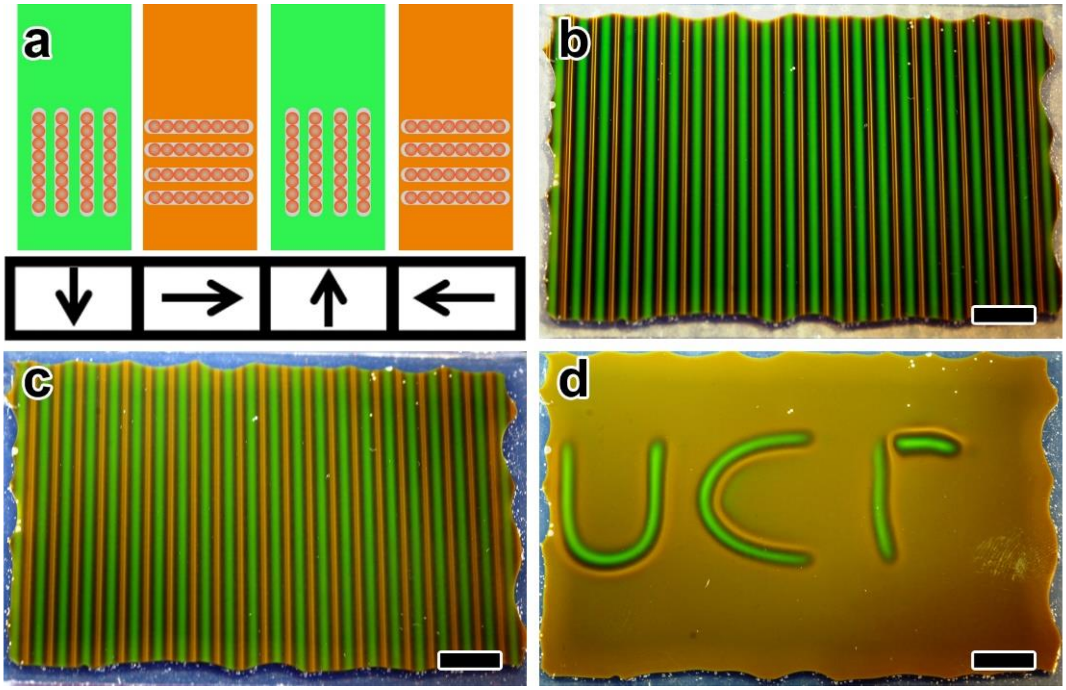

**Figure 2.6** (a) Scheme showing the field orientations of the stripe-patterned refrigerator magnet (black arrows) and the corresponding alignment of the nanochains in response to such a complex field; (b) Digital photo of the display right after removing the stripe-patterned magnet; (c) Digital image of the display in 3 mins after the removal of the magnet; (d) Letters written on the display manually by using a small magnetic "pen". Scale bar: 1 cm.

As the color of photonic inks is solely dependent on the field direction, information can be simply written on or erased from the inks by applying magnetic fields parallel or perpendicular to the viewing angle. A photonic ink based on "green" nanochains with a maximum reflection peak around 540 nm was chosen for investigation. Their optical images during the writing and erasing operations were presented in Figure 2.7a and 2.7b. The writing and erasing operations were repeated for 12 cycles, and corresponding reflectance of the photonic inks was measured and plotted, as shown in Figure 2.7c. Both the writing and erasing process can be finished within 1 s, owing to the fast response of the nanochains to external magnetic fields. The reflectance doesn't change obviously after twelve cycles, indicating an excellent reversibility of the photonic ink.

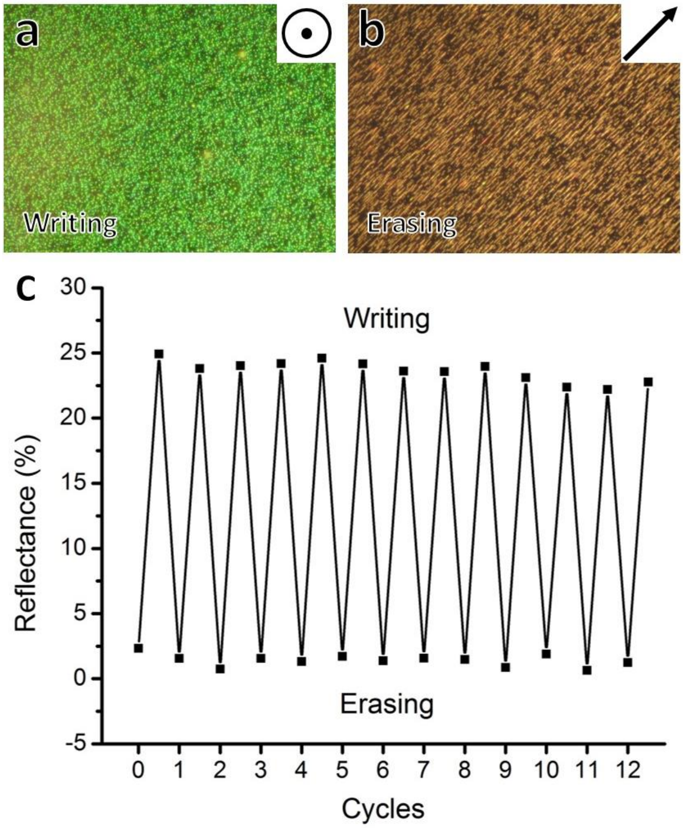

**Figure 2.7** (a, b) Dark-field optical microscopy images of inks after (a) writing and (b) erasing, with the top right insets indicating the field directions; (c) A Plot of the change in the reflectance intensity of photonic ink in 12 cycles of writing and erasing operations. The reflectance was measured at the wavelength of 540 nm, and 1 s after each operation.

In addition to the solvent viscosities, the lengths and the aspect ratios of nanochains also determine their rotational diffusivities, as described by the previous equation. To investigate the effect of the chain lengths, two types of nanochains, one with an average length of 10 μm, and another with an average length of 3.5 μm were fabricated. Their

Brownian rotations in a 95% glycerol solution were then monitored by an optical microscope operated in a dark-field mode. Figure 2.8a and 2.8b show the movement paths of these two nanochains in 1 min. The time interval between neighboring pictures is set to be 6 s. For the measured nanochains, no significant change in their lengths was observed; therefore in the later discussions, their movements were treated as two-dimensionally, within the focal plane.

The mean square displacements (MSDs) for the rotation of nanochains were evaluated and plotted against time, as shown in Figure 2.8c and 2.8d. After fitting the observed values, the rotational diffusivity of the 3.5 μm chain is found to be $8.8 \times 10^{-3}\ rad^2/s$, which is about 23 times higher than that of the 10 μm chain ($3.8 \times 10^{-4}\ rad^2/s$). This result fits the theoretical expectation which predicted that the rotational diffusivities of nanochains are nearly inversely proportional to the cube of their lengths. It is however worth noting that these data only describe the one-directional in-plane rotation of nanochains within 1 min, the diffusivities over a longer period might be lower than these values since the rotation may appear more random.

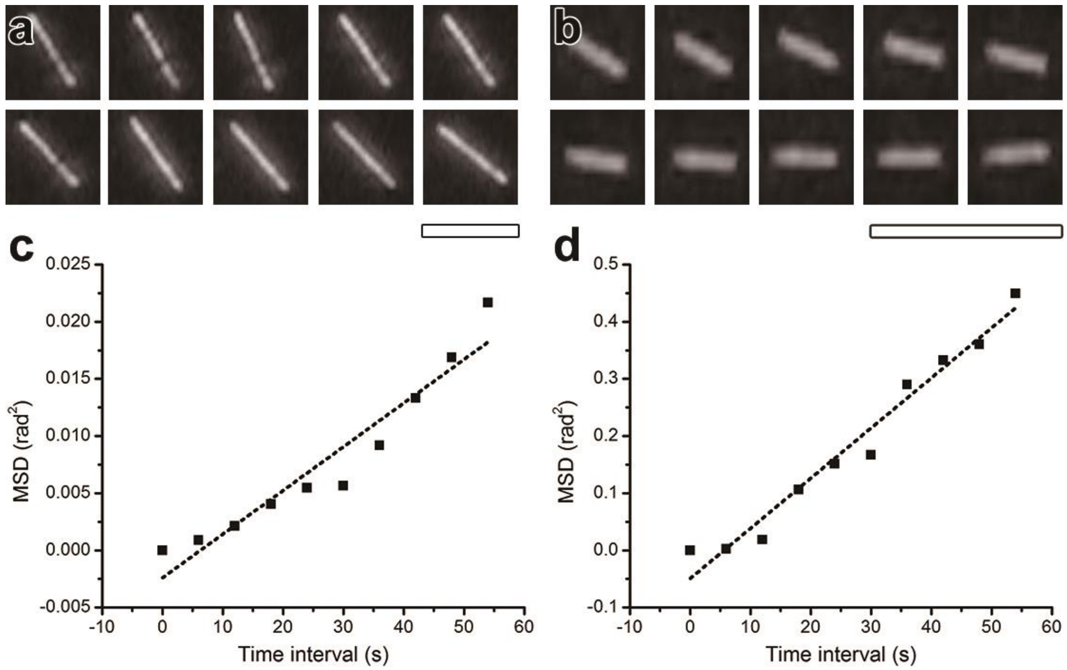

**Figure 2.8** (a, b) Dark-field optical microscope images showing the Brownian rotations of (a) a 10 μm nanochain and (b) a 3.5 μm nanochain in a 95% glycerol solution. From left to right, top to bottom, the time interval between two pictures is 6 s. Scale bars: 10 μm; (c, d) Plots of MSDs versus time for the rotations of (c) the 10 μm nanochain and (d) the 3.5 μm nanochain.

The different rotational diffusivities of nanochains of different lengths allows for the design of more complicated features, for example, a photonic ink display that can show two distinct colors when the external field is switched on and off. This concept was then successfully demonstrated by mixing two photonic nanochains with different diffraction colors and chain lengths. The shorter nanochains are much easier to undergo thermal fluctuations, and therefore lose their photonic properties relatively quicker after the removal of external magnetic fields, while the longer nanochains are able to maintain aligned and diffract the incident light for much longer time. In one demonstration, shorter blue nanochains and longer green nanochains were synthesized respectively, and mixed together in a 95% glycerol solution with a volumetric ratio of approximately 7:1. As shown in Figures 2.9a and 2.9b, upon the application of an external magnetic field, the blue nanochains dominate since their volume concentrations are higher; however, blue dots disappear quickly after the removal of the magnetic field while the green dots are able to maintain for a longer period. An interesting photonic ink display were then constructed by sealing this ink in a glass vessel. With the application of the same patterned magnetic field as previously used, the device shows a blue color due to the higher concentration of the blue nanochains. The original blue stripes fade out within only 2 s after the removal of the pattern magnet, leaving only green stripes which can stay for an additional 10 mins, as shown in Figure 2.9c and 2.9d. This unique display may find immediate uses in anti-counterfeiting or color signage applications.

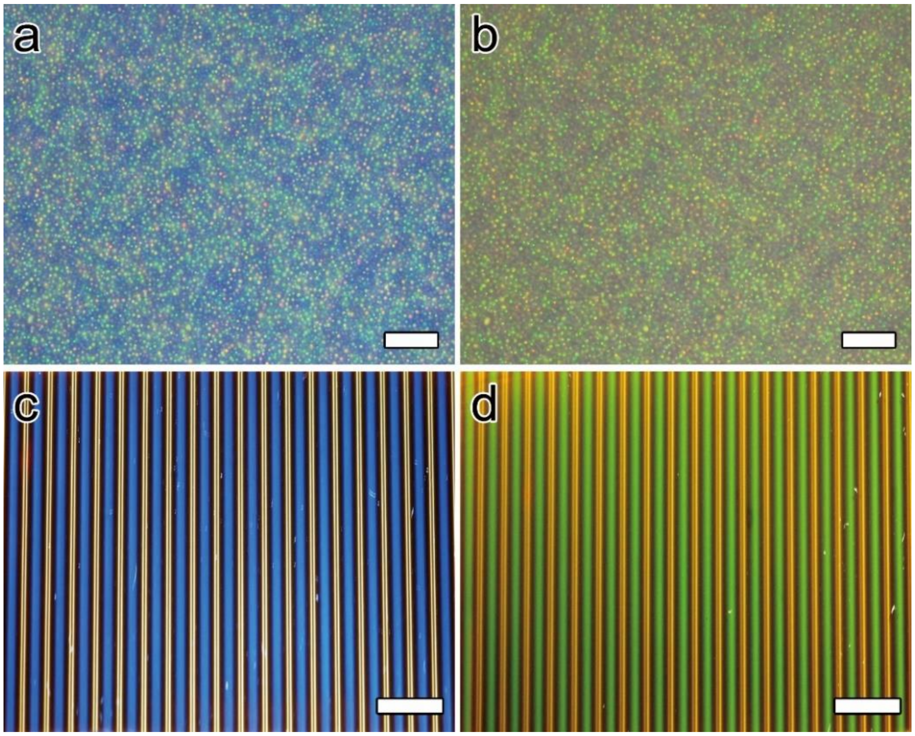

**Figure 2.9** (a) A dark-field optical microscopy image of an ink containing two types of photonic nanochains with different diffraction colors (blue and green) and chain lengths (~ 2 μm and ~ 10 μm) in response to an external magnetic field parallel to the viewing angle; (b) An image of the same ink in 30s after removing the magnetic field; (c) A digital photo of a display fabricated using this ink in the presence of a patterned magnet; (d) A digital photo of the same display in 30s after removing the patterned magnet. Scale bars are 10 μm in (a, b) and 1 cm in (c, d).

## 2.4 Conclusion

In summary, I have developed a new type of ink with fast response, good reversibility and temporary bi-stability by taking advantage of the viscosity dependent rotational diffusivity of the magnetic photonic nanochains. The photonic response of inks can be selectively turn on or off by tuning the direction of external magnetic fields. Temporary bi-stability can be enhanced by increasing the solvent viscosity and/or the length of nanochains. Inks based on 95% glycerol solution are able to retain their color for at least three minutes, which enables people to percept the information without energy supply. The electrode-less remote control, temporary bi-stability, excellent rewritability, reduced energy consumption, and the low toxicity of the materials promise many intriguing applications. For example, the delayed photonic decay might already be useful for creating unique security features for anticounterfeiting. More complex security encoding involving more sophisticated color expression can be achieved by mixing photonic nanochains of different lengths. For signage type applications, intermit refreshing of the patterns by pulsed magnetic field may allow retaining the color information for infinitely long period while at the same time significantly reduce the energy cost.

## 2.5 Reference

1. Ozin, G.A. and A.C. Arsenault, *P-Ink and Elast-Ink from lab to market*. Materials Today, 2008. **11**(7): p. 44-51.

2. Antia, M., *Switchable Reflections Make Electronic Ink*. Science, 1999. **285**(5428): p. 658.

3. Butler, D., *Electronic ink for current issues*. Nature, 2001. **411**(6833): p. 5-5.

4. Sobel, A., *Electronic paper: High-speed inks*. Nat Mater, 2003. **2**(10): p. 643-644.

5. Comiskey, B., et al., *An electrophoretic ink for all-printed reflective electronic displays*. Nature, 1998. **394**(6690): p. 253-255.

6. Ota, I., J. Ohnishi, and M. Yoshiyama, *Electrophoretic image display (EPID) panel*. Proceedings of the IEEE, 1973. **61**(7): p. 832-836.

7. Ge, J., Y. Hu, and Y. Yin, *Highly Tunable Superparamagnetic Colloidal Photonic Crystals*. Angewandte Chemie International Edition, 2007. **46**(39): p. 7428-7431.

8. Xu, X. and S.A. Asher, *Synthesis and Utilization of Monodisperse Hollow Polymeric Particles in Photonic Crystals*. Journal of the American Chemical Society, 2004. **126**(25): p. 7940-7945.

9. Ge, J., et al., *Assembly of Magnetically Tunable Photonic Crystals in Nonpolar Solvents*. Journal of the American Chemical Society, 2009. **131**(10): p. 3484-3486.

10. Ge, J. and Y. Yin, *Magnetically Tunable Colloidal Photonic Structures in Alkanol Solutions*. Advanced Materials, 2008. **20**(18): p. 3485-3491.

11. Gong, T., D.T. Wu, and D.W.M. Marr, *Electric Field-Reversible Three-Dimensional Colloidal Crystals*. Langmuir, 2003. **19**(15): p. 5967-5970.

12. Shim, T.S., et al., *Dynamic Modulation of Photonic Bandgaps in Crystalline Colloidal Arrays Under Electric Field*. Advanced Materials, 2011. **22**(40): p. 4494-4498.

13. Lee, I., et al., *Quasi-Amorphous Colloidal Structures for Electrically Tunable Full-Color Photonic Pixels with Angle-Independency*. Advanced Materials, 2011. **22**(44): p. 4973-4977.

14. Arsenault, A.C., et al., *A Polychromic, Fast Response Metallopolymer Gel Photonic Crystal with Solvent and Redox Tunability: A Step Towards Photonic Ink (P-Ink)*. Advanced Materials, 2003. **15**(6): p. 503-507.

15. Arsenault, A.C., et al., *Photonic-crystal full-colour displays*. Nat Photon, 2007. **1**(8): p. 468-472.

16. Ge, J., et al., *Rewritable Photonic Paper with Hygroscopic Salt Solution as Ink*. Advanced Materials, 2009. **21**(42): p. 4259-4264.

17. Fudouzi, H. and Y. Xia, *Photonic Papers and Inks: Color Writing with Colorless Materials*. Advanced Materials, 2003. **15**(11): p. 892-896.

18. Fudouzi, H. and Y. Xia, *Colloidal Crystals with Tunable Colors and Their Use as Photonic Papers*. Langmuir, 2003. **19**(23): p. 9653-9660.

19. Hu, Y., L. He, and Y. Yin, *Magnetically Responsive Photonic Nanochains*. Angewandte Chemie International Edition, 2011. **50**(16): p. 3747-3750.

20. Kirkwood, J.G. and R.J. Plock, *Non‐Newtonian Viscoelastic Properties of Rod‐Like Macromolecules in Solution* Journal of Chemical Physics, 1956. **24**: p. 665.

21. He, L., et al., *Assembly and Photonic Properties of Superparamagnetic Colloids in Complex Magnetic Fields*. Langmuir, 2011. **27**(22): p. 13444-13450.

# Chapter 3

# Magnetic Assembly and Tuning of Ellipsoidal-Nanoparticle-Based Colloidal Photonic Structures

## 3.1 Introduction

When the periodicity of and the dielectric contrast in the assemblies of dipolar particles match visible diffraction conditions, they may display iridescent structural colors. The diffraction wavelength (or band gap position) of the colloidal crystals can be described by Bragg's law, $m\lambda = 2nd\sin\theta$, where $m$ is the diffraction order, $\lambda$ is the wavelength of incident light, $n$ is the effective refractive index, $d$ is the lattice spacing, and $\theta$ is the glancing angle between the incident light and diffraction crystal plane. In order to magnetically tune the photonic property of colloidal crystals, the external magnetic field must be able to induce changes in either the refractive index of the components, or the symmetries, lattice parameters or orientations of the ordered arrays.

Monodisperse colloidal magnetic particles have long been regarded as one of the most suitable building blocks for magnetically responsive photonic structures, since their magnetic responses are much stronger than normal paramagnetic materials and their dipole-dipole interactions can be fully initiated and controlled by external magnetic fields. However, the self-assembly of colloidal particles into high-dimensional ordered structures usually requires a sufficiently high concentration, therefore the average excluded volume of each particle becomes smaller, allowing less space for effective tuning of the photonic property of the as-assembled structures. The use of anisotropic particles, however, is expected to bring up with more degrees of freedom in designing. In addition to the positional order that is usually considered for describing assemblies from spherical building blocks, one should take orientational order into account when anisotropic building blocks are assembled.[1]

Efforts along this direction, however, has been very limited, mostly due to the unavailability of high quality anisotropic building blocks and the lack of effective mechanism for assembly and tuning. In this chapter, I investigated the synthesis of well-defined ellipsoidal colloidal particles with anisotropy in both morphology and magnetic properties, and then demonstrated their assembly into 3D ordered structures with unique tunable photonic properties. Unlike conventional colloidal crystals made from spherical magnetic particles where dynamic tuning of photonic property can only be achieved by controlling the field strength,[2-4] the diffraction properties of the current systems are strongly dependent on the field direction, which affects the orientation of the ellipsoidal particles. A wide range of tuning in diffraction spectrum can therefore be achieved by controlling the direction of the external magnetic field, while the field strength has only minimal influence on the diffraction wavelength. These novel photonic structures displayed a unique U-shaped profile in reflectance peaks in response to the variations in field direction: they diffract at a minimum wavelength when the field direction is perpendicular to the incident angle, and a maximum wavelength when the field is switched to parallel direction; and the diffraction intensity reaches maximum values when the fields are either parallel or perpendicular to the incident light, and decreases when the field direction is switched off-angle. The shift in diffraction in response to the change in field direction is instantaneous and reversible. This work represents a unique demonstration of magnetically responsive photonic structures whose diffraction property can be widely tuned by controlling the field direction rather than the field strength.

## 3.2 Synthesis and Characterization

***Chemicals.*** Ethanol (denatured), Iron(III) chloride hexahydrate, hydrochloric acid (37 % solution in deionized water), ammonium hydroxide (28-30 % solution in deionized water) and tetraethyl orthosilicate (TEOS) were purchased from Fisher Scientific. Polyacrylic acid (PAA, MW = 1800), cetyltrimethylammonium bromide (CTAB) were obtained from Sigma-Aldrich. All chemicals were directly used as received without further treatment.

***Synthesis of FeOOH nanorods.*** The synthesis of FeOOH nanorods was based on a previous report with slight modifications. In a typical synthesis of smaller FeOOH nanorods, $FeCl_3 \cdot 6H_2O$ was dissolved in 40 mL of deionized water and the molarity of $Fe^{3+}$ was adjusted to 0.02 M. The undissolved precipitates were discarded after centrifugation at 11000 rpm for 3min. The supernatant was transferred to a three-neck flask and heated at 81 °C under magnetic stirring for 12 hrs. The particles were then isolated by centrifugation, washed with deionized water for several times, and dispersed in 7.2 mL of deionized water. In a typical synthesis of larger FeOOH nanorods, $FeCl_3 \cdot 6H_2O$ was dissolved in 40 mL of deionized water and the molarity of $Fe^{3+}$ was adjusted to 0.1 M. 1g of CTAB was added into the solution. The undissolved precipitates were discarded after centrifugation at 11000 rpm for 3min. The supernatant was transferred to a three-neck flask and heated at 90 °C under magnetic stirring for 18 hrs. The particles were then isolated by centrifugation, washed with deionized water for several times, and dispersed in 36 mL of deionized water.

***PAA functionalization of FeOOH nanorods.*** A PAA stock solution was first prepared by dissolving 0.072 g of PAA in 10 mL of deionized water. Typically, 3 mL of the above FeOOH dispersions and 1 mL of PAA stock solution was added into 16 mL of deionized water under sonication. The mixture was then stirred for 12 hrs to allow the complete functionalization of nanorods. Afterwards, the excess PAA in the solution was removed by centrifugation, and the FeOOH nanorods were redispersed in 3 mL of deionized water.

***Synthesis of FeOOH@$SiO_2$ nanoellipsoids.*** The above aqueous dispersion of PAA-functionalized FeOOH was added into 20 mL of isopropanol, followed by the addition of 1 mL of ammonium hydroxide. For the silica coating of smaller FeOOH nanorods, 400 μL of tetraethyl orthosilicate (TEOS) was added into the above mixture in every 30 mins until the total amount of TEOS reached 2.4 mL. For the silica coating of larger FeOOH nanorods, 200 μL of TEOS was added into the above mixture in every 30 mins until the total amount of TEOS reached 1.2 mL. After an additional 1 hr of reaction, the silica-coated elliptical nanoparticles were isolated by centrifugation, washed with ethanol and deionized water for several times, and dispersed in 1 mL of ethanol.

***Reduction of FeOOH@$SiO_2$ nanoellipsoids.*** An ethanolic dispersion FeOOH@$SiO_2$ nanoellipsoids was transferred to a combustion boat, which was placed in a tube furnace (MTI Corporation OTF-1200X), and heated to 500 °C under $N_2$ protection, and then reduced at this temperature for 2 hrs by pure $H_2$ to produce the magnetic nanoellipsoids.

The as-reduced nanoellipsoids were kept in pure $H_2$ atmosphere until the temperature drop to room temperature.

***Assembly of nanoellipsoids into photonic structures.*** The as-reduced magnetic nanoellipsoids were dispersed in deionized water by sonication for 30 min. The dispersion was then transferred to a 100 mL three-neck flask and boiled at 100 °C for 2 hrs with refluxing. The nanoellipsoids were isolated by centrifugation and washed by deionized water for several times. Size selection was then applied and non-dispersible aggregates were discarded by centrifugation at 2000 rpm for 2 min. The dispersions of nanoellipsoids were first concentrated to the maximum volume fraction beyond which aggregations would form, and a certain amount of deionized water was then added into the dispersions to reach the desired concentration. The concentrated dispersions of nanoellipsoids displayed photonic colors, from blue to red, suggesting the formation of photonic structures.

***Characterization.*** The morphology of the initial FeOOH nanorods and Fe@$SiO_2$ nanoellipsoids was characterized using a Tecnai T12 transmission electron microscope. The UV-vis spectra were measured using a probe type Ocean Optics HR2000CG-UV-vis spectrometer in reflection mode with an integration time of 150 ms. The magnetic fields applied to samples during the measurement were generated by an 1" cubic neodymium magnet. The strength and the direction of magnetic fields can be tuned by manually controlling the distance between the magnet and the sample and rotating the magnet. Zeta potential measurement of the nanoellipsoids dispersion was performed by using a Beckman Coulter Delsa Nano C Zeta Potential Analyzer. For achieving the rainbow photonic pattern, the nanoellipsoids dispersion with a volume fraction of 27% was encapsulated in a flat glass capillary tubes, and placed on the top of a refrigerator magnet (nonideal linear Halbach array) purchased from McMaster-Carr.

### 3.3 Results and Discussion

Representative TEM images of the starting nanorods and the final product elliptical nanoparticles were shown in Figure 3.1. The nanorods in Figure 3.1a have an average length of 70 nm and width of 10 nm; while the nanorods in Figure 3.1b are a bit larger, with an average length of 110 nm and width of 20 nm. Both nanorods exhibit a well-defined rod-like morphology. The elliptical nanoparticles synthesized from the smaller nanorods had an average length of 190 nm and an average diameter of 130 nm; while the nanoellipsoids synthesized from the larger nanorods had an average length of 220 nm and an average diameter of 130 nm. Both nanoparticles exhibit a well-defined elliptical morphology, and their size distributions are very uniform, according to the TEM images in Figure 3.1c and 3.1d. For simplicity in discussion, the smaller nanorods are named as “nanorods A”, and the larger nanorods are named as “nanorods B”. Accordingly, the elliptical nanoparticles synthesized from nanorods A are named as “nanoellipsoids A”, and the elliptical nanoparticles synthesized from nanorods B are named as “nanoellipsoids B”.

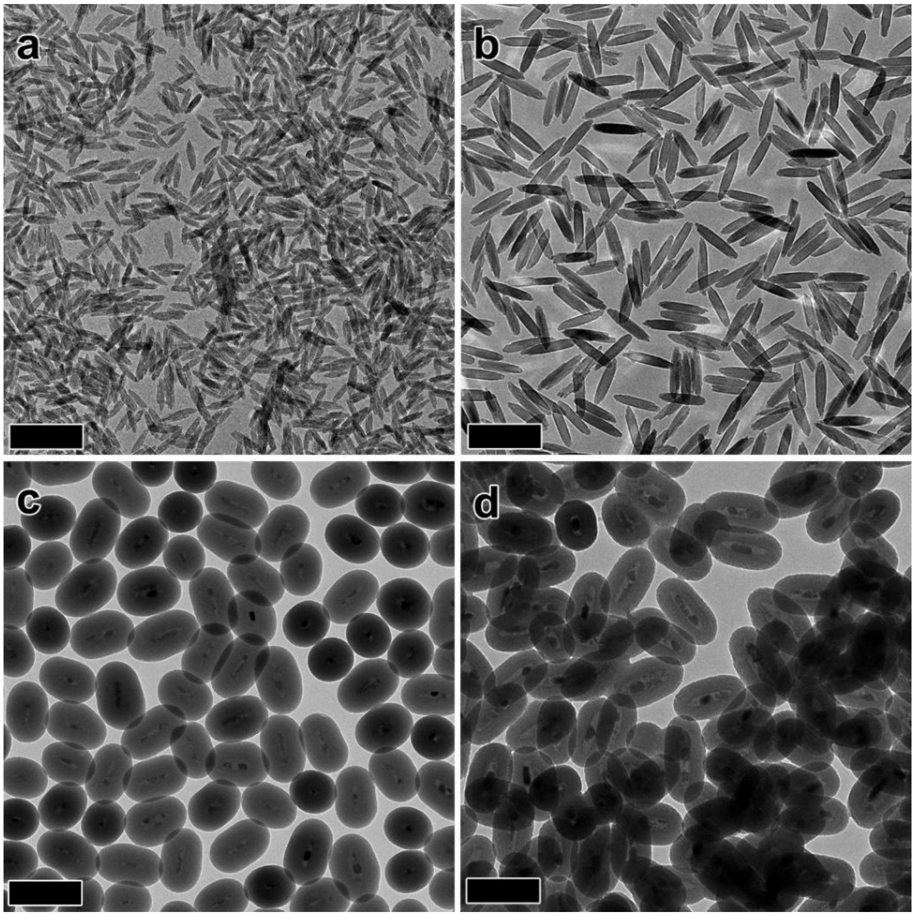

**Figure 3.1** TEM images of (a) Nanorods A; (b) Nanorods B; (c) Nanoellipsoids A; (d) Nanoellipsoids B. Scale bar: 200 nm.

XRD patterns in Figure 3.2a clearly show that the nanorods A and B are both pure β-FeOOH (akaganeite), with the strongest diffraction peak at around 35°. Due to the high reducing ability of hydrogen, these FeOOH nanorods are reduced to pure iron under the above experimental condition, XRD patterns of nanoellipsoids A and B only show the characteristic peak of iron (110) and (200) facets, as shown in Figure 3.2b. No other peak can be observed, except for an absorption shoulder at around 25° which can be attributed to amorphous silica. The XRD peaks of FeOOH nanorods are relatively weak, owing to the thick silica coating and the relatively small size of iron nanoparticles embedded inside the nanoellipsoids. Magnetic property characterizations of nanoellipsoids A and B (Figure 3.2c and 3.2d) indicated that both nanoellipsoids are ferromagnetic. Nanoellipsoids A have a saturated magnetization of 0.6 emu/g and a coercivity of 500 G, while nanoellipsoids B have a saturated magnetization of 1.2 emu/g and a coercivity of 800 G. Although the coercivities of nanoellipsoids are relatively large, their inter-particle magnetic interactions are relatively weak, owing to their extremely low saturated magnetizations. The magnitude of magnetic interactions between particles are determined by the magnetic moments of particles, which relates to the saturated magnetizations of particles.

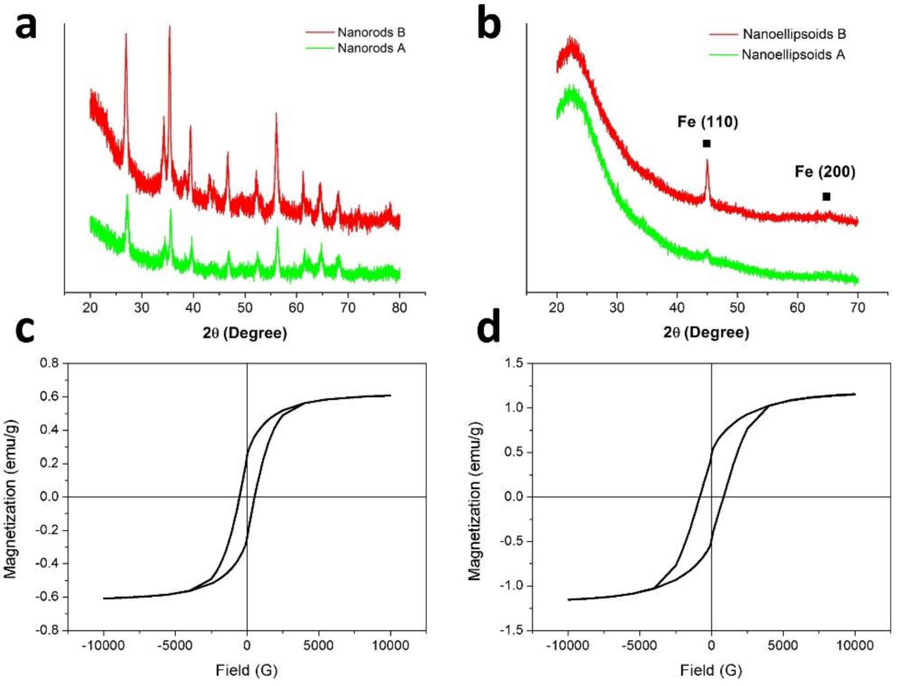

**Figure 3.2** (a) XRD patterns of nanorods A and B; (b) XRD patterns of nanoellipsoids A and B; (c) Magnetic hysteresis loop of nanoellipsoids A; (d) Magnetic hysteresis loop of nanoellipsoids B.

The key for the successful assembly of nanoellipsoids into ordered photonic structures is the presence of charges on their surfaces which provide long-range strong electrorepulsive forces. Owing to the high temperature treatment, the as-reduced nanoparticles barely have any change on their surfaces. In order to enhance the charges on the nanoparticles surfaces, I refluxed the nanoparticles in water for a certain period of time. Hot water acts as an etchant to slightly etch the dense silica surface, to create more silanol groups on the surfaces and thus to allow nanoparticles assemble into ordered structures without aggregations.[5] By using the nanoellipsoids A as an example, I demonstrated the effect of refluxing time on the surface charge of nanoparticles and the diffraction intensity of photonic structures assembled from them. A magnetic field (~ 50 mT) was applied perpendicular to the direction of incident light during the measurement. The ζ-potential of as-reduced nanoparticles was -31 mV, as indicated in Figure 3.3. After being concentrated, they were not able to form photonic structures since their relatively low charged surfaces were not sufficient for stabilizing them and therefore no reflectance can be measured. Refluxing nanoellipsoids in water significantly enhance the surface charges as well as their photonic performance. After being refluxed for 2 hrs, their ζ-potential dropped to -57 mV, comparable to the polyacrylate-capped $Fe_3O_4$ particles (-49 mV) and refluxed $Fe_3O_4$@$SiO_2$ (-56.5 mV),[6, 7] and are thus excellent building blocks for constructing photonic structures. Elongating the refluxing time to 150 min led to almost same results, so I set the refluxing time to 2 hrs and used the resultant nanoellipsoids for all the following experiments.

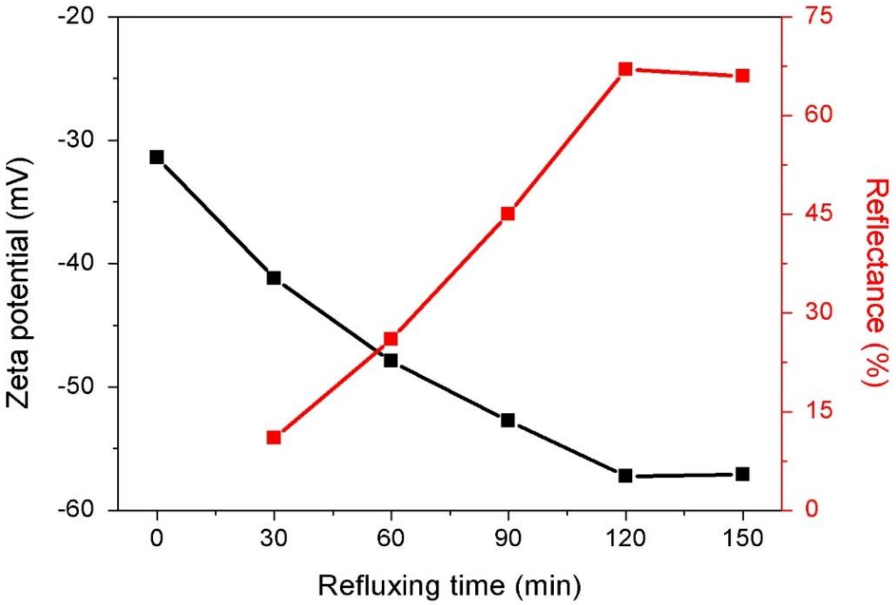

**Figure 3.3** Dependence of zeta potentials of nanoellipsoids A and reflectance of the resultant photonic structures assembled from nanoellipsoids A under a perpendicular magnetic field on the refluxing times.

For the description of the ordered structures assembled from spherical nanoparticles, people usually use positional orders; however, when it comes to the nanoellipsoids, we have to also take orientational orders into account.[7] The orientation of nanoellipsoids can be conveniently tuned by an external magnetic field, owing to the anisotropic magnetic cores embedded inside them. Upon the application of magnetic fields, nanoellipsoids rotate and align their long axis parallel to the field direction. Such rotation immediately results in changes in the orientational orders. In addition, as the direction of incident light is fixed, the rotation of nanoellipsoids also gives rise to changes in the periodicity of the photonic structures. As schematized in Figure 3.4, in the left situation, the periodicity of photonic structures is based on the long axis of nanoellpisoids, and is thus the largest. As a result, the diffraction wavelength of the photonic structures reaches the maximum. In the middle situation, the periodicity of photonic structures is based on the short axis of nanoellpisoids and is the smallest, therefore the diffraction wavelength of the photonic structures reaches the minimum. In the right situation, the periodicity of photonic structures is right in between the previous two scenarios, and the diffraction wavelength of the photonic structures also falls in between them.

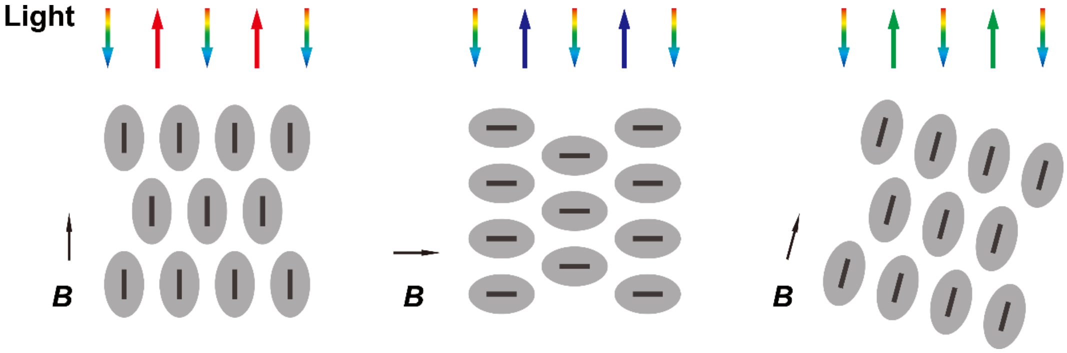

**Figure 3.4** Scheme showing the tuning of periodicity and diffraction wavelength of the photonic structures assembled from nanoellipsoids by external magnetic fields.

To allow the formation of photonic structures, the aqueous dispersions of nanoellipsoids were concentrated to a volume fraction of 18%. The optical property of resultant photonic structures were then investigated under magnetic fields (~ 50 mT) with varying directions. As shown in Figure 3.5a and 3.5b, the diffraction wavelengths reached the minimum when the field direction was perpendicular to the incident light, and gradually red shifted as the field direction rotated from perpendicular to parallel to the incident light. Such shift in reflection wavelengths responds to the change of field direction immediately (within less than a second) and is fully reversible. A notable feature of such magnetic tuning is that the maximum intensity is achieved at the two end points when the magnetic fields are either parallel or perpendicular to the incident light. When the field direction is switched away from these two end points, the relative intensity decreases and reaches a minimum at the middle point (~ 45° from the parallel and perpendicular directions), resulting in an overall U-shaped profile of reflectance peaks. This is a major difference when compared to the previous reported 1D photonic chains where the strongest reflectance is only achievable under intermediate field intensity and the profile of reflectance peaks is an inverted U curve. The minimum diffraction wavelengths of photonic structures assembled from nanoellipsoids A and B were found to be 530 nm and 513 nm, respectively; while the maximum diffraction wavelengths were 643 nm and 725 nm, respectively. Compared to nanoellipsoids A, photonic structures assembled from nanoellipsoids B exhibited a broader tuning range of about 212 nm. The relatively larger aspect ratio of nanoellipsoids B lead to more changes in the inter-planar spacing when the orientation of the assembled crystals are switched, resulting in a broader tuning range in photonic response.

The orientational dependence of the nanoellipsoidal assemblies can find direct use in creating photonic patterns under magnetic fields with non-uniform field directions. As demonstrated in Figure 3.5c and 3.5d, when subjected to complex magnetic field produced by a non-ideal linear Halbach array which has a spatially rotating pattern of magnetization, a dispersion of nanoellipsoids A (with a volume fraction of 32%) encapsulated in a flat glass tube exhibits an alternating pattern containing blue and green stripes. The green strips are at the areas where the magnetic fields are parallel to the viewing angle; while the blue strips are the areas where the magnetic fields are perpendicular to the viewing angle. More interestingly, when a dispersion of nanoellipsoids B (with a volume fraction of 27%) was used, I was able to observe alternating red, green and blue strips, which almost covered the entire visible spectrum. The red strips were at the areas where the magnetic fields were parallel to the viewing angle; while the blue strips were the areas where the magnetic fields were perpendicular to the viewing angle. The green strips were located between red and blue strips, corresponding to the areas where the magnetic fields were tilted between parallel and perpendicular. It is noteworthy that similar transition strips were also present in Figure 3.5c; however, they can hardly be distinguished due to their relatively low contrast to the main blue and green strips. Unlike our previously demonstrated 1D photonic assembly which only shows single color stripes at areas with field parallel to the incident angle,[2] the current system displays stripes of various colors at areas with parallel and horizontal fields.

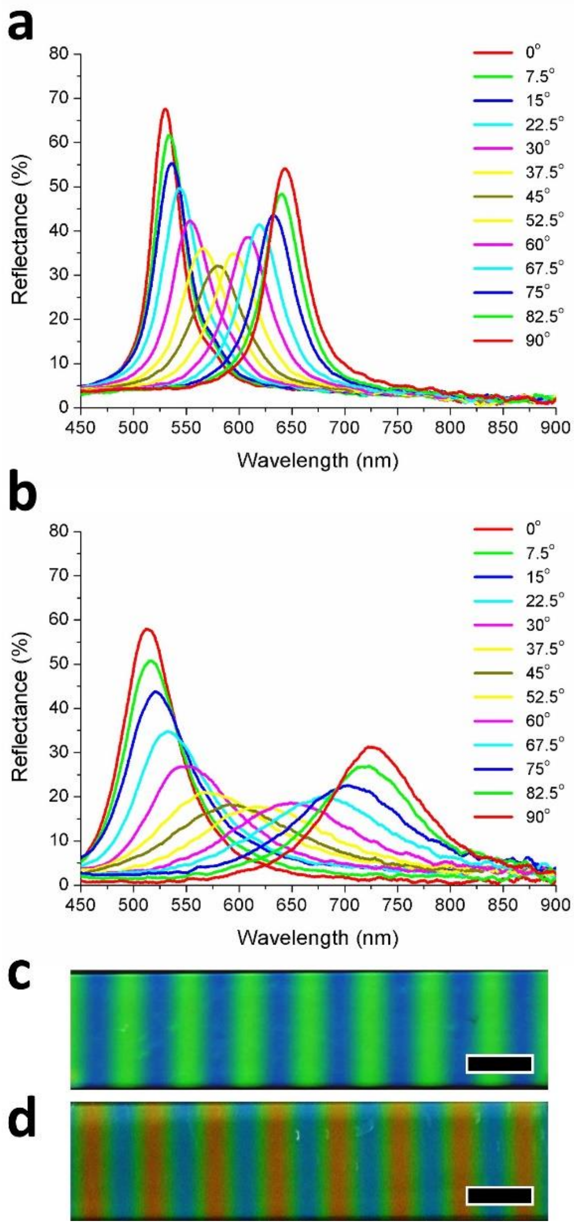

**Figure 3.5** (a) Reflection spectra of photonic structures assembled from nanoellipsoids A under magnetic fields with varying field directions; (b) Reflection spectra of photonic structures assembled from nanoellipsoids B under magnetic fields with varying field directions; (c) A Digital image of a capillary tube with photonic structures assembled from nanoellipsoids A on a piece of refrigerator magnet; (d) A Digital image of a capillary tube with photonic structures assembled from nanoellipsoids B on the same piece of refrigerator magnet. Scale bars for (c) and (d): 1 mm.

The field strength also play an important role since it determines to which degree the nanoellipsoids can be aligned by external magnetic fields. Figure 3.6a and 3.6b showed the reflection spectra of photonic structures assembled from nanoellipsoids A and nanoellipsoids B, under external magnetic fields with fixed directions (either parallel or perpendicular to the direction of incident light) but varying strengths. Two sets of reflection spectra can be found in each figure. When the field direction is perpendicular to the light, nanoellipsoids align themselves perpendicular to the light as well; the periodicity is determined by the shorter axis of nanoellipsoids and results in a reflection peak at shorter wavelengths. When the field direction is parallel to the light, the periodicity is determined by the longer axis of nanoellipsoids and accounts for in a reflection peak at longer wavelengths. The field strength is found to influence the reflectance rather than reflection wavelengths, for both nanoellipsoids A and nanoellipsoids B. The increased reflectance is believed to result from the better orientational order of nanoellipsoids. Because of the limited amount of magnetic species embedded inside them, the rotations of nanoellipsoids require a sufficient high magnetic field to allow the magnetic torque to overcome the rotational resistance. Meanwhile, the reflection wavelengths remain the same as the field strength increases, which indicates that the positional order of photonic structures is determined solely by electrostatic interactions. It also suggested that the magnetic interactions between nanoellisoids are negligible, owing to the limited amount of magnetic species inside them, and this fact is in accordance to our previous findings that the saturated magnetizations of nanoellipsoids are extremely low.

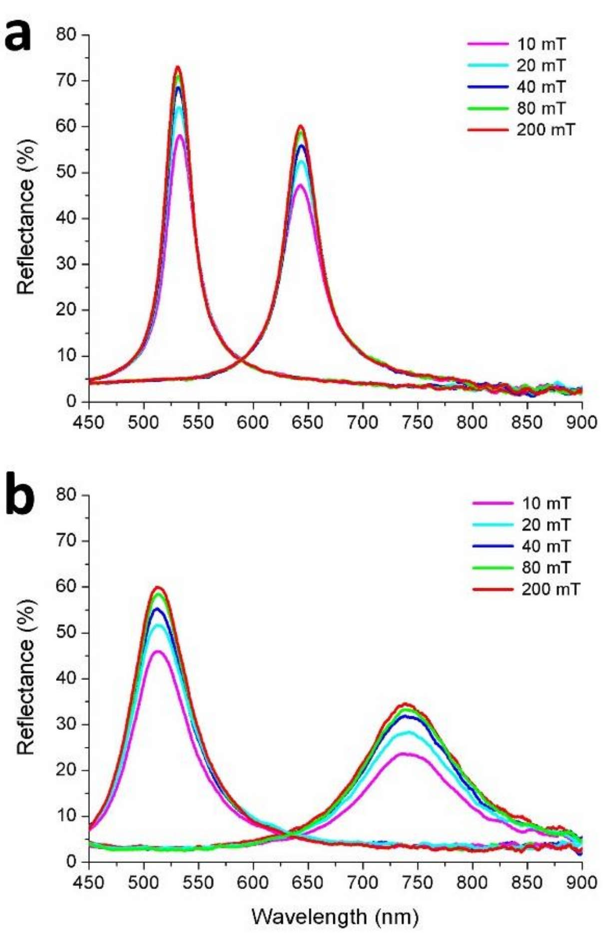

**Figure 3.6** (a) Reflection spectra of photonic structures assembled from nanoellipsoids A under magnetic fields with varying field strengths; (b) Reflection spectra of photonic structures assembled from nanoellipsoids B under magnetic fields with varying field strengths.

In addition to orientation, the inter-planar spacing of the photonic structures is also determined by the volume fractions of the nanoellipsoids.[8] As the volume fraction decreases, the average distances between nanoellipsoids increase, resulting in an expansion of crystal lattice as well as a red-shift of reflection wavelength. In the absence of magnetic fields, the reflection spectra of photonic assemblies formed by nanoellipsoids A under different volume fractions were recorded and exhibited in Figure 3.7a. The reflection peak shifted from 425 nm to 660 nm, as the volume fractions decreased from 32% to 10%. Consistently, a rainbow-like color effect was observed in Figure 3.7b in the dispersion of nanoellipsoids A with a volume fraction gradient, which was achieved by centrifugation at 3000 rpm for 5 min.

The synergy of both field directions and volume fractions allows for a wide range of tuning of the optical property of photonic assemblies. Figure 3.7c plotted the changes in peak positions with volume fraction of the dispersion for nanoellipsoids A. The blue dots and green dots refer to the reflection wavelengths measured under magnetic fields parallel and perpendicular to the incident light, respectively; while the red dots correspond to the reflection wavelengths measured in the absence of a magnetic field. Interestingly, for each volume fraction, the differences in the peak position of the photonic assemblies under parallel and perpendicular magnetic fields remain constantly at around 105 nm, as represented by the black dashed line. Such difference in peak positions is attributed to the difference in the long axis and the short axis of nanoellipsoids, and therefore is not subjected to any change in the volume fractions. In the absence of magnetic fields, the orientation of nanoellipsoids is less uniform. The inter-planar spacing of the assembled photonic structures and the wavelengths of reflection peaks are always between those under parallel magnetic fields and under perpendicular magnetic fields. The nanoellipsoids prefer to align themselves along the surface of sample container, which is perpendicular to the incident angle so that the reflection peak is closer to that of the case in a perpendicular magnetic field even at a relatively low volume fraction (Figure 3.7c). As the volume fraction increases, the orientational order of nanoellipsoids in the absence of magnetic fields enhances and eventually becomes nearly the same as the case aligned by magnetic field, as confirmed by the coincidence of the peak positions at a high volume fraction of 32%. The enhanced orientational order can be explained by the reduced excluded volume of each nanoellipsoid under a higher volume fraction. The nanoellipsoids decreased their orientational entropy but increased translational entropy to reach a more energetically favorable structure, in which most of nanoellipsoids align parallel.[9-14]

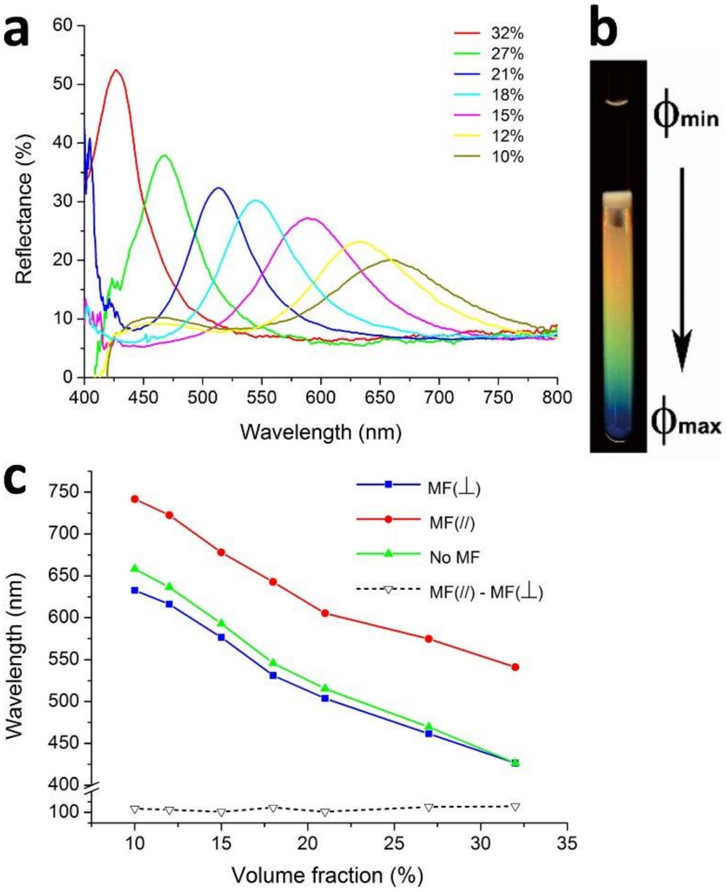

**Figure 3.7** (a) Reflection spectra of the colloidal dispersion of nanoellipsoids A under different volume fractions in the absence of magnetic fields; (b) A digital image of a dispersion of nanoellipsoids A in a glass capillary tube with a volume fraction gradient; (c) Dependence of reflection wavelengths of photonic structures on the volume fractions of nanoellipsoids A, in the presence and the absence of external magnetic fields.

Theoretical investigations have predicted that anisotropic nanoparticles would preferentially form a stretched face-centered cubic (*fcc*) structure as the volume fraction reaches a critical threshold.[15-17] Stretching an *fcc* lattice along different axes altered its symmetry, and resulted in new crystal lattices. As illustrated in Figure 3.8a, when the original *fcc* lattice is stretched along <100>, <110>, or <111> axes, it transforms into body-centered tetragonal lattice (*bct*), body-centered orthorhombic lattice (*bco*), or face-centered orthorhombic lattice (*fco*), respectively.

I estimated the crystal structures of the nanoellipsoidal assemblies under magnetic fields, based on their diffraction properties. The periodicities of photonic assemblies along different axes were calculated using diffraction wavelengths through Bragg's law; and were then plugged in the above three lattices to find out the lattice constants. As shown in Figure 3.8b, the *fco* lattice has the closest value to the experimental volume fractions compared to the *bct* and *bco* lattices. More importantly, in the *fco* lattice, the distances between one particular ellipsoid and its twelve nearest neighbors are almost identical; while in the *bct* or *bco* lattices, the distances between one particular ellipsoid and its twelve nearest neighbors are not identical, and the variations in them can be more than 30 nm or 60 nm, respectively, as calculated and plotted in Figure 3.8c. As the assembly of nanoellipsoids is driven solely by electrostatic forces, the surface to surface distances between one particular nanoellipsoid to its neighbors are not expected to vary significantly. Therefore in our system, nanoellipsoids were most likely to assemble into an *fco* lattice, in accordance to previous theoretical predictions that the *fco* lattice is most energetically favorable among the above three structures.[18]

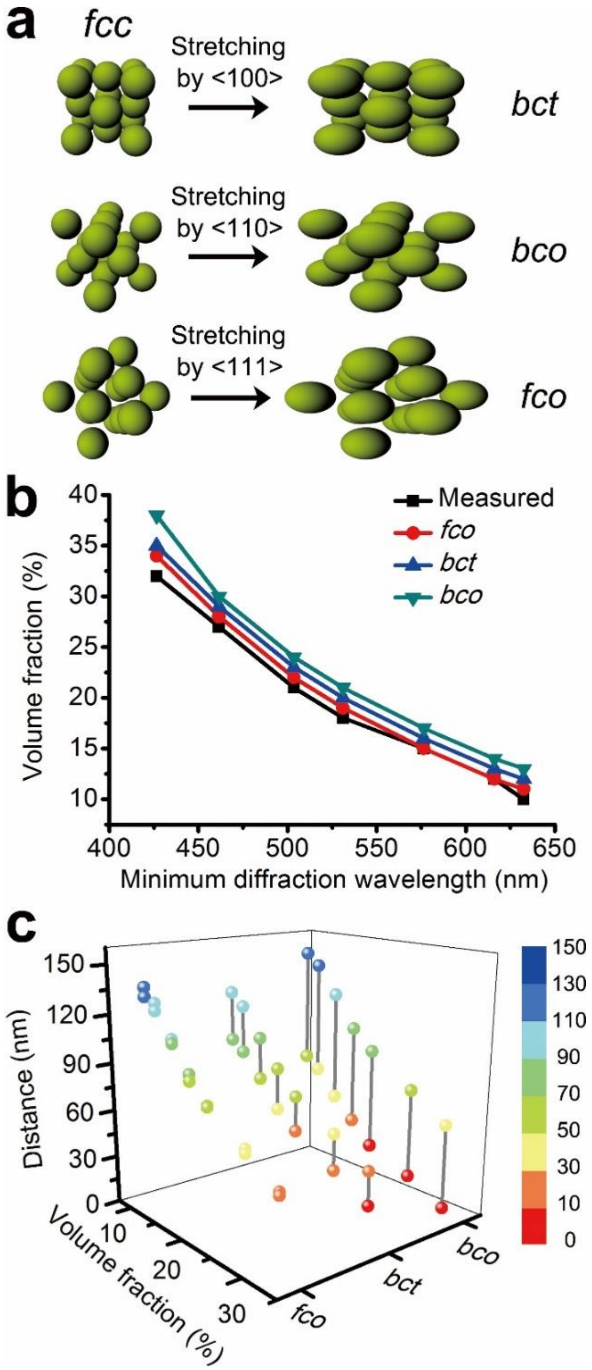

**Figure 3.8** (a) Possible structures resulting from the assembly of nanoellipsoids; (b) Comparison of the measured volume fractions to the calculated values for nanoellipsoids A; (c) Calculated surface-to-surface distances between one particular nanoellipsoid to its nearest neighbors in the three possible structures.

## 3.4 Conclusion

In summary, I synthesized shape- and magnetically anisotropic nanoellipsoids and demonstrated their assembly into photonic structures. It is found that changing the directions of magnetic fields significantly changes the diffraction wavelengths of the photonic structures, while altering the strength of magnetic fields only slightly influences their reflectance. Moreover, based on the photonic property of the as-assembled structures along different directions under a magnetic field, I investigated the assembly manner of nanoellipsoids and calculated the surface-to-surface distances between nanoellipsoids at different volume fractions. Our strategy can be extended to the self-assembly of other anisotropic nanoparticles and the dynamic tuning of their optical property by magnetic fields. These tunable anisotropic photonic structures not only enhance our understanding of self-assembly of anisotropic nanoparticles but also provide a new platform for building novel active optical components, color presentation and display devices.

## 3.5 Reference

1. Lu, Y., Y. Yin, and Y. Xia, *Three-dimensional photonic crystals with non-spherical colloids as building blocks*. Advanced Materials, 2001. **13**(6): p. 415-420.
2. He, L., et al., *Assembly and Photonic Properties of Superparamagnetic Colloids in Complex Magnetic Fields*. Langmuir, 2011. **27**(22): p. 13444-13450.
3. Hu, Y., L. He, and Y. Yin, *Charge Stabilization of Superparamagnetic Colloids for High-Performance Responsive Photonic Structures*. Small, 2012. **8**(24): p. 3795-3799.
4. Ge, J., Y. Hu, and Y. Yin, *Highly tunable superparamagnetic colloidal photonic crystals*. Angewandte Chemie-International Edition, 2007. **46**(39): p. 7428-7431.

5. Piao, Y., et al., *Wrap-bake-peel process for nanostructural transformation from beta-FeOOH nanorods to biocompatible iron oxide nanocapsules*. Nature Materials, 2008. **7**(3): p. 242-247.

6. Wang, M.S., et al., *Magnetic Tuning of Plasmonic Excitation of Gold Nanorods*. Journal of the American Chemical Society, 2013. **135**(41): p. 15302-15305.

7. Hu, Y.X., L. He, and Y.D. Yin, *Charge Stabilization of Superparamagnetic Colloids for High-Performance Responsive Photonic Structures*. Small, 2012. **8**(24): p. 3795-3799.

8. Gao, C., et al., *Highly Stable Silver Nanoplates for Surface Plasmon Resonance Biosensing*. Angewandte Chemie-International Edition, 2012. **51**(23): p. 5629-5633.

9. Frenkel, D., *Order through entropy*. Nature Materials, 2015. **14**(1): p. 9-12.

10. Taylor, M.P. and J. Herzfeld, *Shape Anisotropy and Ordered Phases in Reversibly Assembling Lyotropic Systems*. Physical Review A, 1991. **43**(4): p. 1892-1905.

11. Nguyen, K.T., F. Sciortino, and C. De Michele, *Self-Assembly-Driven Nematization*. Langmuir, 2014. **30**(16): p. 4814-4819.

12. Wang, M., et al., *Magnetically Actuated Liquid Crystals*. Nano Letters, 2014. **14**(7): p. 3966-3971.

13. Shah, A.A., et al., *Direct Current Electric Field Assembly of Colloidal Crystals Displaying Reversible Structural Color*. Acs Nano, 2014. **8**(8): p. 8095-8103.

14. Shah, A.A., et al., *Liquid Crystal Order in Colloidal Suspensions of Spheroidal Particles by Direct Current Electric Field Assembly*. Small, 2012. **8**(10): p. 1551-1562.

15. Hynninen, A.P. and M. Dijkstra, *Phase diagram of dipolar hard and soft spheres: Manipulation of colloidal crystal structures by an external field*. Physical Review Letters, 2005. **94**(13).

16. Evans, B., *The hard ellipsoid-of-revolution fluid. I. Monte Carlo simulations - Comment*. Molecular Physics, 2002. **100**(1): p. 199-200.

17. Frenkel, D. and B.M. Mulder, *The hard ellipsoid-of-revolution fluid. I. Monte Carlo simulations - Comment*. Molecular Physics, 2002. **100**(1): p. 201-217.

18. Solomon, M.J., *Directions for targeted self-assembly of anisotropic colloids from statistical thermodynamics*. Current Opinion in Colloid & Interface Science, 2011. **16**(2): p. 158-167.

# Chapter 4

# Magnetically Actuated Liquid Crystals

## 4.1 Introduction

Liquid crystals are state of matter intermediate between that of a crystalline and an isotropic liquid.[1-4] They possess many of the mechanical properties of liquid, e.g., high fluidity, formation, and coalescence of droplets. At the same time they are similar to crystals in that they exhibit anisotropy in their optical,[5-7] mechanical,[8] electrical,[9-11] and magnetic properties.[12-14] Examples of liquid crystals can be found both in the natural world and in technological applications. Most of electronic displays use liquid crystals.[15-17] Liquid-crystalline phases are abundant in living systems.[18] For example, many proteins and cell membranes are liquid crystals. Other well-known examples of liquid crystals are solutions of soap and various related detergents,[19] as well as the tobacco mosaic virus.[20]

The characteristic feature of liquid crystals is the presence of long-range orientational order in the arrangement of constituent molecules, and sometimes 1D or 2D quasi long-range translational or positional order.[21-23] The quintessential property of a liquid crystal is its anisotropy. The optical, mechanical, electrical and magnetic properties of liquid crystal medium are defined by the orientation order of the constituent anisotropic molecules. Due to the anisotropy of the electrical and magnetic properties, the orientation of the liquid crystal molecules is effectively controlled by electric or magnetic fields. As a result, by changing the liquid crystal molecules orientation, it is possible to change optical, mechanical properties of the medium. All of these are important to the functioning of devices based on liquid crystals: digital watches, calculators, flat TV-displays, thermometers and liquid crystal displays are all examples of what liquid crystal technology can achieve.

Liquid crystal phases can be divided into two classes: thermotropic liquid crystal phases and lyotropic liquid crystal phases. Thermotropic liquid crystal phases are formed by organic molecules in a certain temperature range.[24] Thermotropic organic molecules do not need solvent to form liquid crystal phase. In contrast, lyotropic liquid crystal phases form a solution, and the concentration controls the liquid crystallinity in addition to temperature.[25-27] Nowadays there are a plenty of ways to generate a liquid crystal phase. The thermotropic liquid crystals are usually formed by molecules with anisotropic shape, either elongated or disk-like. The lyotropic liquid crystals generally are two-component systems where building blocks are dissolved in a solvent. The building blocks forming lyotropic liquid crystals can be various, from amphiphilic organic molecules[28-30] to inorganic anisotropic nanostructures.[31-36]

Anisotropic colloidal inorganic particles, such as rods and platelets, have the ability to spontaneously self-organize into various liquid crystalline phases when brought in suspensions.[37-40] In the 1940s, Onsager explained in his seminal work the isotropic (I) to nematic (N) phase transition for rod-like particles on basis of the particle shape alone: at sufficiently high concentration the loss in orientational entropy is smaller than the gain in excluded volume entropy.[41] In the nematic state, the excluded volume decreases, and this gives rise to the translational entropy of the system

$$\Delta S_{tr} = -k_B \ln(1 - V_{excl}/V) \sim k_B \rho L^2 D$$

where $\rho = N/V$ is the density of rods with length $L$ and diameter $D$. However, there is also a decrease in orientational entropy in the nematic state, $S_N = k_B \ln \Omega_N$, in comparison to the isotropic state, $S_I = k_B \ln \Omega_I$,

$$\Delta S_{or} = k_B \ln \Omega_N/\Omega_I \sim k_B$$

where $\Omega_{I,N}$ gives the number of orientational states in the isotropic or nematic mesophase. At the nematic-isotropic transition, these two contributions compensate each other, $\Delta S_{or} + \Delta S_{tr} = 0$, and the critical density is $\rho_c \sim 1/(L^2 D)$, or a critical volume fraction is given by $\emptyset_c = V_{rods}/V \sim (NLD^2)/(NL^2 D) = D/L$.

The Onsager model is based on monodisperse spherocylinders with only hard-rod interactions and its applicability is limited to real systems. Building blocks in most real systems are polydisperse and there are additional interactions between them, for example, electrostatic, steric, and solvation interactions.[39, 40] These interactions can alter the effective diameter and the degree of dispersion of building blocks, and thus also influence their organization behavior.

In addition to fundamental issues related to self-organization of particles and their liquid crystal behavior, research on inorganic compounds opens the way toward devices that would take benefit from intrinsic properties of minerals such as large refractive index, absorption dichroism, ferroelectricity or ferromagnetism. A largely unexplored area in this field is the designed synthesis of anisotropic magnetic materials and their assembly into liquid crystals with magnetically tunable optical properties, which are in fact of both fundamental and practical importance. From the fundamental point of view, they served as ideal model systems in condensed matter physics, which allow explorations of the phase complexity in a single liquid crystal sample as the inter-particle interactions can be conveniently tuned by magnetic fields within an experimentally accessible timescale. A more in-depth understanding in the phase transitions and the related changes of optical property of the liquid crystal sample under magnetic fields can be achieved. From a practical point of view, the ionic strength of colloidal suspensions made it especially difficult to electrically switch the orientation of inorganic liquid crystals causing a short-circuit problem; while magnetically-switchable liquid crystal samples do not have this issue but benefit from the instantaneous and contactless nature of magnetic manipulation. In order to achieve magnetically tunable liquid crystals, incorporation of ferro- or ferrimagnetic materials into liquid crystals has been attempted, although a long interaction time is usually required to induce uniform molecular alignment.[42-48] Another proposed strategy is to enhance the intrinsic magnetic property of the constituents of liquid crystals, for example, by doping rare earth metal ions into liquid crystal molecules[49-52] or by developing alternative inorganic building blocks with a higher magnetic susceptibility.[53-57] However, most such studies have been limited to paramagnetic materials, which can only be aligned in extremely strong external magnetic fields.

In this chapter, I proposed to start from the synthesis of ferromagnetic or ferrimagnetic inorganic building blocks with higher magnetic susceptibilities and then assemble them into liquid crystals, and then investigate the optical tuning of liquid crystals with a magnetic field. The optical property of a liquid crystal is determined by many factors, one of the most important is its director, the average direction of the long axes of building blocks. As the orientation of magnetic building blocks is always parallel to the fields, the direction of liquid crystals can be easily controlled by external magnetic fields. By tuning the direction to be parallel or at a certain angle to the transmission axis of cross polarizers, it is expected to gain a control over the transmittance of liquid crystals. Moreover, the optical property of liquid crystals is also related to the sizes and shapes of building blocks as well as their intrinsic optical property including light absorbance and birefringence.

## 4.2 Synthesis and Characterization

***Chemicals.*** Ethanol (denatured), anhydrous iron(III) chloride, hydrochloric acid (37 % solution in water), ammonium hydroxide (28-30 % solution in water) and tetraethyl orthosilicate (TEOS) were purchased from Fisher Scientific. Polyacrylic acid (PAA, MW = 1800), 2,2-dimethoxy-2-phenylacetophenone (DMPA), poly(ethylene glycol) diacrylate (PEGDA, MW = 700) and diethylene glycol (DEG) were obtained from Sigma-Aldrich. All chemicals were directly used as received without further treatment.

***Synthesis of FeOOH nanorods.*** The synthesis of FeOOH nanorods is based on a previous literature with small modifications.[57] Typically, 7.776 g of anhydrous $FeCl_3$ were dissolved in 80 mL of deionized water. The solution was added into 450 μL of 37% HCl and then centrifuged at 11000 rpm for 3 mins to remove precipitates. The purified solution was transferred to a 100 mL three-neck flask, heated to 98 °C, and kept at that temperature for 16 hrs with refluxing. After the reaction, the solid product was collected by centrifugation at 5000 rpm for 3 mins, and then stored in 20 mL of deionized water for future use.

***PAA functionalization of FeOOH nanorods.*** A PAA stock solution was first prepared by dissolving 0.072 g of PAA in 10 mL of deionized water. The above aqueous dispersion of FeOOH nanorods was then mixed with 10 mL of PAA stock solution under vigorous stirring. After 12 hrs, the mixture was centrifuged at 5000 rpm for 3 mins, and the solid product was washed by deionized water for at least three times.

***Synthesis of FeOOH@$SiO_2$ core/shell nanorods.*** In a typical coating procedure, 30 mg of PAA-functionalized FeOOH nanorods was dispersed in 3 ml of deionized water, and 1 mL of ammonia solution was added. The mixture was vigorously sonicated for 4 mins, and was added into 20 mL ethanol. The mixture was then transferred into a 50 mL Erlenmeyer flask, and 100 μL of TEOS was added into the mixture with stirring. After 1 hr, the silica-coated nanorods were recovered from the solution mixture by centrifugation, washed by deionized water for several times and stored in deionized water.

***Reduction of FeOOH@$SiO_2$ nanorods to $Fe_3O_4$@$SiO_2$ nanorods.*** With the protection of nitrogen, 60 mL of diethylene glycol was heated to 220 °C, to which the above FeOOH@$SiO_2$ aqueous dispersion was slowly added. The color of the mixture changed from yellow to brownish instantly, and to black at the end of the reduction. The reduction process usually took 24 hrs, after which the as-reduced $Fe_3O_4$@$SiO_2$ nanorods were collected by centrifugation, washed by ethanol for several times and dispersed in deionized water.

***Self-assembly of $Fe_3O_4$@$SiO_2$ nanorods into liquid crystal phases.*** As-reduced $Fe_3O_4$@$SiO_2$ nanorods were further purified by magnetic separation for three times. After magnetic separation, certain amounts of deionized water was added into the nanorods to yield aqueous nanorods dispersions with desired volume concentrations. Liquid crystal phases would spontaneously form as the volume concentrations of nanorods exceeded a threshold.

***Fabrication of liquid crystal PEGDA films.*** A mixture solution of PEGDA and water (volume ratio of 7:3) was prepared. As-reduced $Fe_3O_4$@$SiO_2$ nanorods were dispersed in the mixture solution and purified by magnetic separation for three times. After magnetic separation, certain amounts of PEGDA/water mixture solution was added into the nanorods to yield a nanorods dispersion with a volume concentration of 10 %. DMPA (photo-initiator) was added into the nanorods dispersion at a mass fraction of 5%. For photo-polymerization, about 2 μL of solution was used each time. It was sandwiched between one cover glass and one glass slide. A mask can be placed on the top of cover glass, and a magnet field can be applied to the sample by an NdFeB magnet if necessary. The typical exposure time to UV-light for thorough polymerization is 20 s.

***Characterization.*** The morphology of the FeOOH and $Fe_3O_4$@$SiO_2$ nanorods were characterized under a Tecnai T12 transmission electron microscope (TEM). The cross-section morphology of PEGDA films with $Fe_3O_4$@$SiO_2$ nanorods embedded inside was characterized using a Philips FEI XL30 scanning electron microscope (SEM). Magnetic property measurement of $Fe_3O_4$@$SiO_2$ nanorods was performed using a Lakeshore vibrating sample magnetometer with 736 VSM controller, Model 142A, Model 642

Electromagnet power supply and Model EM4 HV electromagnet. The magnetic moment was measured as function of applied magnetic field at room temperature. Transmittances of liquid crystals and PEGDA films were measured with an Ocean Optics HR2000CG-UV-NIR spectrometer. Microscopic and polarized microscopic observations of nanorods dispersions and films were carried out under an Applied Biosystems® ArcturusXT™ LCM System or an Omano OM339P Transmitted Light Polarizing Microscope.

The birefringence of the sample was measured under a multi-functional spectral-domain optical coherence tomography (OCT) system with a polarization-sensitive OCT function.[58] During the measurement, the sample was sealed in a glass capillary tube with an inner thickness of 300 μm and a magnetic field was applied by placing a magnet next to the sample. Images of sample were acquired by the system with nanorods aligned parallel or perpendicular to the direction of light, controlled by the external magnetic fields. The accumulated phase retardation caused by the birefringence of the sample was calculated by comparing the phase of A-lines acquired with orthogonal polarization states, using a generalized Jones-matrix based analysis.[59] The birefringence was then found from this phase difference and the known thickness of the sample.

For the optical modulation test of liquid crystals, an aqueous liquid crystal sample is sandwiched between two glass slides and placed in between a polarizer and an analyzer. The thickness of sample liquid film is approximately 100 μm. The magnetic field was generated by a Helmholtz coil which is driven by an audio amplifier which in turn is driven by a generator. A compensating capacitor is used to counteract the inductive reactance due to the solenoid for a given frequency. A constant intensity polarized laser beam is directed at the sample, goes through the sample, and is detected by a photodetector which in turn is monitored by an oscilloscope.[60, 61]

Figure 4.1 shows the schematic diagram of the experimental setup. During the measurement, the generator input a 100 Hz alternating current signal to the Helmholtz coil, and an alternating magnetic field is created accordingly. The direction of magnetic field can be either along the blue arrow in the scheme, or opposite to it. The quickly switching of the field direction from one side to the opposite side results in the oscillation of nanorods. As their orientaion become temporarily displaced from their equilibrium position, laser beam passes through the cross polarizer and gives a detectable signal. Nanorods orient themselves parallel to the field twice within one full cycle, and hence twice allowing maximum light passage, resulting in a response frequency of 200 Hz.

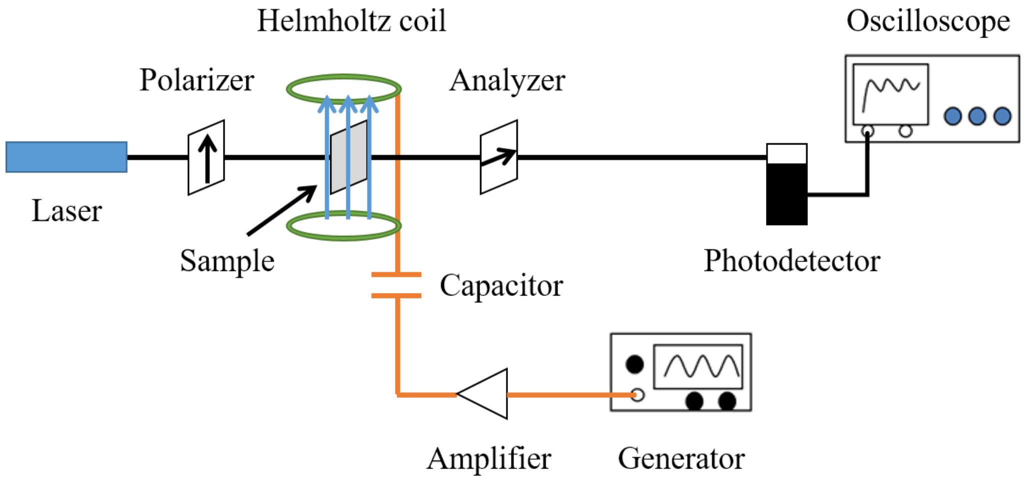

**Figure 4.1** Scheme for the optical modulation experimental setup.

## 4.3 Results and Discussion

The major challenge of our proposed work lies in the controlled synthesis of anisotropic magnetic building blocks. Even with the significant advances in colloidal synthesis achieved in the past two decades, preparation of magnetic (Fe, Co, Ni or magnetite) anisotropic nanostructures with uniform size and well defined shape has remained difficult. Herein, our strategy involves the preparation of nonmagnetic anisotropic nanostructures as precursors, surface passivation to enhance the colloidal stability, and then conversion of the precursors into magnetic anisotropic nanostructures, as schematized in Figure 4.2. Metal (Fe, Co and Ni) hydroxides are long known to grow into anisotropic shapes because of their low-symmetry crystal lattices, and are thus excellent starting materials. A representative TEM image of FeOOH nanorods is shown in Figure 4.3a. The FeOOH nanorods were further coated with a layer of silica through a sol–gel process and then reduced to $Fe_3O_4$ by diethylene glycol at an elevated temperature. As shown in Figure 4.3b, the product maintains a well-defined rod-like morphology, with an average length of 1.5 μm and diameter of 200 nm. XRD patterns of FeOOH nanorods and as-reduced $Fe_3O_4$@$SiO_2$ nanorods in Figure 4.3c confirm their materials phases. Magnetic hysteresis loop measurement reveals the ferrimagnetic nature of $Fe_3O_4$@$SiO_2$ nanorods, showing a saturated magnetization of 18 emu/g and a coercivity of 300 Oe and suggesting their good response to external magnetic fields, as shown in Figure 4.3d. The silica layer on the nanorods surface plays an important role in their stabilization in the colloidal dispersion: it acts as a physical barrier to separate the magnetic cores from each other, attenuates their magnetic dipole–dipole interactions, and prevents them from aggregating. The abundant hydroxyl groups on the silica surface provide sufficient long-range electrostatic repulsion and short-range solvation forces for stabilizing the magnetic nanorods, granting them excellent dispersibility in various polar solvents such as water and alcohols.

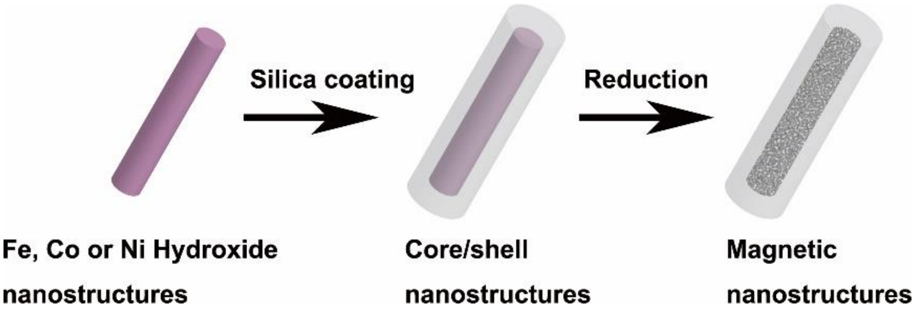

**Figure 4.2** Scheme for the preparation of magnetic anisotropic nanostructures.

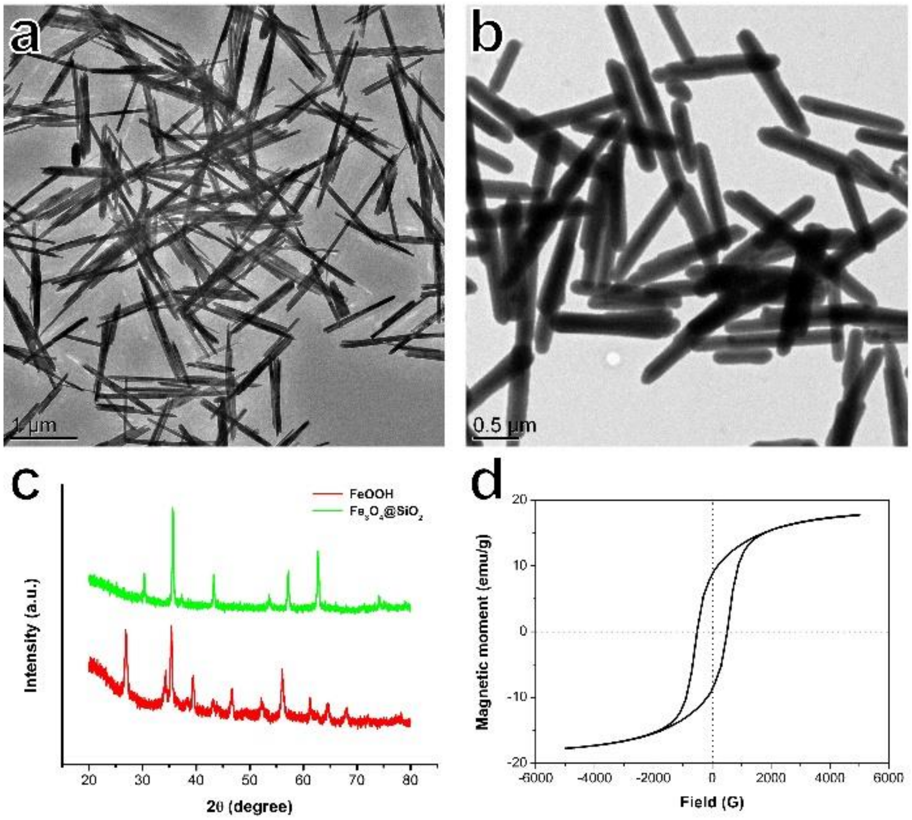

**Figure 4.3** (a) A representative TEM image of FeOOH nanorods; (b) A representative TEM image of $Fe_3O_4@SiO_2$ nanorods; (c) XRD patters of FeOOH nanorods and $Fe_3O_4@SiO_2$ nanorods; (d) Magnetic hysteresis loop of $Fe_3O_4@SiO_2$ nanorods.

A theoretical sedimentation rate of 4.7 $\mu m \cdot min^{-1}$ for magnetic rods was calculated based on a model for the sedimentation of cylinders in the dilute limit.[62] Experimentally, for a suspension of magnetic rods in water with a volume fraction ($\Phi$) of 1%, I measured a much lower sedimentation rate of 0.70 $\mu m \cdot min^{-1}$ for days 2 to 4, and a rate of 0.65 $\mu m \cdot min^{-1}$ for days 5 to 6.[63] This value is expected to further decrease as the volume fraction of magnetic rods and the viscosity of suspension increased,[64, 65] and I did not observe obvious sedimentation of magnetic rods in the liquid crystal sample within a week.

Upon the application of an external magnetic field, the magnetic nanorods align themselves along the field direction, producing the orientational order needed for the formation of liquid crystals. Since the average size of the nanorods is much larger than the detection limit of conventional small angle X-ray scattering measurement, resolving the crystal structure of the sample in the magnetic field is difficult to achieve. An alternative method which allows us to directly observe the alignment of the nanorods is to fix the nanorods in a polymer matrix.[66] In this case, $Fe_3O_4$@$SiO_2$ nanorods were dispersed in a UV curable PEGDA resin at a volume fraction of 10%. Under an external magnetic field, the dispersion was exposed to UV light to initiate polymerization. The polymerized solid was cut and its cross section was examined. As shown in Figure 4.4a, a uniform alignment of nanorods could be observed, which confirmed the orientational order of the nanorods that leads to liquid crystal properties; although it is still difficult to resolve positional order by using this method.

Figure 4.4b shows the POM images of the aqueous dispersions of $Fe_3O_4$@$SiO_2$ nanorods at different volume fractions from 1% to 10%, which indicates a clear transition from an isotropic phase to an ordered nematic phase as the volume fraction increased, and confirms the liquid crystal behavior of the dispersions. Further phase transitions from nematic phase to columnar phase or smectic phase are expected at even higher volumetric fractions, as theoretically predicted [67, 68] and experimental proved, [69, 70] although solid evidence for the formation of such phases requires small angle x-ray scattering test and cannot be provided solely by polarized optical microscope observations.

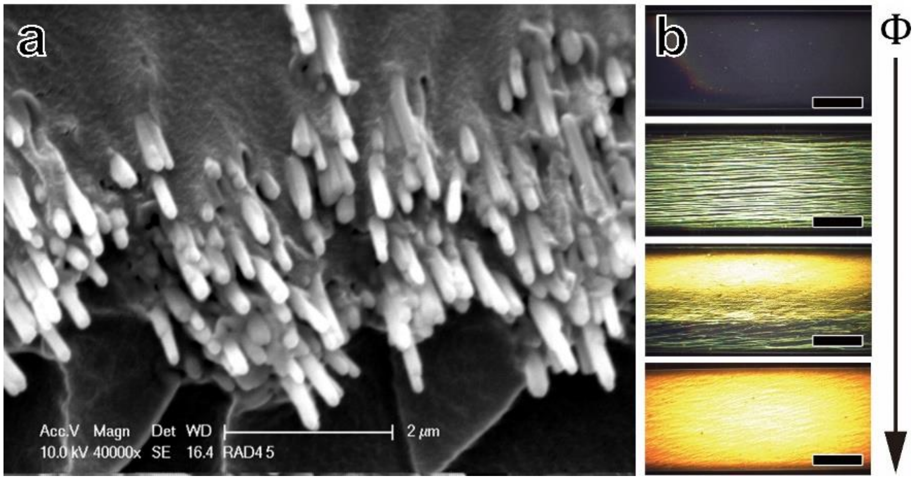

**Figure 4.4** (a) SEM image of a fixed magnetic liquid crystal in a polymer matrix showing the ordered arrangement of magnetic nanorods; (b) POM images of aqueous dispersions of $Fe_3O_4$@$SiO_2$ nanorods in a capillary tube at different volume fractions of 1%, 3%, 5% and 10% (from top to bottom). Scale bars: 500 μm.

The above results have confirmed that $Fe_3O_4$@$SiO_2$ nanorods can assemble into liquid crystal phases. In the next step, I demonstrated that the optical property of such liquid crystals can be tuned by an external magnetic field. Generally, when light enters a liquid crystal sample, it breaks up into the fast (the ordinary ray) and slow (the extraordinary ray) components.[71] Because the two components travel at different velocities, the waves get out of phase. When the rays are recombined as they exit the birefringent material, the polarization state has changed because of this phase difference. Let us consider about the case that a liquid crystal sample being sandwiched between crossed polarizers with its direction aligned at some angle to the transmission axes of crossed polarizers. Because of the birefringent nature of the sample, the incoming linearly polarized light

$$E_{incident} = \begin{pmatrix} E_x \\ E_y \end{pmatrix} = \begin{pmatrix} E_0 \cos\alpha \\ E_0 \sin\alpha \end{pmatrix}$$

becomes elliptically polarized.

$$E_{sample}(z) = \begin{pmatrix} E_x \exp ik_e z \\ E_y \exp ik_o z \end{pmatrix}$$

Using Jones calculus for optical polarizer

$$\hat{A} = \begin{pmatrix} \sin^2 \alpha & -\cos \alpha \sin \alpha \\ -\cos \alpha \sin \alpha & \cos^2 \alpha \end{pmatrix}$$

We obtain the light behind the second polarizer (analyzer),

$$E_{out} = \hat{A} E_{sample}(z = L) = E_0 \sin(2\alpha) \sin(\Delta k L/2) \exp[i(k_o + k_e)L/2] \begin{pmatrix} \sin \alpha \\ \cos \alpha \end{pmatrix}$$

and the output intensity becomes

$$I_{out} = |E_{out}|^2 = E_0^2 \sin^2(2\alpha) \sin^2\left(\frac{\Delta k L}{2}\right) = I_0 \sin^2(2\alpha) \sin^2\left(\frac{\pi \Delta n L}{\lambda}\right)$$

where $I_0$ is the intensity of light passing through the first polarizer; $\alpha$ is the angle between the transmission axes of the polarizer and the director of the liquid crystal; $\Delta n$ is the birefringence - the difference in the refractive indices of liquid crystals along the fast direction and the slow direction; $L$ is the sample thickness; and $\lambda$ is the wavelength of incident light. Therefore, when this ray reaches the second polarizer, there is now a component that can pass through, and the region appears bright. If the transmission axis of the first polarizer is parallel to either the ordinary or extraordinary directions, the light is not broken up into components, and no change in the polarization state occurs. In this case, there is no transmitted component and the region appears dark.

The birefringence of the liquid crystals formed by $Fe_3O_4$@$SiO_2$ nanorods was measured to be 0.15 and did not show significant change as the field strength increased, suggesting a good alignment of the nanorods even under weak magnetic fields. When the field direction was parallel or perpendicular to the polarizer, the long axes of nanorods were parallel to the transmission axes of crossed polarizers. $\alpha$ was equal to 0° or 90°, thus only dark optical views could be obtained, as shown in Figure 4.5a and 4.5c. As the field direction turned to 45° relative to the polarizer, $\alpha$ changed to 45°, and then the intensity reached the maximum, resulting in bright views under POM, as shown in Figure 4.5b and 4.5d. In contrast, the corresponding bright field optical microscopy images of the same sample did not show apparent differences in the darkness of the view in response to the changes in the direction of the magnetic field, as indicated in Figure 4.5e – 4.5h. The magnetic torque exerted on the liquid crystals is so strong that it overwhelms the substrate and boundary effects. All the nanorods reorient instantly as the magnetic field applied, no difference in the orientations of rods near the edge and rods far away from the edge is observed, as suggested by Figure 4.6.

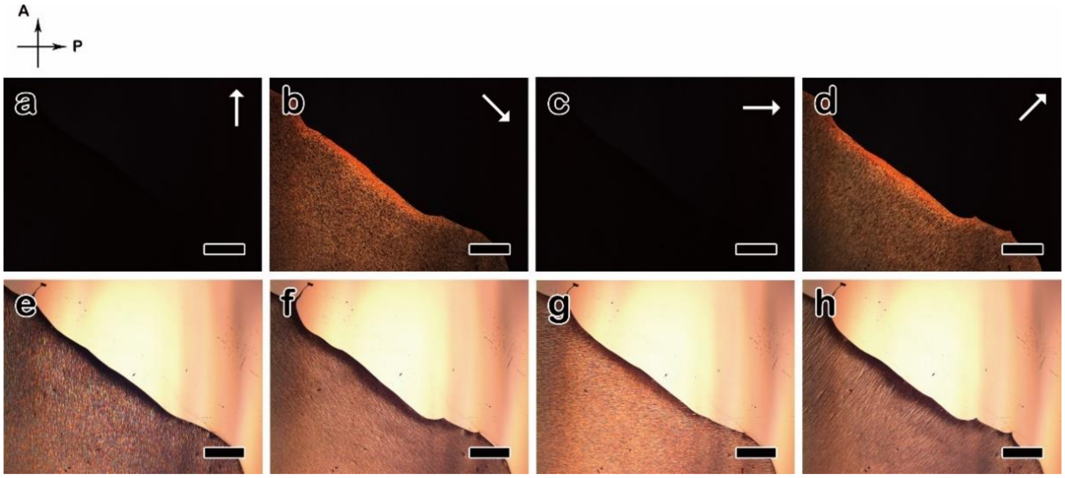

**Figure 4.5** (a-d) POM images and (e-h) bright-field OM images of a magnetic liquid crystal film under magnetic fields oriented in different directions. Black arrows at the top-left indicate the transmission axis of the polarizer (P) and analyzer (A). White arrows indicate the direction of magnetic fields. The top-right corner in each image contains no sample. Scale bars: 500 μm.

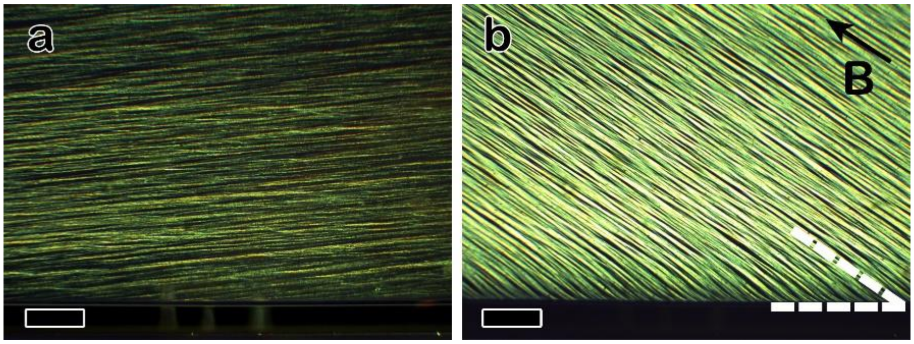

**Figure 4.6** Polarized optical microscope images of liquid crystals near the edge of capillary tube in the (a) absence and (b) presence of a magnetic field. Scale bar: 100 μm.

In order to obtain a quantitative understanding of its switching frequency, I studied the optical properties of the liquid crystal under a high-frequency alternating magnetic field. Upon the application of a high-frequency alternating magnetic field, magnetic nanorods oscillate as a result of the quick switching of field polarity from one direction to the opposite.[60, 72, 73] As the orientation of the nanorods is temporarily displaced from the equilibrium position, which is parallel to the transmission axis of the polarizer, a laser beam passes through the cross polarizer and gives a detectable light signal. The strength of signal is measured and plotted in Figure 4.7. The black curve in Figure 4.7b indicates that this liquid crystal exhibits a rapid response to an alternating 5 mT field. The transmittance changes drastically within 0.01 s, corresponding to a switching frequency of 100 Hz, while in a control experiment, no transmittance change is observed in the absence of the liquid crystal sample (red curve).

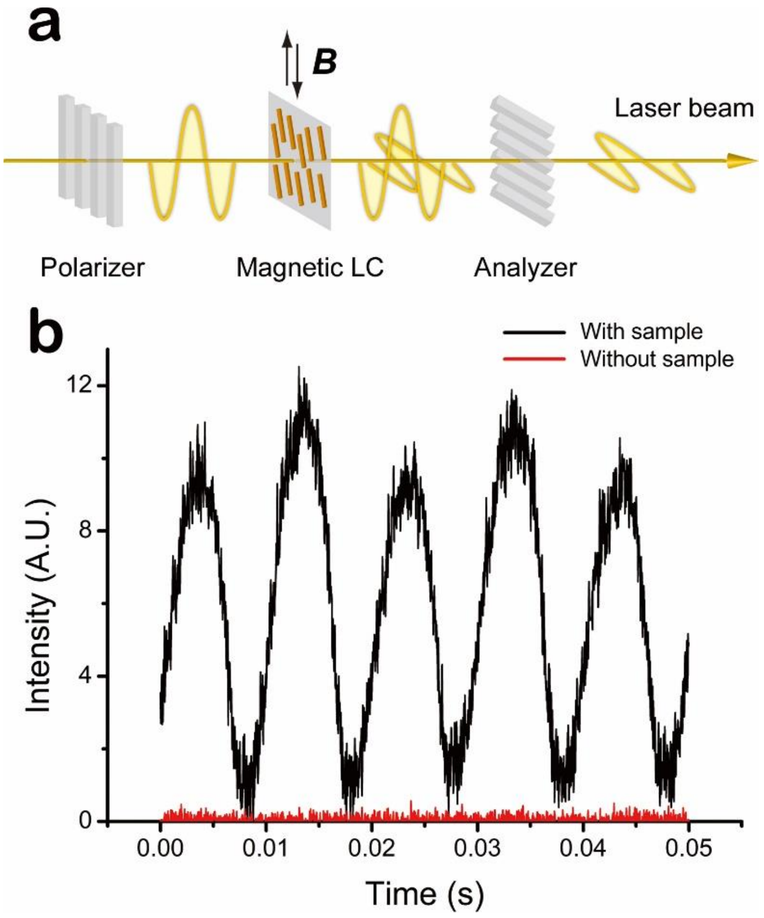

**Figure 4.7** (a) Scheme for tuning the optical property of liquid crystals; (b) The transmittance intensity profile of a magnetic liquid crystal under an alternating magnetic field.

One advantage of magnetic liquid crystals is the possibility for convenient fixation of the orientational order. In our previous study, we demonstrated that thin films patterned with various optical polarizations can be conveniently produced by combining the magnetic liquid crystals with lithography processes.[74] As schematically shown in Figure 4.8a, a liquid crystal solution containing magnetic nanorods and PEGDA resin was first sandwiched between a glass cover slip and a glass slide to form a liquid film. A photomask was then placed on top of the sample, followed by the application of a magnetic field. Upon exposure to UV light, the orientation of the nanorods in the uncovered regions was fixed along a specific direction within the plane of the film. The photomask was then removed and the sample was again exposed to UV light in the presence of a magnetic field rotated 45° (in plane) from the initial field direction. In the end, it is obtained a thin film with polarization patterns showing different transmittances to a polarized light. Figure 4.8b – 4.8d display the POM images of as-prepared samples after the application of different patterns. In these cases, the transmission axis of the polarizer was set to be parallel to the initial field direction. The areas cured during the first exposure appear dark under the POM, owing to the parallel arrangement of the nanorods relative to the transmission axis of the polarizer, while the areas cured during the second exposure are bright since all nanorods are oriented 45° relative to the transmission axis of the polarizer. An enlarged bright field optical microscopy image is shown in Figure 4.8e, which accentuates the alignment of the nanorods at the boundary of the bright (left) and dark (right) areas (separated by the dotted line), and clearly confirms the 45° angle between the two orientations.

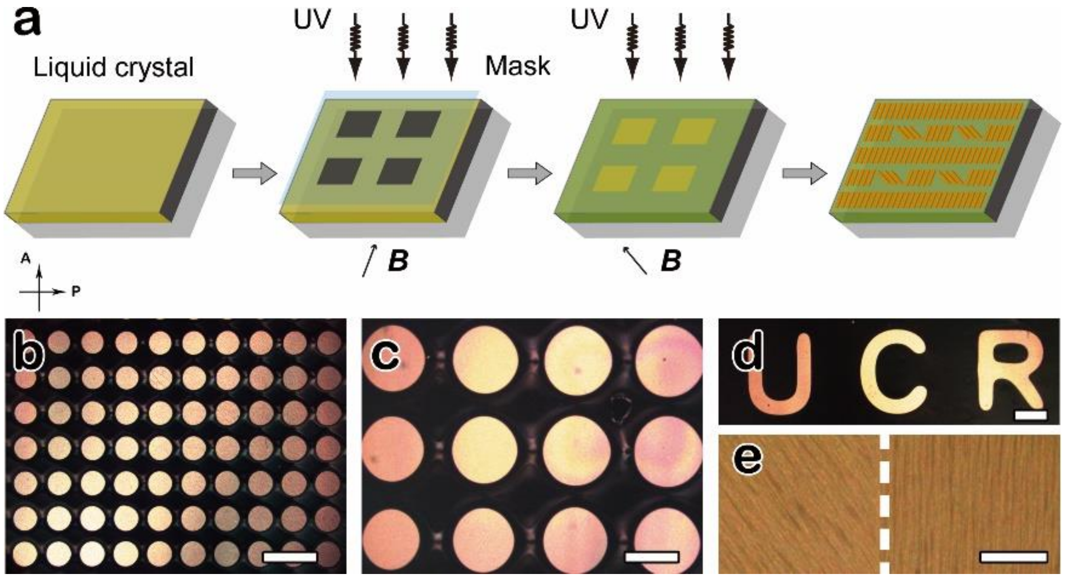

**Figure 4.8** (a) Scheme showing the lithography process for the fabrication of thin films with patterns of different polarizations; (b-d) POM images of various polarization-modulated patterns; (e) enlarged OM image shows the arrangement of nanorods in the pattern (left) and surrounding area (right). Scale bars: (b-d) 500 μm; (e) 10 μm.

Changing the orientation of the nanorods relative to the transmission axis of the polarizer allows convenient modulation of the transmittance intensity. As depicted in the extreme cases in Figure 4.9a – 4.9d, shifting the transmission axis of the polarizer to be parallel to the direction of the second field completely reverses the dark and bright areas, while almost no contrast can be observed under their bright-field optical images (Figure 4.9e and 4.9f). In Figure 4.9g, I have plotted the dependence of measured transmittance on the angle between the orientation of the nanorods and the transmission axis of the polarizer, which is in accordance with previous theory. The transmittance of the polarized light of the film or consequently its brightness under POM can be fully modulated by controlling the relative orientation of the nanorods in different areas during the lithographic processes.

Figure 4.9h demonstrates a single film with varying brightness in different areas fabricated by a multi-step lithography process, in which the magnetic field was gradually shifted from 0° to 45° relative to the transmission axis of the polarizer. More interestingly, if we only perform the first curing process, the uncured areas remain in the liquid phase so that the orientation of the nanorods within can still be tuned by magnetic fields, allowing continuous change in the contrast between the pattern and the background.

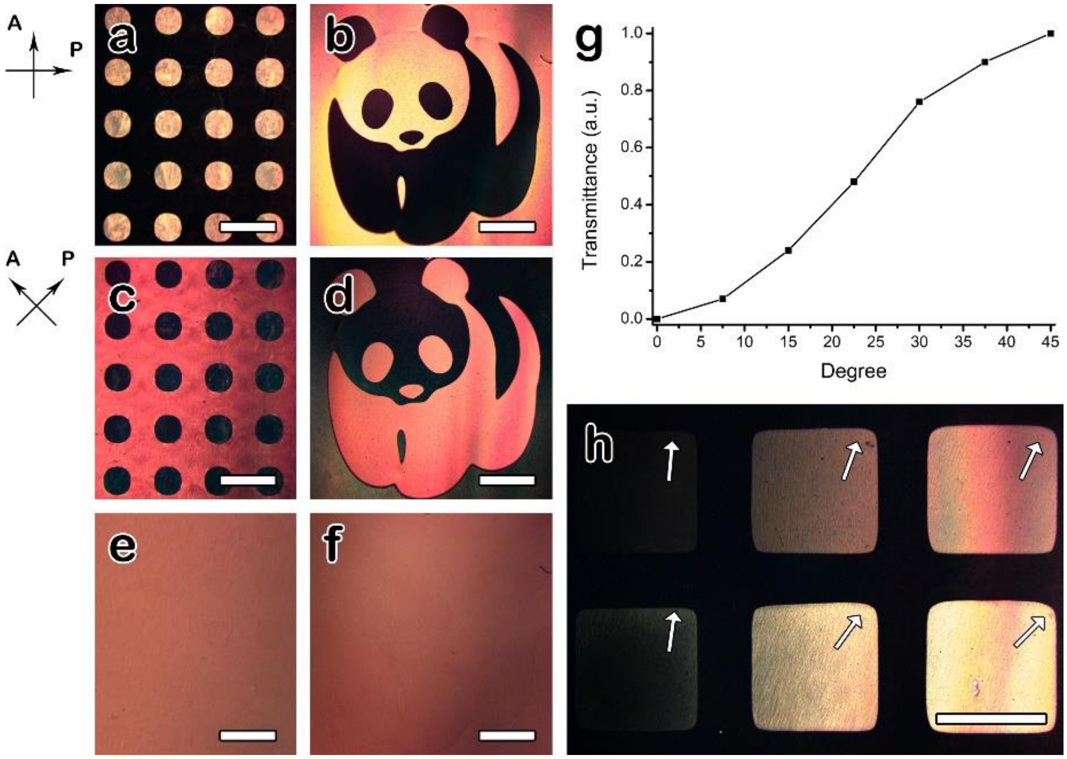

**Figure 4.9** (a-d) POM images of two polarization-modulated patterns under cross polarizers before (a-b) and after (c-d) shifting the direction of the transmission axis of the polarizers for 45°; (e-f) bright-field images of the same patterns; (g) A plot of the dependence of the thin film transmittance on the angle between the nanorod orientation and the transmission axis of the polarizer; (h) POM image of a single thin film patterned with different brightness in different areas by controlling the relative orientation of the nanorods, which is indicated by the white arrows. Scale bars: 500 μm.

The above magnetic tunable liquid crystal films may be instantly used for many optical applications. However, since magnetite is a black material and can absorb visible light, the use of magnetite in liquid crystals may limits their practical applications. I have investigated the transmittances of all the liquid crystal samples used throughout this chapter. The transmission spectra of the liquid crystal thin liquid and solid (PEGDA) films with different thickness were measured, as shown in Figure 4.10a. The relationship between the transmittance of the liquid crystal films and their thicknesses were also plotted. It can be found that liquid crystal films with a thickness of 30 μm can generally allow half of the light passing through. Given that liquid crystals involved in most applications are typically in the form of thin films, there can still be sufficient light transmission and the absorption of iron oxide may not be a big limitation.

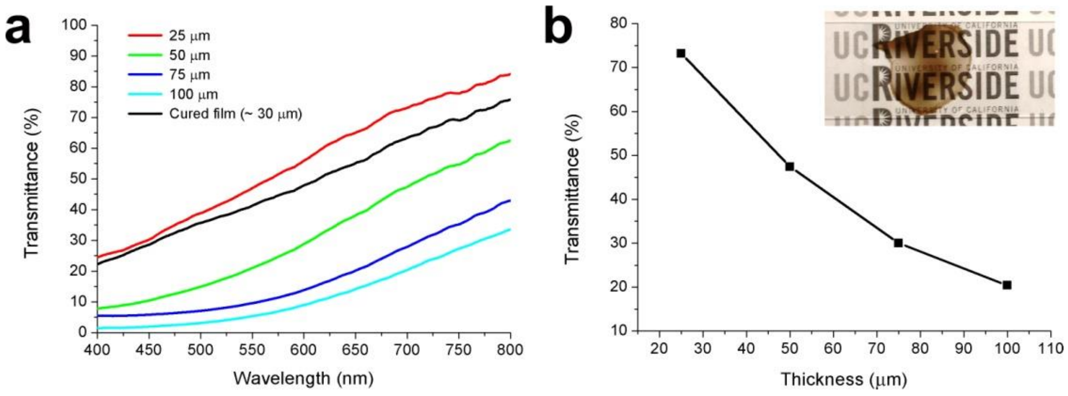

**Figure 4.10** (a) Transmittance of aqueous dispersions of Fe$_3$O$_4$@SiO$_2$ nanorods with different liquid film thickness and a cured film with Fe$_3$O$_4$@SiO$_2$ nanorods embedded inside; (b) Plot of transmittance at 700 nm on the thickness of liquid films. Inset: A digital image of a UV-cured film with a thickness of 30 μm.

## 4.4 Conclusion

In summary, I have successfully produced a magnetically actuated liquid crystal system based on magnetic iron oxide nanorods, and demonstrated its instantaneous and reversible orientational tuning using magnetic fields. Depending on the direction of the applied external field, this liquid crystal alters the polarization of light and is thus able to control the intensity of the light transmitted through it. Optical switching tests indicate that this liquid crystal is extremely sensitive to the directional change of external magnetic fields and exhibits an instant response within 0.01 s. The magnetic nanorods can also be dispersed in a UV curable resin to produce thin film liquid crystals, the orientation of which can be fixed completely or in selected areas by combining magnetic alignment and lithography processes, allowing the creation of patterns of different polarizations and control over the transmittance of light in particular areas. Although the absorption of iron oxide can limit some potential applications, the liquid film involved in most optical applications are typically in the form of thin films which can still allow sufficient transmittance of the light. The magnetically actuated liquid crystal reported here is therefore expected to provide a new platform for fabricating novel optical devices that can be widely applied in many fields, such as displays, waveguides, actuators, optical modulators, and anti-counterfeiting features.

## 4.5 Reference

1. Frank, F.C., *On the Theory of Liquid Crystals*. Discussions of the Faraday Society, 1958(25): p. 19-28.

2. Chandrasekhar, S., *Recent Developments in the Physics of Liquid-Crystals*. Contemporary Physics, 1988. **29**(6): p. 527-558.

3. Stephen, M.J. and J.P. Straley, *Physics of Liquid-Crystals*. Reviews of Modern Physics, 1974. **46**(4): p. 617-704.

4. Soref, R.A., *Physics and Chemistry of Liquid-Crystals*. Sid International Symposium Digest of Technical Papers, 1971. **11**(May): p. 122-&.

5. Ikeda, T. and O. Tsutsumi, *Optical Switching and Image Storage by Means of Azobenzene Liquid-Crystal Films*. Science, 1995. **268**(5219): p. 1873-1875.

6. Schadt, M. and W. Helfrich, *Voltage-Dependent Optical Activity of a Twisted Nematic Liquid Crystal*. Applied Physics Letters, 1971. **18**(4): p. 127-&.

7. Gooch, C.H. and H.A. Tarry, *Optical-Properties of Twisted Nematic Liquid-Crystal Structures with Twist Angles Less Than 90 Degrees*. Journal of Physics D-Applied Physics, 1975. **8**(13): p. 1575-1584.

8. Thomsen, D.L., et al., *Liquid crystal elastomers with mechanical properties of a muscle*. Macromolecules, 2001. **34**(17): p. 5868-5875.

9. Deuling, H.J., *Deformation of Nematic Liquid-Crystals in an Electric-Field*. Molecular Crystals and Liquid Crystals, 1972. **19**(2): p. 123-131.

10. Wysocki, J.J., J. Adams, and W. Haas, *Electric-Field-Induced Phase Change in Cholesteric Liquid Crystals*. Physical Review Letters, 1968. **20**(19): p. 1024-&.

11. Kahn, F.J., *Electric-Field-Induced Color Changes and Pitch Dilation in Cholesteric Liquid Crystals*. Physical Review Letters, 1970. **24**(5): p. 209-&.

12. Meyer, R.B., *Effects of Electric and Magnetic Fields on Structure of Cholesteric Liquid Crystals*. Applied Physics Letters, 1968. **12**(9): p. 281-&.

13. Pieransk.P, F. Brochard, and E. Guyon, *Static and Dynamic Behavior of a Nematic Liquid-Crystal in a Magnetic-Field .2. Dynamics*. Journal De Physique, 1973. **34**(1): p. 35-48.

14. Luz, Z. and S. Meiboom, *Nuclear Magnetic-Resonance Studies of Smectic Liquid-Crystals*. Journal of Chemical Physics, 1973. **59**(1): p. 275-295.

15. Schadt, M., H. Seiberle, and A. Schuster, *Optical patterning of multidomain liquid-crystal displays with wide viewing angles*. Nature, 1996. **381**(6579): p. 212-215.

16. Chaudhari, P., et al., *Atomic-beam alignment of inorganic materials for liquid-crystal displays*. Nature, 2001. **411**(6833): p. 56-59.

17. Scheffer, T.J. and J. Nehring, *A New, Highly Multiplexable Liquid-Crystal Display*. Applied Physics Letters, 1984. **45**(10): p. 1021-1023.

18. Small, D.M., *Liquid-Crystals in Living and Dying Systems*. Journal of Colloid and Interface Science, 1977. **58**(3): p. 581-602.

19. Luzzati, V., H. Mustacchi, and A. Skoulios, *Structure of the Liquid-Crystal Phases of the Soap-Water System - Middle Soap and Neat Soap*. Nature, 1957. **180**(4586): p. 600-601.

20. Oldenbourg, R., et al., *Orientational Distribution Function in Nematic Tobacco-Mosaic-Virus Liquid-Crystals Measured by X-Ray-Diffraction*. Physical Review Letters, 1988. **61**(16): p. 1851-1854.

21. Vroege, G.J. and H.N.W. Lekkerkerker, *Phase-Transitions in Lyotropic Colloidal and Polymer Liquid-Crystals*. Reports on Progress in Physics, 1992. **55**(8): p. 1241-1309.

22. Tiddy, G.J.T., *Surfactant-Water Liquid-Crystal Phases*. Physics Reports-Review Section of Physics Letters, 1980. **57**(1): p. 1-46.

23. Cladis, P.E., *New Liquid-Crystal Phase-Diagram*. Physical Review Letters, 1975. **35**(1): p. 48-51.

24. Madsen, L.A., et al., *Thermotropic biaxial nematic liquid crystals*. Physical Review Letters, 2004. **92**(14).

25. Odijk, T., *Theory of Lyotropic Polymer Liquid-Crystals*. Macromolecules, 1986. **19**(9): p. 2313-2329.

26. Forrest, B.J. and L.W. Reeves, *New Lyotropic Liquid-Crystals Composed of Finite Nonspherical Micelles*. Chemical Reviews, 1981. **81**(1): p. 1-14.

27. Firouzi, A., et al., *Alkaline lyotropic silicate-surfactant liquid crystals*. Journal of the American Chemical Society, 1997. **119**(15): p. 3596-3610.

28. Araos, M.U. and G.G. Warr, *Self-assembly of nonionic surfactants into lyotropic liquid crystals in ethylammonium nitrate, a room-temperature ionic liquid*. Journal of Physical Chemistry B, 2005. **109**(30): p. 14275-14277.

29. Hill, R.M., et al., *Lyotropic Liquid-Crystal Phase-Behavior of Polymeric Siloxane Surfactants*. Langmuir, 1993. **9**(11): p. 2789-2798.

30. Atkin, R., S.M.C. Bobillier, and G.G. Warr, *Propylammonium Nitrate as a Solvent for Amphiphile Self-Assembly into Micelles, Lyotropic Liquid Crystals, and Microemulsions*. Journal of Physical Chemistry B, 2010. **114**(3): p. 1350-1360.

31. van der Kooij, F.M. and H.N.W. Lekkerkerker, *Formation of nematic liquid crystals in suspensions of hard colloidal platelets*. Journal of Physical Chemistry B, 1998. **102**(40): p. 7829-7832.

32. Li, L.S., et al., *Semiconductor nanorod liquid crystals*. Nano Letters, 2002. **2**(6): p. 557-560.

33. Jana, N.R., et al., *Liquid crystalline assemblies of ordered gold nanorods*. Journal of Materials Chemistry, 2002. **12**(10): p. 2909-2912.

34. Meuer, S., et al., *Liquid crystalline phases from polymer-functionalized TiO2 nanorods*. Advanced Materials, 2007. **19**(16): p. 2073-+.

35. Xu, T. and V.A. Davis, *Liquid Crystalline Phase Behavior of Silica Nanorods in Dimethyl Sulfoxide and Water*. Langmuir, 2014. **30**(16): p. 4806-4813.

36. van der Beek, D. and H.N.W. Lekkerkerker, *Liquid crystal phases of charged colloidal platelets*. Langmuir, 2004. **20**(20): p. 8582-8586.

37. Gabriel, J.C.P. and P. Davidson, *New trends in colloidal liquid crystals based on mineral moieties*. Advanced Materials, 2000. **12**(1): p. 9-+.

38. Davidson, P. and J.C.P. Gabriel, *Mineral liquid crystals*. Current Opinion in Colloid & Interface Science, 2005. **9**(6): p. 377-383.

39. Davidson, P. and J.C.P. Gabriel, *Self-Assemblies of Anisotropic Nanoparticles: Mineral Liquid Crystals*. Nanocrystals Forming Mesoscopic Structures, 2005: p. 173-212.

40. Gabriel, J.C.P. and P. Davidson, *Mineral liquid crystals from self-assembly of anisotropic nanosystems*. Colloid Chemistry 1, 2003. **226**: p. 119-172.

41. Onsager, L., *The Effects of Shape on the Interaction of Colloidal Particles*. Annals of the New York Academy of Sciences, 1949. **51**(4): p. 627-659.

42. Fabre, P., et al., *Ferrosmectics - a New Magnetic and Mesomorphic Phase*. Physical Review Letters, 1990. **64**(5): p. 539-542.

43. Brochard, F. and P.G.D. Gennes, *Theory of Magnetic Suspensions in Liquid Crystals*. Journal De Physique, 1970. **31**(7): p. 691-&.

44. Podoliak, N., et al., *Macroscopic optical effects in low concentration ferronematics*. Soft Matter, 2011. **7**(10): p. 4742-4749.

45. Garboyskiy, Y., et al., *Increasing the switching speed of liquid crystal devices with magnetic nanorods*. Applied Physics Letters, 2012. **101**(18).

46. Chen, S.H. and N.M. Amer, *Observation of Macroscopic Collective Behavior and New Texture in Magnetically Doped Liquid-Crystals*. Physical Review Letters, 1983. **51**(25): p. 2298-2301.

47. Vallooran, J.J., S. Bolisetty, and R. Mezzenga, *Macroscopic Alignment of Lyotropic Liquid Crystals Using Magnetic Nanoparticles*. Advanced Materials, 2011. **23**(34): p. 3932-+.

48. Cordoyiannis, G., et al., *Effects of magnetic nanoparticles with different surface coating on the phase transitions of octylcyanobiphenyl liquid crystal*. Physical Review E, 2009. **79**(1).

49. Binnemans, K., et al., *Rare-earth-containing magnetic liquid crystals*. Journal of the American Chemical Society, 2000. **122**(18): p. 4335-4344.

50. Galyametdinov, Y., et al., *Synthesis and magnetic investigations on rare-earth-containing liquid crystals with large magnetic anisotropy*. Chemistry of Materials, 1996. **8**(4): p. 922-926.

51. Galyametdinov, Y.G., et al., *Magnetic alignment study of rare-earth-containing liquid crystals*. Journal of Physical Chemistry B, 2007. **111**(50): p. 13881-13885.

52. Griesar, K., et al., *A ferrimagnetically coupled liquid crystal*. Advanced Materials, 1997. **9**(1): p. 45-&.

53. Abecassis, B., et al., *Aqueous Suspensions of GdPO4 Nanorods: A Paramagnetic Mineral Liquid Crystal*. Journal of Physical Chemistry B, 2012. **116**(25): p. 7590-7595.

54. Lemaire, B.J., et al., *Outstanding magnetic properties of nematic suspensions of goethite (alpha-FeOOH) nanorods*. Physical Review Letters, 2002. **88**(12): p. 125507.

55. Thies-Weesie, D.M.E., et al., *Synthesis of goethite as a model colloid for mineral liquid crystals*. Chemistry of Materials, 2007. **19**(23): p. 5538-5546.

56. van den Pol, E., et al., *Magnetic-field-induced nematic-nematic phase separation and droplet formation in colloidal goethite*. Journal of Physics-Condensed Matter, 2011. **23**(19).

57. Hijnen, N. and P.S. Clegg, *Simple Synthesis of Versatile Akaganeite-Silica Core-Shell Rods*. Chemistry of Materials, 2012. **24**(17): p. 3449-3457.

58. Wang, Y., et al., *GPU accelerated real-time multi-functional spectral-domain optical coherence tomography system at 1300nm*. Optics Express, 2012. **20**(14): p. 14797-14813.

59. Park, B.H., et al., *Real-time fiber-based multi-functional spectral-domain optical coherence tomography at 1.3 mu m*. Optics Express, 2005. **13**(11): p. 3931-3944.

60. Ye, M.M., et al., *Self-assembly of superparamagnetic magnetite particles into peapod-like structures and their application in optical modulation*. Journal of Materials Chemistry, 2010. **20**(37): p. 7965-7969.

61. Zorba, S., et al., *Superparamagnetic Magnetite Nanoparticle Superstructures for Optical Modulation/Chopping*. Journal of Physical Chemistry C, 2010. **114**(41): p. 17868-17873.

62. Tirado, M.M., C.L. Martinez, and J.G. Delatorre, *Comparison of Theories for the Translational and Rotational Diffusion-Coefficients of Rod-Like Macromolecules - Application to Short DNA Fragments*. Journal of Chemical Physics, 1984. **81**(4): p. 2047-2052.

63. Dogic, Z., et al., *Concentration-dependent sedimentation of colloidal rods*. Journal of Chemical Physics, 2000. **113**(18): p. 8368-8380.

64. Kuijk, A., et al., *Phase behavior of colloidal silica rods*. Faraday Discussions, 2012. **159**: p. 181-199.

65. Royall, C.P., R. van Roij, and A. van Blaaderen, *Extended sedimentation profiles in charged colloids: the gravitational length, entropy, and electrostatics*. Journal of Physics-Condensed Matter, 2005. **17**(15): p. 2315-2326.

66. Ge, J., et al., *Rewritable Photonic Paper with Hygroscopic Salt Solution as Ink*. Advanced Materials, 2009. **21**(42): p. 4259-+.

67. Bates, M.A. and D. Frenkel, *Influence of polydispersity on the phase behavior of colloidal liquid crystals: A Monte Carlo simulation study*. Journal of Chemical Physics, 1998. **109**(14): p. 6193-6199.

68. Martinez-Raton, Y. and J.A. Cuesta, *Smectic and columnar ordering in length-polydisperse fluids of parallel hard cylinders*. Molecular Physics, 2009. **107**(4-6): p. 415-422.

69. Lemaire, B.J., et al., *Magnetic-field-induced nematic-columnar phase transition in aqueous suspensions of goethite (alpha-FeOOH) nanorods*. Physical Review Letters, 2004. **93**(26): p. 267801.

70. Vroege, G.J., et al., *Smectic liquid-crystalline order in suspensions of highly polydisperse goethite nanorods*. Advanced Materials, 2006. **18**(19): p. 2565-+.

71. Gennes, P.G.d. and J. Prost, *The physics of liquid crystals*. 2nd ed. Oxford science publications. 1993, Oxford

72. Zorba, S., et al., *Superparamagnetic Magnetite Nanoparticle Superstructures for Optical Modulation/Chopping*. Journal of Physical Chemistry C, 2010. **114**(41): p. 17868-17873.

73. Wang, M.S., et al., *Magnetic Tuning of Plasmonic Excitation of Gold Nanorods*. Journal of the American Chemical Society, 2013. **135**(41): p. 15302-15305.

74. Wang, M.S., et al., *Magnetically Actuated Liquid Crystals*. Nano Letters, 2014. **14**(7): p. 3966-3971.

# Chapter 5

## Magnetic Tuning of Plasmonic Excitation of Gold Nanorods

### 5.1 Introduction

Noble metal nanoparticles have been used, albeit unknowingly, for thousands of years. Medieval artisans had been creating nanoparticles when utilizing gold for pigmentation of stained glass windows and ceramics. One of the most famous examples of this practice is the Lycurgus Cup, a Roman artifact in which the glass exhibits dichroic behavior. This unique effect occurs because of the metallic nanoparticles that are incorporated into the glass, which scatter green light when illuminated from the outside and transmit red light when illuminated from the inside.

In 19th century, Faraday attributed these vibrant colors to very finely divided colloidal gold, or gold nanoparticles as known today. However, a theory that explains why fine noble metal particles exhibit varied colors was not proposed until fifty years after. A German scientist named Gustav Mie was able to predict the optical properties of spherical metallic nanoparticles by solving Maxwell's equation for an electromagnetic light wave interacting with small spheres having the same macroscopic frequency dependent material dielectric constant as the bulk metal.

The solution of this electrodynamic calculation with appropriate boundary conditions for a spherical object leads to a series of multiple oscillations for the extinction cross-section of the nanoparticles. For nanoparticles much smaller than the wavelength of light

($2r \ll \lambda$, or roughly $2r < \lambda_{max}/10$) only the dipole oscillation contributes significantly, and the Mie theory leads to the following relationship (dipole approximation):

$$\sigma_{ext}(\omega) = \frac{9\omega}{c}\varepsilon_m^{3/2}V\frac{\varepsilon_2(\omega)}{[\varepsilon_1(\omega) + 2\varepsilon_m]^2 + \varepsilon_2(\omega)^2}$$

where $\sigma_{ext}$ $V$ is the particle volume, $\omega$ is the angular frequency of the exciting light, $c$ is the speed of light, and $\varepsilon_m$ and $\varepsilon(\omega) = \varepsilon_1(\omega) + i\varepsilon_2(\omega)$ are the dielectric functions of the surrounding medium and the material itself respectively.

The above equation has been used extensively to explain the absorption spectra of small metallic nanoparticles in a qualitative as well as quantitative manner. The resonance condition is fulfilled when $\varepsilon_1(\omega) = -2\varepsilon_m$ if $\varepsilon_2$ is small or weakly dependent on $\omega$. In a plasmon resonance, a collective oscillation of the surface electrons that occurs when light interacts with a particle at its resonant frequency. The rapidly oscillating electrons are associated with the production of very strong electromagnetic fields in the immediate vicinity of the nanoparticle. For many metals, this occurs within the visible region of the electromagnetic spectrum, resulting in many vivid colors, as observed by Faraday, and unique optical spectra, as predicted by Mie.

The wavelengths at which resonance occurs can be manipulated by altering the size, shape, and dielectric constants of the particles and the environment surrounding the particles.[1-11] For larger nanoparticles, the dipole approximation is no longer valid and the plasmon resonance depends explicitly on the particle size as $x$ is a function of the particle radius $r$. The larger the particles become, the more important are the higher-order modes, as the light can no longer polarize the nanoparticles homogeneously. These higher-order modes peak at lower frequencies, and therefore the plasmon band red shifts with increasing particle size. In the meantime, the plasmon bandwidth increases with increasing particle size. This is illustrated experimentally from the spectra shown in Figure 5.1.

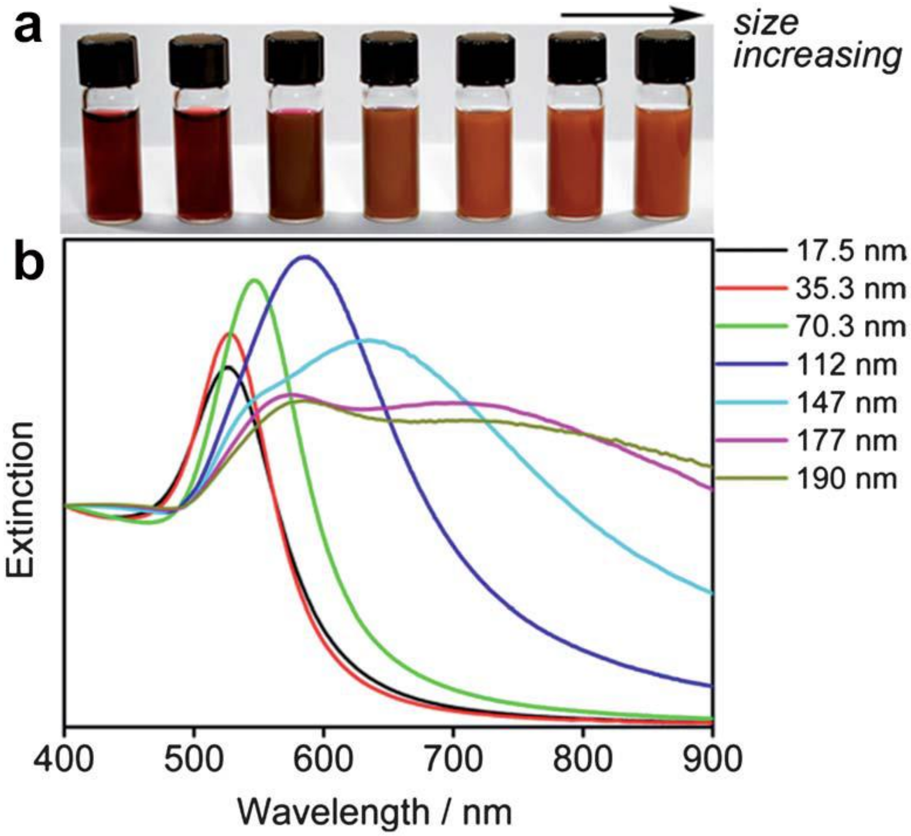

**Figure 5.1** (a) Photograph of the colloidal gold nanoparticle solutions; (b) UV-vis-NIR spectra of the gold nanoparticles with different sizes.

Shape effects seem to be even more pronounced in the plasmon resonance of nanoparticles.[12-20] The optical absorption spectrum of a collection of randomly oriented gold nanorods with aspect ratio *R* can be modelled using an extension of the Mie theory.

Within the dipole approximation according to the Gans treatment, the extinction cross-section $\sigma_{ext}$ for elongated ellipsoids is given by the following equation:

$$\sigma_{ext}(\omega) = \frac{\omega}{3c}\varepsilon_m^{3/2}V\sum_j \frac{\left(1/P_j^2\right)\varepsilon_2}{\left\{\varepsilon_1 + \left[\left(1-P_j\right)/P_j\right]\varepsilon_m\right\}^2 + \varepsilon_2^2}$$

where $P_j$ are the depolarization factors along the three axes *A*, *B* and *C* of the nanorod with *A* > *B* = *C*, defined as

$$P_A = \frac{1-e^2}{e^2}\left[\frac{1}{2e}\ln\left(\frac{1+e}{1-e}\right) - 1\right]$$

$$P_B = P_c = \frac{1-P_A}{2}$$

and the aspect ratio *R* is included in *e* as follows:

$$e = \left[1-\left(\frac{B}{A}\right)^2\right]^{1/2} = \left(1-\frac{1}{R^2}\right)^{1/2}$$

The plasmon resonance absorption band splits into two bands as the particles become more elongated along one axis.[21-24] The aspect ratio is the value of the long axis (length) divided by the short axis (width) of a cylindrical or rod-shaped particle. As the aspect ratio increases, the energy separation between the resonance frequencies of the two plasmon bands increases. The high-energy band absorbing at around 520 nm corresponds to the oscillation of the electrons perpendicular to the major (long) rod axis and is referred to as the transverse plasmon absorption. This absorption band is relatively insensitive to the nanorod aspect ratio and coincides spectrally with the surface plasmon oscillation of the nanodots. The other absorption band at lower energies is caused by the oscillation of the free electrons along the major (long) rod axis and is known as the longitudinal surface plasmon absorption. Figure 5.2 shows the colors and absorption spectra of gold nanorods with different aspect ratios. The longitudinal plasmon band maximum red shifts with increasing aspect ratio while the transverse absorption band maximum barely changes.

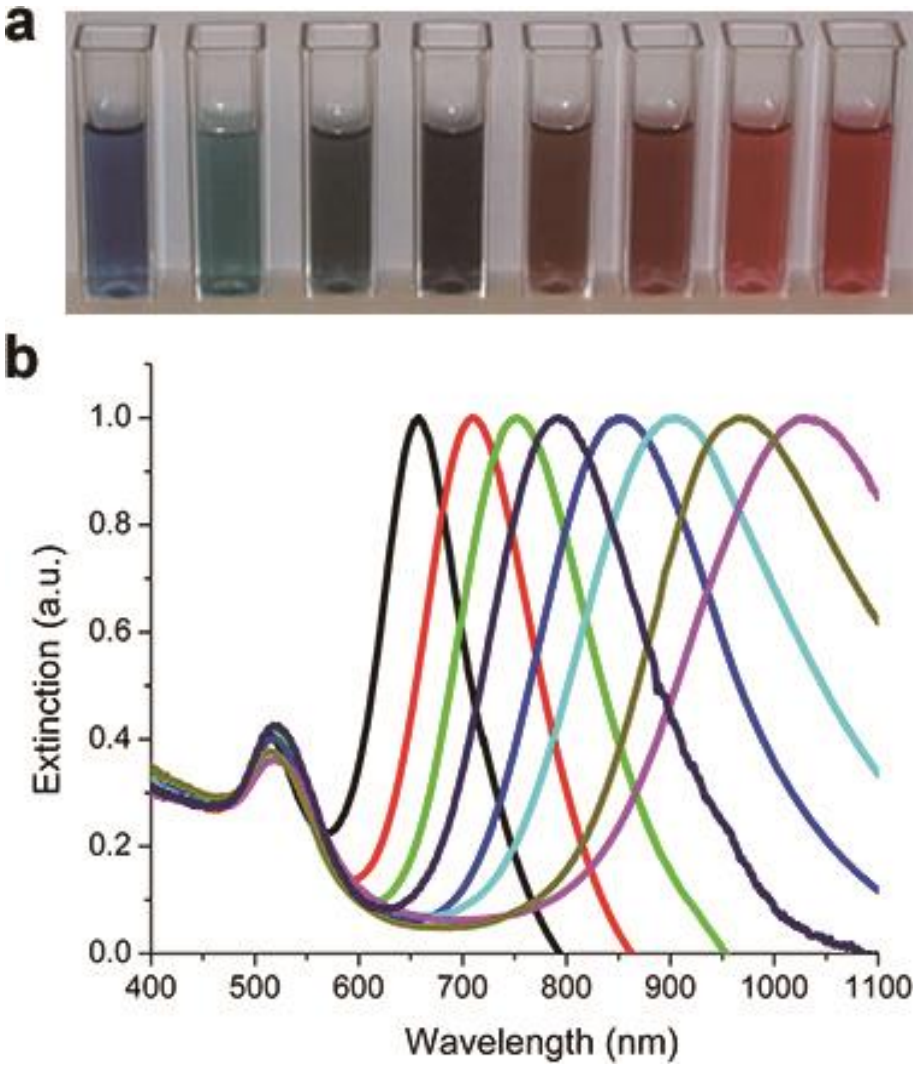

**Figure 5.2** (a) Photograph of the colloidal gold nanorods solutions with increasing aspect ratios from left to right; (b) UV-vis-NIR spectra of the gold nanorods with increasing aspect ratios from left to right.

The vibrant colors of plasmonic nanomaterials enable some instant color-related applications, such as signage and anti-counterfeit devices.[25-29] The plasmon resonance absorption of plasmonic nanoparticles has an absorption coefficient orders of magnitude larger than commercially absorbing dyes, and anisotropic-shaped nanostructures have plasmon resonance absorptions that are even stronger. In addition to the generation of vivid colors, the rapidly oscillating electrons are associated with the production of very strong electromagnetic fields in the vicinity of the nanoparticle. These fields are known to affect the properties of other materials and are of great potential to be used in nanoscale sensing applications to enhance sensitivity in modern analytical techniques based on spectroscopy. Manipulation of the surface plasmon resonance and the resulting electromagnetic fields are the focus of much of the research in the plasmonic nanostructures. Creation of novel plasmonic nanostructures with tunable optical property and desired electromagnetic fields for specific applications are the current and future goals of this field.

## 5.2 Synthesis and Characterization:

***Chemicals.*** Polyvinylpyrrolidone (PVP, MW = 10000, K15), potassium iodide (KI), hydrogen tetrachloroaurate (III) trihydrate ($HAuCl_4 \cdot 3H_2O$), hydrazine hydrate (100%, hydrazine 64%), 3-aminopropyltriethxoysilane (APS) and tetraethyl orthosilicate (TEOS) were purchased from Acros. Polyoxyethylene(10) cetyl ether (Brij C10), polyacrylic acid (PAA), L-ascorbic acid, hexadecyltrimethylammonium bromide (CTAB, $\geq$ 99%), polyacrylic acid (PAA, MW = 1800), 2,2-dimethoxy-2-phenylacetophenone (DMPA), poly(ethylene glycol) diacrylate (PEGDA, MW = 700), diethylene glycol (DEG), sodium borohydride ($NaBH_4$, 99%) and 4-styrenesulfonic acid sodium salt hydrate (NaSS) were purchased from Sigma-Aldrich. Nickel chloride hexahydrate ($NiCl_2 \cdot 6H_2O$), ethanol (denatured), sodium hydroxide (NaOH), diethylamine, hydrochloric acid (HCl, 37.5%), cyclohexane and isopropanol were purchased from Fisher Scientific. All chemicals were used as received without further purification. Deionized water was used for all the solution preparations and reactions.

***Synthesis of silica templates with rod-shaped cavities.*** In a typical synthesis, 8.5 g of Brij C10 was dissolved in 15 mL of cyclohexane and was kept at 50 °C. Under stirring, 1.0 mL of $NiCl_2$ solution (0.8 M) was added and stirred until homogeneity. After that, 0.45 mL of hydrazine hydrate was added dropwisely to form nickel-hydrazine complex nanorods. After 3 hrs of reaction, 23 μL of APS and 1 mL of diethylamine were added and the reaction system was stirred for 1.5 hrs, ensuring complete hydrolysis and condensation of APS on the surface of the newly formed nickelhydrazine nanorods. Then, 2.3 mL of TEOS were added for silica coating, which was allowed to proceed for 3 hrs. The nickel-hydrazine nanorod@silica core/shell structured material was collected by centrifugation, washed with isopropanol, and stored in 25 mL of isopropanol. 9.2 mL of the above solution was taken, centrifuged, dispersed in 35 mL of HCl (1 M), and stirred for 1 hr at room temperature. After etching, the solid was recovered by centrifugation, washed with water, and dispersed in 15 mL of ethanol containing 300 μL of ammonium hydroxide (28%) for the deprotonation of the aminopropyl groups. The solid was then washed with ethanol and stored in 15 mL of ethanol.

***Synthesis of PVP-protected gold nanorods.*** Typically, 2 mL of the above ethanol solution containing silica nanotubes was taken, centrifuged, washed with water to pH neutral, and dispersed in 0.5 mL of water. Then, 30 μL of $HAuCl_4$ (0.1 g/mL in water, 0.25 M) was added and stirred for 15 mins. The solid was collected by centrifugation, washed with water three times, and redispersed in 1 mL of water, to which was added 0.5 mL of $NaBH_4$ solution (0.1 M, freshly prepared and cooled in an ice bath). The solid dispersion turned red, forming Au seed@silica nanotube yolk/shell structures, and was then recovered by centrifugation and washed with HCl (0.01 M) and water to remove residual $NaBH_4$. The obtained Au seed@silica nanotubes were etched with 15 mL of water at 70 °C for 1 hr and were stored in 3 mL of water as a stock solution. For the subsequent seeded growth of gold nanorods, chemicals were added to a glass vial in the following order: 2 mL of water, 400 μL of PVP solution (Mw 10000, 5% wt in water), 150 μL of KI (0.2 M), 200 μL of ascorbic acid (0.1 M), and 30 μL of $HAuCl_4$ (0.1 g/mL, 0.25 M), forming a clear colorless solution (growth solution). 80 μL of the Au seed@silica stock solution was injected into the growth solution. After 8 mins of reaction, the Au nanorod@silica material was collected by centrifugation and washed with water. They were dispersed in 40 mL of PVP 10000 (1.25% wt) solution and heated to 98 °C. 200 μL of diethylamine and 200 μL of NaOH (1 M) were injected and the dispersion was stirred for 1 hr. Finally, the gold nanorods were recovered from the dispersion by centrifugation at 5000 rpm for 15 mins, and were dispersed in 10 mL of water.

***Synthesis of FeOOH nanorods.*** The synthesis of FeOOH nanorods is based on a previous literature with small modifications. In a typical synthesis, 1 g of CTAB and 1.08

g of $FeCl_3 \cdot 6H_2O$ were dissolved in 40 mL of water. The solution was centrifuged at 11000 rpm for 3 min, and the insolvable precipitates were discarded. The purified solution was heated to 85 °C with gently stirring and maintained at that temperature for 12 hrs. After the reaction, the solid product was collected by centrifugation at 11000 rpm for 12 mins, washed by water for three times, and then stored in 12 mL of deionized water for future use.

***PAA functionalization of FeOOH nanorods.*** A PAA stock solution was first prepared by dissolving 0.072 g of PAA in 10 mL of deionized water. Typically, 1 mL of the above FeOOH nanorods dispersion, 1 mL of PAA stock solution and 18 mL of water was mixed together for PAA functionalization of FeOOH nanorods. After overnight stirring, the nanorods were recovered by centrifugation and then dispersed in 3 mL of water.

***Synthesis of FeOOH@$SiO_2$ core/shell nanorods.*** In a typical coating procedure, 3 mL of the above PAA-functionalized FeOOH nanorods dispersion and 1 mL of ammonia solution was mixed together. The mixture was vigorously sonicated for 4 min, and was added into 20 mL of ethanol. The mixture was then transferred into a 50 mL Erlenmeyer flask, and 60 μL of TEOS was added into the mixture with stirring. After 1 hr, the silica-coated nanorods were recovered from the solution mixture by centrifugation, washed by water for several times and stored in 2 mL of water.

***Reduction of FeOOH@$SiO_2$ nanorods to $Fe_3O_4$@$SiO_2$ nanorods.*** With the protection of nitrogen, 60 mL of diethylene glycol was heated to 220 °C, to which the above FeOOH@$SiO_2$ aqueous dispersion was slowly added. The color of the mixture changed from yellow to brownish instantly, and to black at the end of the reduction. The reduction process usually took 24 hrs, after which the as-reduced $Fe_3O_4$@$SiO_2$ nanorods were collected by centrifugation, washed by ethanol for several times and dispersed in 6 mL of ethanol.

***Assembly of gold nanorods onto $Fe_3O_4$@$SiO_2$ nanorods.*** $Fe_3O_4$@$SiO_2$ nanorods were first modified with amino groups to ensure their affinity with gold nanorods. Typically, 500 µL of APS was added to 6 ml of ethanol dispersion of $Fe_3O_4$@$SiO_2$ nanorods. After overnight stirring, nanorods were collected by centrifugation, washed by ethanol for several times and dispersed in 6 mL of ethanol. Under the assistance of sonication, 25 µL of magnetic nanorods dispersion was added into 5 mL of the above gold nanorods dispersion. After sonication for an additional 5 mins, the hybrid gold-$Fe_3O_4$ nanorods were magnetically recovered from the solution. They were purified by magnetic separation for several times and then stored in 3 mL of water.

***Silica coating of hybrid gold-$Fe_3O_4$ nanorods.*** Hybrid gold-$Fe_3O_4$ nanorods were modified with sulfonate groups by mixing their aqueous dispersion (3 mL) with 1 mL of NaSS solution (0.1 M). After overnight stirring, hybrid nanorods were collected by centrifugation, washed by water for several times and dispersed in 3 mL of water. 1 mL of ammonia solution was added into the hybrid nanorods dispersion. The mixture was sonicated for 4 min, and was mixed with 20 mL of ethanol and 60 µL of TEOS with stirring. After 1 hr, the silica-coated hybrid nanorods were recovered from the solution mixture by centrifugation, washed by water for several times and stored in water.

***Fabrication of hybrid nanorods PEGDA films.*** A mixture solution of PEGDA and water (volume ratio of 7:3) was prepared. As-reduced $Fe_3O_4$@$SiO_2$ nanorods were dispersed in the mixture solution and purified by magnetic separation for three times. After magnetic separation, certain amounts of PEGDA/water mixture solution was added into the nanorods. DMPA (photo-initiator) was added into the nanorods dispersion at a mass fraction of 5%. The solution was then transferred into a homemade glass cell with a thickness of 1mm. A flat magnet sheet with precut shape (purchased from Mcmaster Carr) was placed at the bottom of glass cell to generate a magnetic field for the local alignment of hybrid nanorods, and the cell was exposed to UV-light for at least 1 min for the complete polymerization.

***Characterization.*** The morphology of the silica templates, gold nanorods, $Fe_3O_4$@$SiO_2$ nanorods and their assemblies was characterized by using a Tecnai T12 transmission electron microscope (TEM). The UV-Vis spectra were measured by a probe-type Ocean Optics HR2000CG-UV-Vis spectrophotometer in absorption mode with an integration time of 5 ms. Digital pictures of hybrid nanorods were taken by a Canon EOS Rebel T5i DSLR camera, with or without a Tiffen 58 mm linear polarizer glass filter.

For the optical characterization of hybrid nanorods under alternating magnetic field, an aqueous solution of nanorods is placed in a cylindrical glass cell. The length and diameter of the glass cell are 1 cm. The glass cell is positioned inside a solenoid (15 cm in length) which is driven by an audio amplifier which in turn is driven by a function generator. A compensating capacitor is used to counteract the inductive reactance due to the solenoid for a given frequency. Alternating (ac), linearly polarized magnetic fields of ~ 10 mT magnitude were facilely obtained at the center of the solenoid with tunable frequency capability. A constant intensity laser beam is directed at the sample, goes through the sample, and is finally detected by a photodetector which in turn is monitored by an oscilloscope.

### 5.3 Results and Discussion

Owing to the anisotropic distribution of surface electrons, gold nanorods display more complex resonance modes than their spherical counterparts. The oscillating electric field of an incident light induces the coherent oscillation of the conduction electrons along both the long and short axes of gold nanorods. The mean free paths of electrons travelling along the two axes are different, resulting in different oscillation frequencies and correspondingly two bands of different wavelengths in extinction spectrum. The band at a shorter wavelength is attributed to the excitation of transverse plasmon, in which electrons oscillate along the short axes, whereas the band at a longer wavelength results from the excitation of longitudinal plasmon, in which electrons oscillate along the longer axis.

The excitation of transverse and longitudinal modes is determined by the orientation of the nanorods relative to the direction of oscillating electric field of incident light, in other words, the polarization of light. When the polarization of light is parallel to the long axis of the nanorods, only the longitudinal plasmon is excited. Similarly, only the transverse mode will be excited if the polarization of light is parallel to the short axes of gold nanorods. Figure 1 schematically illustrates the excitation of plasmon modes of gold nanorods upon the incidence of ordinary light. For the simplicity in discussion, the direction of light is fixed in $y$ axis, and then the electric field of light oscillates in $xz$ plane as it is always perpendicular to the propagation direction of light. If gold nanorods are aligned along $z$

axis, both the transverse plasmon along ***x*** axis and the longitudinal plasmon along ***z*** axis will be excited, displaying two typically observed bands in the extinction spectrum. Aligning gold nanorods along the ***x*** axis leads to a similar result as both longitudinal and transverse modes can be excited. However, a dramatic difference occurs when gold nanorods are aligned along the ***y*** axis. In this case, electron oscillation only occurs along the short axes, therefore results in the excitation of transverse plasmon only.

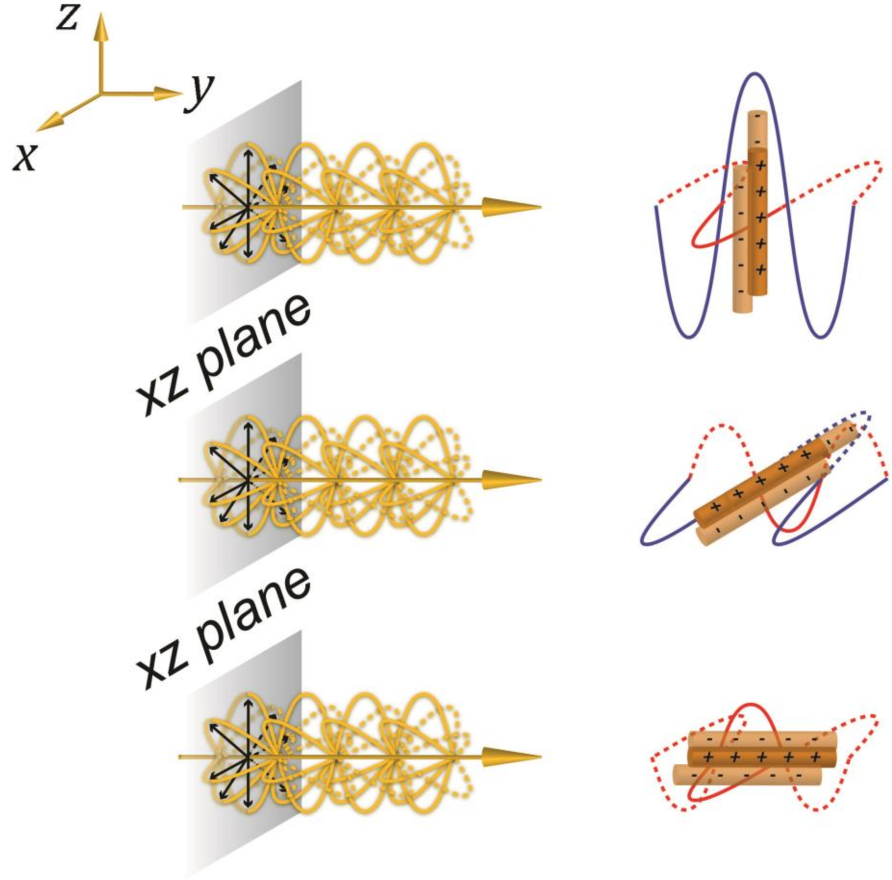

**Figure 5.3** Scheme showing the plasmon excitation of AuNRs under ordinary light. The black arrows indicate the polarization of light; blue curves represent longitudinal plasmon resonance while red curves represent transverse plasmon resonance.

The above analysis suggests a new mechanism that allows dynamic tuning of the optical property of gold nanorods even under normal light illumination. A critical question is then how to enable the desired magnetic orientational control of gold nanorods. I have developed a strategy to overcome this challenge by attaching gold nanorods to the surface of magnetic nanorods in a parallel manner, so that orientational control of gold nanorods can be simply achieved by aligning the magnetic nanorods. As magnetic nanorods tend to orient themselves parallel to the direction of the external magnetic field to minimize their magnetic potential energy, the gold nanorods attached to the magnetic nanorods will be aligned along the same direction, thus enabling magnetic control of their plasmonic excitation.

In order for the designed scheme to work, there are a few requirements on the magnetic nanorods. The most important requirement is that their net magnetization should be small enough to avoid magnetically induced aggregation, but their magnetic response should be strong enough to guarantee an effective reorientation under normal magnetic fields. The diameter of the magnetic nanorods should be kept close to that of the gold nanorods so that a parallel attachment is highly preferred when the two types of nanorods are brought together through coordination covalent bonds.

In order to produce magnetic nanorods with the required features, I have developed a unique solution phase synthesis which involves first preparation of nonmagnetic iron oxyhydroxide (FeOOH) nanorods,[30, 31] coating with a thin layer of silica through a sol-gel process, and then dehydration and reduction in diethylene glycol to produce magnetic magnetite ($Fe_3O_4$) nanostructures of a similar morphology. Representative TEM images of

FeOOH nanorods and $Fe_3O_4$@$SiO_2$ nanorods were presented in Figure 5.4a and 5.4b. The FeOOH nanorods have an average length of 200 nm and width of 40 nm. The as-reduced $Fe_3O_4$@$SiO_2$ nanorods still exhibit a well-defined rod-like morphology. The inner core of nanorods become hollow, owing to the decrease in mass and the increase in density during the reduction process. The magnetic property of $Fe_3O_4$@$SiO_2$ nanorods was also measured, as shown in Figure 5.4c. They have a saturated magnetization of 20 emu/g and a coercivity very close to zero, suggesting their superparamagnetism, and negligible inter-particle magnetic interactions in the absence of external magnetic fields. The silica layer on the surface plays important roles: it helps maintaining the rod-like morphology during reduction, prevents the as-reduced magnetic $Fe_3O_4$ from aggregation, and also facilitates the surface functionalization of magnetic nanorods with amino-groups for linking to gold nanorods.

PVP-stabilized gold nanorods were then synthesized, and one of their representative TEM images is shown in Figure 5.4d. The gold nanorods have a well-defined morphology, with an average length of 75 nm and width of 30 nm. PVP-stabilized gold nanorods were chosen particularly for their good affinity to amino-group-functionalized surfaces. There have been a lot of well-developed methods for the synthesis of gold nanorods with beautiful morphology; however, almost all of them use CTAB as a surfactant to guide the 1D growth of gold. As a result, the CTAB-capped gold nanorods are positively charged and show no affinity to positively charged amino groups.

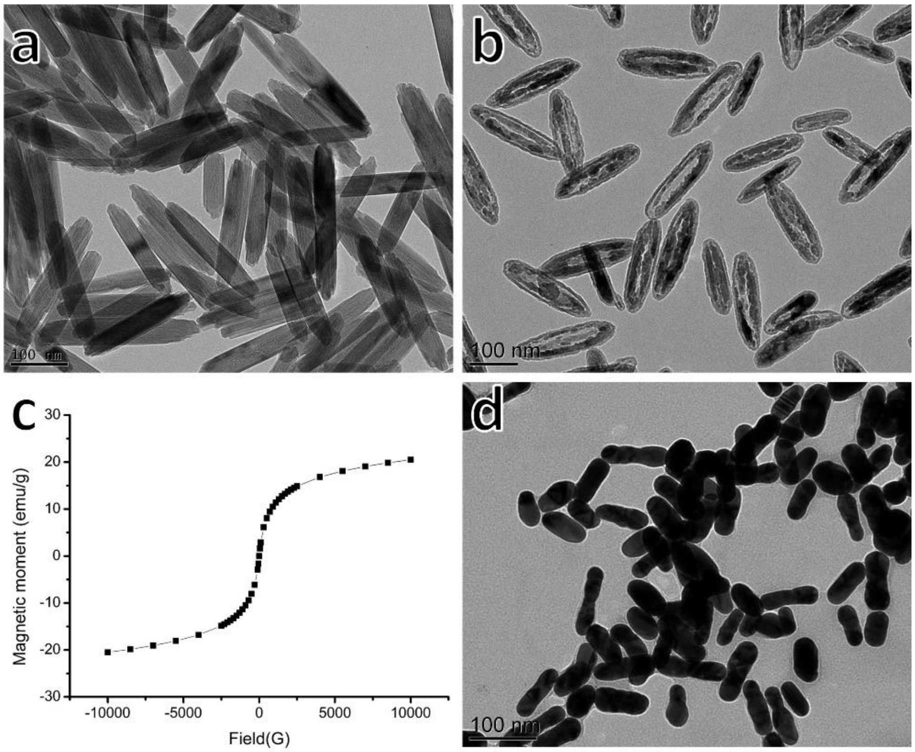

**Figure 5.4** (a) A TEM image of bare FeOOH nanorods; (b) A TEM image of the $Fe_3O_4$@$SiO_2$ nanorods; (c) Magnetic hysteresis loop of the $Fe_3O_4$@$SiO_2$ nanorods; (d) A TEM image of the gold nanorods.

The extinction spectra of the bare FeOOH nanorods, $Fe_3O_4$@$SiO_2$ nanorods and gold nanorods were measured. Owing to the intrinsic orange color of FeOOH, the aqueous dispersion of FeOOH nanorods exhibit an obvious absorption shoulder in shorter wavelengths. However, after being reduced, the absorption shoulder attenuated a lot. The extinction spectra of the gold nanorods exhibit two characteristic peaks. The peak at a shorter wavelength corresponds to the transverse plasmon excitation; while the peak at a longer wavelength corresponds to the longitudinal plasmon excitation.

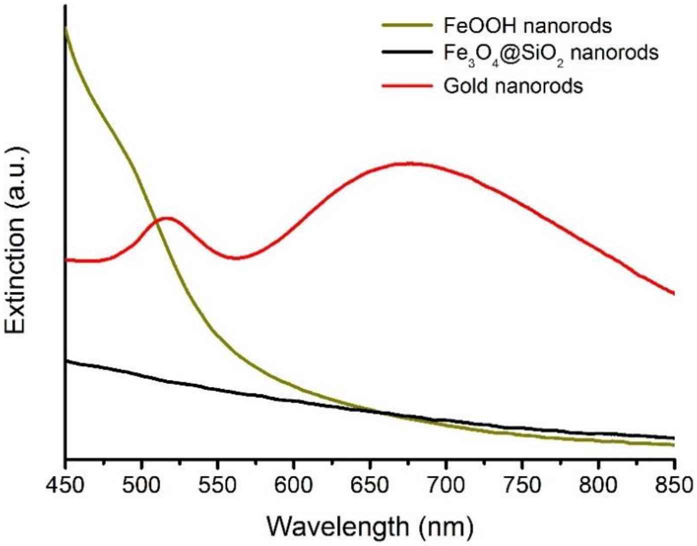

**Figure 5.5** UV-Vis extinction spectra of the FeOOH nanorods, $Fe_3O_4$@$SiO_2$ nanorods and gold nanorods.

The gold nanorods were then binded to amino-group-functionalized $Fe_3O_4$@$SiO_2$ nanorods. Due to the high affinity between gold surface and amino groups, gold nanorods tend to attach to the magnetic nanorods by maximizing the contact area, as confirmed by the TEM observation shown in Figure 5.6a. Magnetic tuning of the optical property of the gold nanorods under ordinary light was then demonstrated. In accordance with the above discussion, the perceived color of gold nanorods changed with the direction of magnetic field. When the field was parallel to the incident light, gold nanorods were aligned along the same direction so that only transverse plasmon could be excited, resulting in a red color of the dispersion; when the field was tuned perpendicular to the direction of incidence, the color turned to green owing to the dominant excitation of the longitudinal plasmon mode. The plasmon property was very sensitive to the external magnetic field, including both the field direction and field strength. As the angle between the directions of incident light and the magnetic field changed from 90° to 0°, the excitation of longitudinal mode decreased in magnitude, leading to an attenuated band at the wavelength of around 700 nm, as shown in Figure 5.5b. Meanwhile, only a slight change over the plasmon band at 520 nm could be observed as transverse plasmonic mode was always excited.

The effective rotation of nanorods requires only a weak magnetic field. As shown in Figure 5.5c, when a magnet moved along the incident direction towards the sample, the resonance band at 700 nm became significantly suppressed. A change in the extinction spectrum could be observed when the magnet was 20 cm away from the sample, which corresponds to a field strength of 8 G and indicates an acute response of the sample to magnetic fields. The band at 700 nm reached a minimum at a sample-magnet distance of 4 cm, corresponding to a field strength of 50 G. Further increasing the field strength had no effect in the extinction spectra of hybrid nanorods, suggesting that all the nanorods were aligned by external magnetic fields.

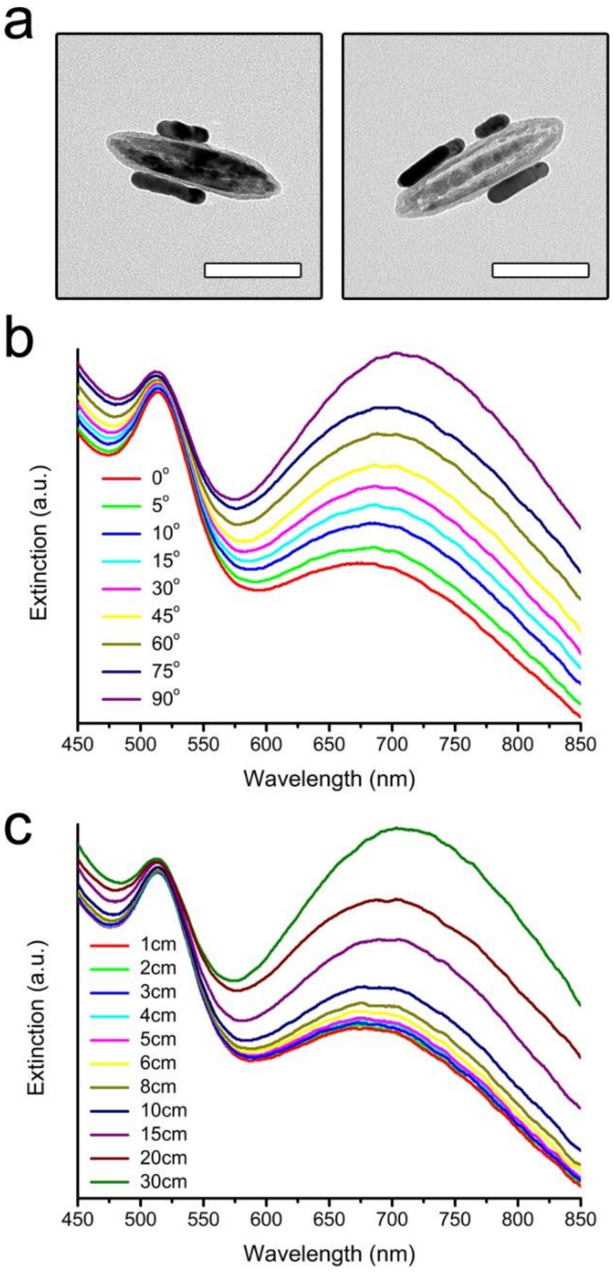

**Figure 5.6** (a) TEM images of the as-assembled structures. Scale bar: 100 nm; (b) Spectra of a dispersion of gold-$Fe_3O_4$ hybrid nanorods under external magnetic fields with different directions relative to that of the incident light (from perpendicular (90°) to parallel (0°)); (c) Spectra of the dispersion under magnetic fields with varying strengths controlled by the sample-magnet distance. The field direction is parallel to the incident direction of light.

In a control experiment, I investigated the optical property of pure gold nanorods, pure $Fe_3O_4$@$SiO_2$ nanorods and a simple mixture of gold nanorods and $Fe_3O_4$@$SiO_2$ nanorods in the absence and presence of external magnetic fields, as presented in Figure 5.6. The gold nanorods exhibit no optical response to magnetic fields; while the other two dispersions exhibit a small difference in the intensity upon the application or removal of magnetic fields, owing to the orientation change of $Fe_3O_4$@$SiO_2$ nanorods. No change in the plasmonic property of gold nanorods is observed, as their orientation cannot be controlled by external magnetic fields in this situation. This is consistent with our previous findings.

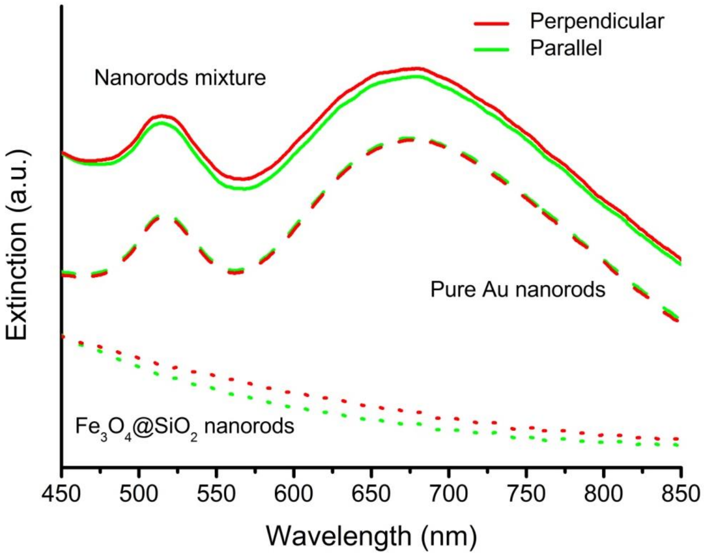

**Figure 5.7** UV-Vis spectra of pure gold nanorods, $Fe_3O_4$@$SiO_2$ nanorods and a simple mixture of two nanorods (gold nanorods not attached to $Fe_3O_4$@$SiO_2$ nanorods) under external magnetic fields with direction parallel or perpendicular to incident light.

Magnetic orientational control of gold nanorods under the illumination of linear polarized light provides more opportunity in tuning their plasmon resonance, for example, by completely suppressing either the transverse or longitudinal mode. As schematically illustrated in Figure 5.7a, under the illumination of ***z***-polarized light incident along ***y*** axis, the plasmon excitation of gold nanorods changed in different manners when they are rotated in the ***yz*** or ***xy*** planes. When gold nanorods were aligned along the ***z*** axis, the transverse mode resonance was completely suppressed, and only a strong band for longitudinal mode could be observed, as confirmed by the extinction spectra in Figure 5.7b. Rotating the nanorods from ***z*** axis towards ***y*** axis gradually enhances the transverse plasmon excitation while at the same time suppressing the longitudinal mode, as evidenced by the gradual decrease of the band at 700 nm and rising of the one at 520 nm. In the end, when the nanorod were aligned along ***y*** axis, the absorption band at 700 nm disappears almost completely. The color of nanorod dispersion changes accordingly, from green to red, as shown in the inset in Figure 5.7b. When the orientation of gold nanorods are tuned within the ***xy*** plane, the longitudinal mode cannot be excited, so that the absorption band at 520 nm dominates the absorption spectra (Figure 5.7c), and the gold nanorods dispersion remains in a red color. The complete suppressions of either longitudinal or transverse plasmon modes can be achieved in the above cases, suggesting very good alignment of gold nanorods with external magnetic fields.

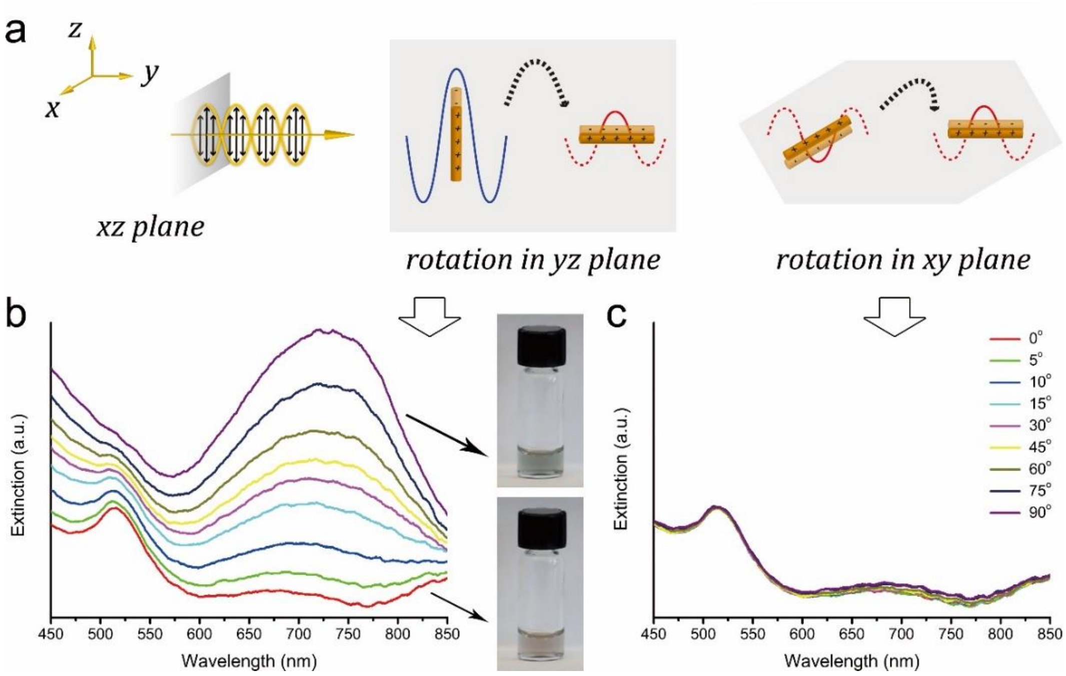

**Figure 5.8** (a) Scheme showing the plasmon excitations of gold nanorods under linear polarized light; (b). Extinction spectra of a dispersion of the hybrid nanorods under a magnetic field with its direction varying from perpendicular to parallel within the ***yz*** plane relative to the incident light. The incident light is linearly polarized along the ***z*** axis. The inset shows digital images of the dispersion under a magnetic field with its direction parallel (bottom) and perpendicular (up) to the incident beam; (c) Extinction spectra of the dispersion under a magnetic field with its direction varying within the ***xy*** plane from perpendicular to parallel relative to the incident light. The incident light is linearly polarized along the ***z*** axis.

In order to obtain a quantitative understanding of the rate of optical response, I studied the optical property of hybrid nanorods under alternating magnetic fields.[32, 33] Upon the application of such a field, the orientation of gold nanorods oscillated, leading to alternating changes in their extinction spectra, as schematized in Figure 5.8a. At a 200 Hz magnetic field, gold nanorods showed a 6% modulation to a laser beam at 650 nm (red curve in Figure 5.8b), which was close to the excitation wavelength of longitudinal mode of gold nanorods. To confirm that this effect is resulted from gold nanorods, another laser beam at 530 nm (corresponding to the resonant wavelength of the transverse mode) was chosen and only a 0.15% modulation was achieved, which could be attributed to the changes in the extinction cross-section of magnetic nanorods. The modulation percentages showed no variations after many cycles, indicating good reversibility of the magnetic tuning. More interestingly, the optical response of gold nanorods to a rotating magnetic field could be clearly visualized by placing their colloidal dispersion on the top of a magnetic stirrer. Then the nanorods rotated just like a stir bar, and displayed alternating green and red colors under ordinary light or linear polarized light with a direction parallel to the rotating plane of stirrer. No color change could be observed when the nanorods dispersion was illuminated under incident lights polarized perpendicular to the rotating plane, in great accordance with above findings.

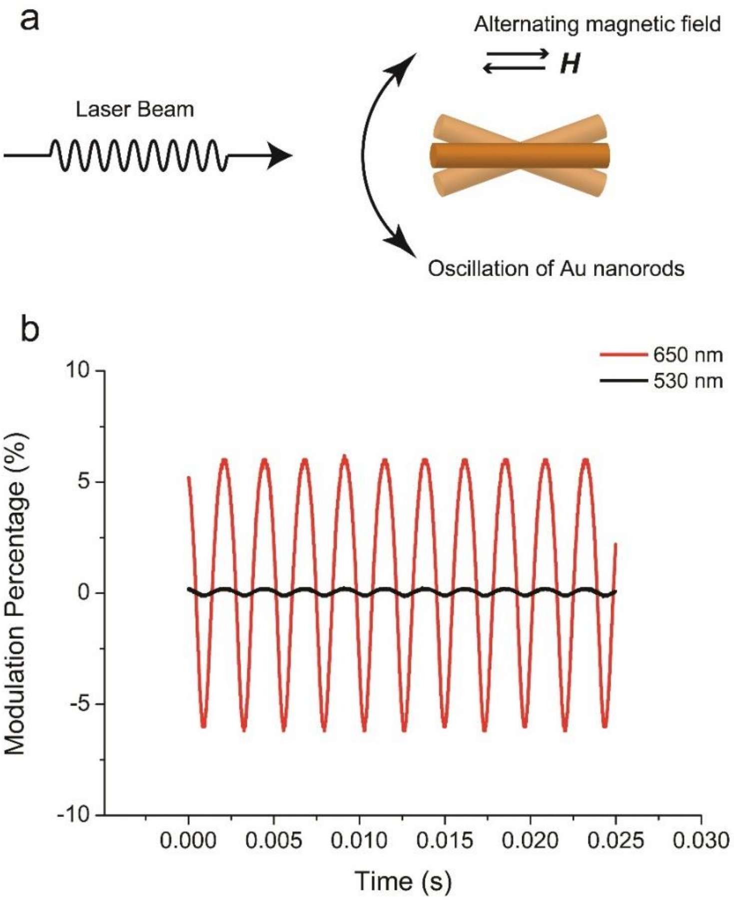

**Figure 5.9** (a) Scheme showing optical modulation using gold nanorods oscillating under an alternating magnetic field with field direction parallel to the incident laser beam. Longitudinal plasmon can only be excited when gold nanorods are displaced from the parallel position and illuminated by light with comparable wavelength. The resulting change in extinction thus leads to intensity modulation of the laser beam; (b) Optical modulation of gold nanorods to laser beams with different wavelengths under a 200 Hz alternating magnetic field: 650 nm (Red) and 532 nm (black).

The instant color change of these hybrid gold-magnetic nanorods under different magnetic field and different incident lights makes them excellent candidates for lots of applications, which include but not limit to data storage,[34] photonics,[26, 35-38] and biomedicine.[39-42] As practical applications usually favor solid materials rather than liquid dispersions, it is further demonstrated that these hybrid gold-magnetic nanorods can be made into color changing solid polymer films, by taking advantages of a photo-polymerization technique. The hybrid gold-magnetic nanorods were first coated with a layer of silica to enhance their dispersibility in pre-polymer solutions. A representative TEM image of the coated hybrid nanorods is presented in Figure 5.9a. After being dispersed in a PEGDA solution and then cured under UV light, solid polymer films with color patterns were obtained, as shown in Figure 5.9b, 5,9c and 5.9d.

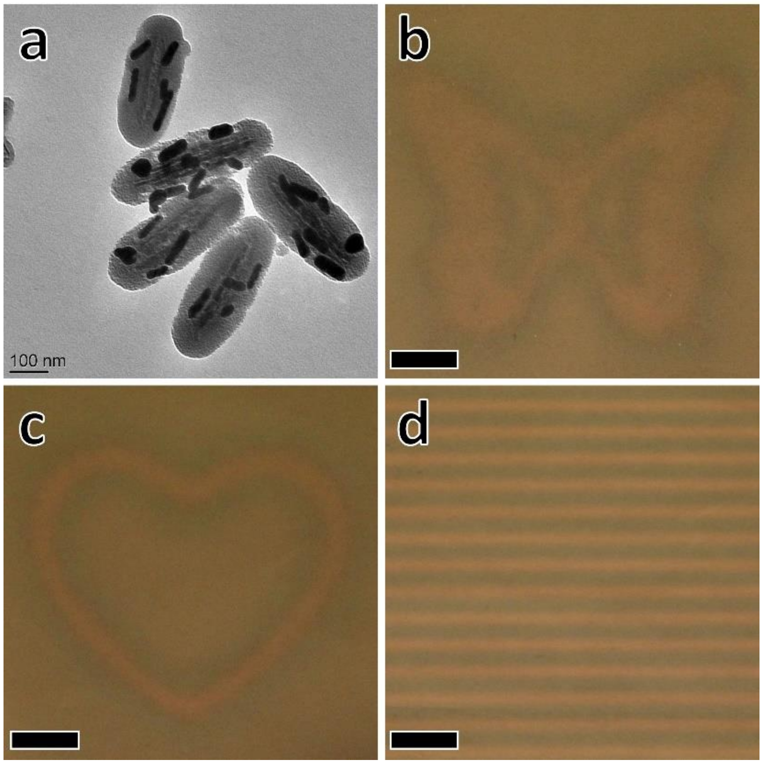

**Figure 5.10** (a) A TEM image of the silica-coated hybrid gold-$Fe_3O_4$ nanorods; (b-d) Digital images of PEGDA solid films with hybrid nanorods embedded inside. Scale bar: 1 mm.

## 5.4 Conclusion

In summary, I have successfully demonstrated the magnetic manipulation of plasmon excitation of gold nanorods by controlling their orientation relative to the incident lights. Such tuning is enabled by attaching gold nanorods to $Fe_3O_4$ nanorods whose orientation can be magnetically controlled. By tuning the direction of magnetic field, I am able to control the excitation of plasmonic modes of gold nanorods under the incidence of ordinary and polarized light. The colloidal dispersion of gold nanorods shows instant color switching in response to the changes in the orientation or strength of external magnetic fields. The optical switching is extremely sensitive and can operate under considerably weak magnetic fields or alternating magnetic fields with high frequency. The same strategy can be extended to dynamic tuning of the optical property of other anisotropic plasmonic nanostructures by using magnetic fields. These tunable plasmonic hybrid nanostructures not only enhance our understanding in plasmonic tuning, but also provide a new platform for building novel active optical components, color presentation and display devices, and highly sensitive and selective chemical and biomedical sensors.

## 5.5 Reference

1. Hu, M.-S., et al., *Photosensitive gold-nanoparticle-embedded dielectric nanowires*. Nature Materials, 2006. **5**(2): p. 102-106.
2. Huang, X., et al., *Plasmonic photothermal therapy (PPTT) using gold nanoparticles*. Lasers Med. Sci., 2008. **23**(3): p. 217-228.
3. Frens, G., *Controlled Nucleation for Regulation of Particle-Size in Monodisperse Gold Suspensions*. Nature-Physical Science, 1973. **241**(105): p. 20-22.

4. Link, S. and M.A. El-Sayed, *Size and temperature dependence of the plasmon absorption of colloidal gold nanoparticles*. Journal of Physical Chemistry B, 1999. **103**(21): p. 4212-4217.

5. Hussain, I., et al., *Size-controlled synthesis of near-monodisperse gold nanoparticles in the 1-4 nm range using polymeric stabilizers*. Journal of the American Chemical Society, 2005. **127**(47): p. 16398-16399.

6. Jana, N.R., L. Gearheart, and C.J. Murphy, *Wet chemical synthesis of high aspect ratio cylindrical gold nanorods*. Journal of Physical Chemistry B, 2001. **105**(19): p. 4065-4067.

7. Aizpurua, J., et al., *Optical properties of gold nanorings*. Physical Review Letters, 2003. **90**(5).

8. Nikoobakht, B. and M.A. El-Sayed, *Preparation and growth mechanism of gold nanorods (NRs) using seed-mediated growth method*. Chemistry of Materials, 2003. **15**(10): p. 1957-1962.

9. Nehl, C.L., H.W. Liao, and J.H. Hafner, *Optical properties of star-shaped gold nanoparticles*. Nano Letters, 2006. **6**(4): p. 683-688.

10. Sanchez-Iglesias, A., et al., *Synthesis and optical properties of gold nanodecahedra with size control*. Advanced Materials, 2006. **18**(19): p. 2529-+.

11. Millstone, J.E., et al., *Colloidal Gold and Silver Triangular Nanoprisms*. Small, 2009. **5**(6): p. 646-664.

12. Link, S., M.B. Mohamed, and M.A. El-Sayed, *Simulation of the optical absorption spectra of gold nanorods as a function of their aspect ratio and the effect of the medium dielectric constant*. Journal of Physical Chemistry B, 1999. **103**(16): p. 3073-3077.

13. Kelly, K.L., et al., *The optical properties of metal nanoparticles: The influence of size, shape, and dielectric environment*. Journal of Physical Chemistry B, 2003. **107**(3): p. 668-677.

14. Lin, S., et al., *One-Dimensional Plasmon Coupling by Facile Self-Assembly of Gold Nanoparticles into Branched Chain Networks*. Advanced Materials, 2005. **17**(21): p. 2553-2559.

15. Nie, S. and S.R. Emory, *Probing Single Molecules and Single Nanoparticles by Surface-Enhanced Raman Scattering*. Science, 1997. **275**(5303): p. 1102-1106.

16. Mirkin, C.A., et al., *A DNA-based method for rationally assembling nanoparticles into macroscopic materials*. Nature, 1996. **382**(6592): p. 607-609.

17. Elghanian, R., et al., *Selective colorimetric detection of polynucleotides based on the distance-dependent optical properties of gold nanoparticles*. Science, 1997. **277**(5329): p. 1078-1081.

18. Nikoobakht, B., Z.L. Wang, and M.A. El-Sayed, *Self-assembly of gold nanorods*. Journal of Physical Chemistry B, 2000. **104**(36): p. 8635-8640.

19. Storhoff, J.J., et al., *What controls the optical properties of DNA-linked gold nanoparticle assemblies?* Journal of the American Chemical Society, 2000. **122**(19): p. 4640-4650.

20. Zhang, H. and D. Wang, *Controlling the Growth of Charged-Nanoparticle Chains through Interparticle Electrostatic Repulsion*. Angewandte Chemie International Edition, 2008. **47**(21): p. 3984-3987.

21. Yang, M., et al., *Mechanistic investigation into the spontaneous linear assembly of gold nanospheres*. Physical Chemistry Chemical Physics, 2010. **12**(38): p. 11850-11860.

22. Zhang, H., et al., *Controlled Chainlike Agglomeration of Charged Gold Nanoparticles via a Deliberate Interaction Balance*. Journal of Physical Chemistry C, 2008. **112**(43): p. 16830-16839.

23. Dirix, Y., et al., *Oriented pearl-necklace arrays of metallic nanoparticles in polymers: A new route toward polarization-dependent color filters*. Advanced Materials, 1999. **11**(3): p. 223-+.

24. van der Zande, B.M.I., et al., *Optical properties of aligned rod-shaped gold particles dispersed in poly(vinyl alcohol) films*. Journal of Physical Chemistry B, 1999. **103**(28): p. 5761-5767.

25. Murphy, C.L. and C.J. Orendorff, *Alignment of gold nanorods in polymer composites and on polymer surfaces*. Advanced Materials, 2005. **17**(18): p. 2173-2177.

26. Perez-Juste, J., et al., *Optical control and patterning of gold-nanorod-poly(vinyl alcohol) nanocomposite films*. Advanced Functional Materials, 2005. **15**(7): p. 1065-1071.

27. Zhu, M.-Q., et al., *Thermosensitive Gold Nanoparticles*. Journal of the American Chemical Society, 2004. **126**(9): p. 2656-2657.

28. Klajn, R., K.J.M. Bishop, and B.A. Grzybowski, *Light-controlled self-assembly of reversible and irreversible nanoparticle suprastructures*. Proceedings of the National Academy of Sciences, 2007. **104**(25): p. 10305-10309.

29. Li, D., et al., *Fabrication of pH-Responsive Nanocomposites of Gold Nanoparticles/Poly(4-vinylpyridine)*. Chemistry of Materials, 2007. **19**(3): p. 412-417.

30. Ge, J.P., Y.X. Hu, and Y.D. Yin, *Highly tunable superparamagnetic colloidal photonic crystals*. Angewandte Chemie-International Edition, 2007. **46**(39): p. 7428-7431.

31. He, L., et al., *Magnetic Assembly Route to Colloidal Responsive Photonic Nanostructures*. Accounts of Chemical Research, 2012. **45**(9): p. 1431-1440.

32. Peng, Z.M., et al., *Synthesis of magnetite nanorods through reduction of beta-FeOOH*. Chemistry Letters, 2005. **34**(5): p. 636-637.

33. Piao, Y., et al., *Wrap-bake-peel process for nanostructural transformation from beta-FeOOH nanorods to biocompatible iron oxide nanocapsules*. Nature Materials, 2008. **7**(3): p. 242-247.

34. Zijlstra, P., J.W.M. Chon, and M. Gu, *Five-dimensional optical recording mediated by surface plasmons in gold nanorods*. Nature, 2009. **459**(7245): p. 410-413.

35. Roskov, K.E., et al., *Long-Range Alignment of Gold Nanorods in Electrospun Polymer Nano/Microfibers*. Langmuir, 2011. **27**(23): p. 13965-13969.

36. Wang, H.F., et al., *In vitro and in vivo two-photon luminescence imaging of single gold nanorods*. Proceedings of the National Academy of Sciences of the United States of America, 2005. **102**(44): p. 15752-15756.

37. Wang, P., et al., *Polymer Nanofibers Embedded with Aligned Gold Nanorods: A New Platform for Plasmonic Studies and Optical Sensing*. Nano Letters, 2012. **12**(6): p. 3145-3150.

38. Wilson, O., G.J. Wilson, and P. Mulvaney, *Laser writing in polarized silver nanorod films*. Advanced Materials, 2002. **14**(13-14): p. 1000-+.

39. Huang, X.H., et al., *Cancer cell imaging and photothermal therapy in the near-infrared region by using gold nanorods*. Journal of the American Chemical Society, 2006. **128**(6): p. 2115-2120.

40. Huang, X.H., S. Neretina, and M.A. El-Sayed, *Gold Nanorods: From Synthesis and Properties to Biological and Biomedical Applications*. Advanced Materials, 2009. **21**(48): p. 4880-4910.

41. Murphy, C.J., et al., *Gold Nanoparticles in Biology: Beyond Toxicity to Cellular Imaging*. Accounts of Chemical Research, 2008. **41**(12): p. 1721-1730.

42. Salem, A.K., P.C. Searson, and K.W. Leong, *Multifunctional nanorods for gene delivery*. Nature Materials, 2003. **2**(10): p. 668-671.

# Chapter 6

# Conclusion and Outlook

## 6.1 Conclusion of This Thesis

In this thesis, I have presented our recent understandings in the fabrication of magnetically responsive structures with tunable optical property via a self-assembly route. The key factors to success fabrications are the design of magnetically responsive building blocks with distinct sizes, shapes and chemical compositions, as well as the establishment of an equilibrium between magnetic dipole-dipole attractive forces and comparably strong long-range electrostatic repulsive forces for their assembly. The self-assembly of such building blocks system into photonic structures, liquid crystals and plasmonic structures have been demonstrated. Owing to the instantaneous nature of magnetic dipole-dipole interactions, they quickly respond to the change in the external magnetic fields, within less than one tenth of a second, making them very promising candidates for a large variety of applications, such as displays, optical devices and sensors.

## 6.2 Outlook and Future Work

Despite the tremendous progress made in the development of magnetically responsive optical structures, a number of challenges still present. I believe that future research in this area will be primarily focused on the design and synthesis of magnetically responsive building blocks with more complexity in their sizes, shapes, chemical compositions and physical properties. One general example is the 2D planar magnetically responsive building blocks, such as nanodisks and nanoplates. The synthesis of 2D materials with uniform and controllable size distributions is demanding as it requires for different growth rates of materials towards different directions and thus sophisticate controls of both thermodynamic factors and kinetic factors during the synthesis; however, they are expected to bring more degree of freedom into the system design and introduce novel optical properties or new methods of tuning to the as-assembled structures. Other examples include but not limit to materials with 3D morphologies including tetrahedral, cubic, octahedral, rhombohedral, etc. These well-defined materials have crystalline planes and axes with distinct orientations, which interact with light in different manners and thus add more complexity to the resultant superstructures.

Fundamental understandings to the self-assembly manner of building blocks are also critical to the design and fabrication of resultant superstructures. Our current knowledge in this field, however, is limited. For instance, the 1D and 2D assembly scenarios of anisotropic building blocks have not been investigated yet. Comprehensive phase diagrams for the self-assembly of nanoparticles under different volume concentration are highly desired. Investigations of their assembly behavior under ultra-strong magnetic fields or high-frequency alternating magnetic fields are also of great interest, which helps the development of new magnetic tuning methods. Continuous research in these directions will provide people with better accuracy and precision in predicting and controlling the resultant structures. Advances in the synthesis of building blocks and in the fundamental understandings about the self-assembly manners are expected to prospect the fabrications of responsive structures with more complex design with more exciting and novel optical effects.

The last but the biggest challenge towards the practical applications of magnetically responsive structures is their scalability, from the synthesis of building blocks to their assembly to superstructures. In most previous studies, the synthesis of nanoparticles was in a milligram scale, or even in a microgram scale; while in most industrial applications, people is talking about gram scale or kilogram scale, which are more than six orders of magnitude larger in the amount. The upscale synthesis of nanoparticles requires a much more sophisticate control on the reaction process and usually specially-designed reaction apparatus. On the other hand, as the amount of building blocks increases, more factors need to be considered, which include but not limit to the concentration gradients in the building blocks dispersions, the homogeneity of magnetic fields as well as the time cost. As a result, the assembly method may need to be revised accordingly, which certainly requires a lot of efforts. Ultimately, after solving these issues, I hope that these magnetically responsive optical structures will be commercialized for industrial applications.